REPORT DOCUMENTATION PAGE

1. REPORT DATE (DD-MM-YYYY)	2. REPORT TYPE	3. DATES COVERED (From - To)
07-31-2008	Biannual Technical Report	1/1/2008 - 6/30/2008

4. TITLE AND SUBTITLE

Bi-annual (1/1/2008-6/30/2008) Performance/Technical Report for ONR Award under Grant N00014-07-1-0395
MARSnet: Mission-aware Autonomous Radar Sensor Network for Future Combat Systems

5a. CONTRACT NUMBER

5b. GRANT NUMBER
N00014 – 07 –1 –0395

5c. PROGRAM ELEMENT NUMBER

6. AUTHOR(S)
Liang, Qilian

5d. PROJECT NUMBER

5e. TASK NUMBER

5f. WORK UNIT NUMBER

7. PERFORMING ORGANIZATION NAME(S) AND ADDRESS(ES)
University of Texas at Arlington
Office of Sponsored Projects
PO Box 19145
Arlington, TX 76019

8. PERFORMING ORGANIZATION REPORT NUMBER

9. SPONSORING/MONITORING AGENCY NAME(S) AND ADDRESS(ES)
Office of Naval Research
875 N. Randolph St.
One Liberty Center
Arlington, VA 22203-1995

10. SPONSOR/MONITOR'S ACRONYM(S)
ONR

11. SPONSOR/MONITOR'S REPORT NUMBER(S)

12. DISTRIBUTION/AVAILABILITY STATEMENT
Approved for Public Release; Distribution is Unlimited.

13. SUPPLEMENTARY NOTES

14. ABSTRACT

During the period of 1/1/2008 – 6/30/2008, we performed the following studies on radar sensor network: 1. favor weak fuzzy logic systems: theory and applications to threat assessment in disparate sensor networks; 2. cognitive radar sensor networks: a human-inspired information integration and fuzzy logic system-based approach; 3. wireless channel modeling in foliage environment using UWB radar versus narrowband radar; 4. tri-phase coded waveforms: design and applications to radar systems.

15. SUBJECT TERMS
Radar Sensor Network, UWB Radar, fuzzy logic system, threat assessment, tri-phase coded waveforms, UWB channel.

16. SECURITY CLASSIFICATION OF:			17. LIMITATION OF ABSTRACT	18. NUMBER OF PAGES	19a. NAME OF RESPONSIBLE PERSON
a. REPORT	b. ABSTRACT	c. THIS PAGE			Qilian Liang
U	U	U	UU	134	19b. TELEPHONE NUMBER (Include area code) 817-272-1339

20080807 179

Bi-annual (1/1/2008–6/30/2008) Performance/Technical Report for
ONR Award under Grant N00014-07-1-0395
MARSnet: Mission-aware Autonomous Radar Sensor Network for
Future Combat Systems

Qilian Liang
Department of Electrical Engineering
University of Texas at Arlington
Arlington, TX 76019-0016 USA
Phone: 817-272-1339, Fax: 817-272-2253
E-mail: liang@uta.edu

Abstract

During the period of 1/1/2008 – 6/30/2008, we performed the following studies on radar sensor network:

1. favor weak fuzzy logic systems: theory and applications to threat assessment in disparate sensor networks;

2. cognitive radar sensor networks: a human-inspired information integration and fuzzy logic system-based approach;

3. wireless channel modeling in foliage environment using UWB radar versus narrowband radar;

4. tri-phase coded waveforms: design and applications to radar systems.

1 Favor Weak Fuzzy Logic Systems: Theory and Applications to Threat Assessment

In current and future DoD operational environments, such as the Global War on Terrorism (GWOT) and the Maritime Domain Awareness (MDA), there is a need to exploit and integrate heterogeneous sensor networks based information from multiple sensors across a variety of modalities, media types including radar, video imagery (static and dynamic), audio (speech), acoustic stimuli, IR, text, as well as signals from novel chemical and biological sensors. Unfortunately, current DoD tactical sensor systems are not networked to each other or to small expeditionary warfighters units operating on the battlefield. A divide exists between receiving timely and useful tactical sensor data and the delivery of actionable intelligence to the Marine Expeditionary Force (MEF) and subordinate expeditionary force units. Moreover, software applications do not exist to automatically translate and fuse data into tactical situational understanding, indications and warning (I&W). Algorithms do not exist to fuse tactical data (level 2 or 3 fusion for a GWOT asymmetric environment) in the expeditionary forces tactical environment using tactically available computing capabilities. This need is also motivated by the fact that humans display a remarkable capability to perform situation understanding despite noisy sensory signals and conflicting inputs. Humans are adept at network

1

visualization, and at understanding subtle implications among the network connections. To date, however, human's innate ability to process and integrate information from disparate, network-based sources for situational understanding has not translated well to automated systems.

Motivated by the above challenges, in [1], we applied human information integration mechanisms to threat assessment in heterogeneous sensor networks. Humans use multiple sources of sensory information to estimate environmental properties and has innate ability to integrate information from heterogeneous data sources. How the multi-sensory and multimodal information are integrated in human brain? There is consensus that it depends on the prefrontal cortex (PFC). The PFC has top-down control (favor weak) and rule-based mechanisms, and we propose to incorporate the favor weak mechanism into rule-based fuzzy logic systems (FLS) via using upper and lower membership functions. The inference engine of favor weak fuzzzy logic system is proposed under three different categories based on fuzzifiers. We observe that the favor weak FLS is a special type-1 FLS which is embedded in an interval type-2 FLS, so its much simpler in computing than an interval type-2 FLS. We applied the favor weak FLS to situation understanding based on heterogeneous sensor network, and it shows that our favor weak fuzzy logic system has clear advantage comparing to the type-1 FLS. The favor weak FLS can increase the probability of threat detection, and provides timely I&W.

2 Cognitive Radar Sensor Networks: A Human-Inspired Information Integration and Fuzzy Logic System-Based Approach

Inspired by human's innate ability to process and integrate information from network-based sources, we applied [2][4] human-inspired information integration mechanisms to target detection in cognitive radar sensor network. Humans' information integration mechanisms have been modelled using maximum-likelihood estimation (MLE) or soft-max approaches. In [2][4], we applied these two algorithms to cognitive radar sensor networks target detection. Discrete-cosine-transform (DCT) was used to process the integrated data from MLE or soft-max. We applied fuzzy logic system (FLS) to automatic target detection based on the AC power values from DCT. Simulation results showed that our MLE-DCT-FLS and soft-max-DCT-FLS approaches performed very well in the radar sensor network target detection, whereas the existing 2-D construction algorithm didn't work in this study.

3 Wireless Channel Modeling in Foliage Environment: UWB versus Narrowband

In [3], we studied the wireless channel modeling in foliage environment, a rich scattering and time-varying environment, based on extensive data collected using UWB and narrowband (200MHz and 400MHz) radars. We applied two approaches to the wireless channel modeling: Saleh and Valenzuela (S-V) method for UWB channel modeling and CLEAN method for narrowband and UWB channel modeling. We validated that UWB echo signals (within a burst) don't hold self-similarity, which means the future signals can't be forecasted based on the received signals and channel modeling is necessary from statistical point of view. Based on the S-V method for UWB channel modeling, in foliage UWB channel, the multi-path contributions arrive at the receiver are grouped into clusters. The time of arrival of clusters can be modeled as a Poisson arrival process, while within each cluster, subsequent multipath contributions or rays also arrive according to a Poisson process. At different field (near field, medium field, and far field), we observe that the

2

Poisson process parameters are quite different. We also observe that the amplitude of channel coefficient at each path follows Rician distribution for medium and far field, and it's non-stationary for paths from near field (one of two Rician distributions), and these observations are quite different with the IEEE indoor UWB channel model and S-V indoor channel model. Based on the CLEAN method, the narrowband (200MHz and 400MHz) and UWB channel impulse responses have many similarities: both can be modeled as linear time-variant filter channel.

In [5][6], we studied the statistical modeling for outdoor non line-of-sight (NLOS) channel in rich scattering and time-varying foliage environment based on extensive data collected using both narrowband and ultra-wideband (UWB) radars. The multi-path contributions arrive at the receiver are grouped into clusters. The time of arrival of clusters can be modeled as a Poisson arrival process, while within each cluster, subsequent multipath contributions or rays also arrive according to a Poisson process. However, the parameters are quite different along with the frequency. We also observe that the amplitude of channel coecient at each path can be more accurately characterized by log-logistic distribution (LLD) other than log-normal, Weibull or Rayleigh due to the best goodness-of-fit and smallest root-mean-square (RMS).

4 Tri-Phase Coded Waveforms: Design and Applications to Radar Systems

A phase coded waveform has a constant RF frequency, but an absolute phase that is switched between one of N fixed values at regular intervals within the pulse length. In this project, we proposed two tri-phase coded waveform ($N = 3$) design methods.

In [7], we presented [7] the definition and properties of ZCZ sequence-pair set based on zero correlation zone (ZCZ) concept, and proposed to use the perfect punctured sequence-pair together with Hadamard matrix in the zero correlation zone to construct the perfect punctured ZCZ sequence-pair set for tri-phase coded waveform design. According to performance analysis, perfect punctured ZCZ sequence-pair set has good autocorrelation and cross correlation properties when doppler shift is not large. The radar target detection system simulation results also show that perfect punctured ZCZ sequence-pair outperforms other conventional pulse compression codes, such as the well known polyphase codeP4 code. As a result, perfect punctured ZCZ sequence-pair set can be good candidate for pulse compression code.

In [8], we proposed new code punctured binary sequence-pair and applied it to tri-phase coded waveforms. The definitions and the autocorrelation properties of the proposed code are given. Doppler shift performance is also investigated. The significant advantages of punctured binary sequence-pair over conventional pulse compression codes, such as the widely used Barker codes, are zero autocorrelation sidelobes and the longer length of the code which can be as long as 31 so far. In the radar target detection system simulation, punctured binary sequencepair also outperforms other conventional pulse compression codes. Therefore, our proposed code can be used as one of the candidates for pulse compression code.

References

[1] Q. Liang, "Favor Weak Fuzzy Logic Systems: Theory and Applications," submitted to *IEEE Trans on Fuzzy Systems*.

[2] Q. Liang, "Cognitive Radar Sensor Networks: A Human-Inspired Information Integration and Fuzzy Logic System-Based Approach," submitted to *IEEE Trans on Fuzzy Systems*.

3

[3] Q. Liang, "Wireless Channel Modeling in Foliage Environment: UWB versus Narrowband," submitted to *IEEE Trans on Vehicular Technology*.

[4] Q. Liang, "Human-Inspired Information Integration for UWB Radar Sensor Networks," submitted to *IEEE MILCOM 2008*, San Diego, CA, Oct 2008.

[5] J. Liang, Q. Liang, "Outdoor Propagation Channel Modeling in Foliage Environment," submitted to *IEEE Trans on Aerospace and Electronic Systems*.

[6] J. Liang, Q. Liang, "Outdoor Propagation Channel Modeling in Foliage Environment," submitted to *IEEE MILCOM 2008*, San Diego, CA, Oct 2008.

[7] L. Xu, Q. Liang, "Perfect punctured ZCZ sequence-pair set: design, analysis, and application to radar," submitted to *IEEE MILCOM 2008*, San Diego, CA, Oct 2008.

[8] L. Xu, Q. Liang, T. Jiang, "Punctured binary sequence-pair and its application in radar system," submitted to *IEEE MILCOM 2008*, San Diego, CA, Oct 2008.

4

Favor Weak Fuzzy Logic Systems: Theory and Applications

Qilian Liang, *Senior Member, IEEE*

Department of Electrical Engineering

University of Texas at Arlington

Arlington, TX 76019-0016 USA

E-mail: liang@uta.edu

Abstract

Humans use multiple sources of sensory information to estimate environmental properties and has innate ability to integrate information from heterogeneous data sources. How the multi-sensory and multimodal information are integrated in human brain? There is consensus that it depends on the prefrontal cortex (PFC). The PFC has top-down control (favor weak) and rule-based mechanisms, and we propose to incorporate the favor weak mechanism into rule-based fuzzy logic systems (FLS) via using upper and lower membership functions. The inference engine of favor weak fuzzy logic system is proposed under three different categories based on fuzzifiers. We observe that the favor weak FLS is a special type-1 FLS which is embeded in an interval type-2 FLS, so it's much simpler in computing than an interval type-2 FLS. We apply the favor weak FLS to situation understanding based on heterogeneous sensor network, and it shows that our favor weak fuzzy logic system has clear advantage comparing to the type-1 FLS. The favor weak FLS can increase the probability of threat detection, and provides timely indication & warning (I&W).

Index Terms : Fuzzy logic systems, prefrontal cortex (PFC), favor weak, upper and lower membership functions, situation understanding, heterogeneous sensor networks.

1

1 Introduction and Motivation

Humans use multiple sources of sensory information to estimate environmental properties. For example, the eyes and hands both provide relevant information about an objects shape. The eyes estimate shape using binocular disparity, perspective projection, etc. The hands supply haptic shape information by means of tactile and proprioceptive cues. **Combining information across cues can improve estimation of object properties** but may come at a cost: loss of single-cue information. Recent studies [12] showed that single-cue information is indeed lost when cues from within the same sensory modality (e.g., disparity and texture gradients in vision) are combined, **but not when different modalities (vision and haptics) are combined**. In another study on human [7], gaze shifts are coordinated movements of the eyes (eyes-re-head) and head (head-re-space) that rapidly reorient the visual axis (eyes-re-space) to a target of interest. Reaction latencies for gaze shifts to combined auditory and visual stimuli presented in close spatial and temporal register are **less than those to either stimulus presented alone**, suggesting that the integration of multisensory information may play an important role in forming appropriate motor behaviors. These studies demonstrate that human has innate ability to integrate information from heterogeneous data sources and multi-sensory and multimodal information integration has clear advantage.

In this paper, as a product of multidisciplinary collaborative research, we incorporate human brain mechanisms to a new fuzzy logic system design and apply it to situation understanding based on heterogeneous sensor network. A heterogeneous sensor network consists of multiple networked sensors with different modality (video, audio, acoustic, radar, etc), and such networks are necessary in different applications. For example, in an emergency natural disaster scenario, information integration for first responders is critical for search and rescue. Besides, the first responders need to be situation-aware. Danger may appear anywhere at any time, therefore, first responders must monitor a large area continuously in order to iden-

2

tify potential danger and take actions. Due to the dynamic and complex nature of natural disaster, some victims may not be found with a single type of sensor modality, for example, image/video sensors can't be used to find a buried/foleage victim, UWB radar sensors need to be used for penetrating the ground or sense-through-wall, and acoustic sensors are needed to collect the voice from victims. Similarly, some potential dangers may not be identified using a single modality sensor. More modalities are required to search victims and identify potential dangers and that means large-scale Heterogeneous Sensor Networks (HSN) are needed for search, rescue, and situation awareness. However, information integration algorithms (especially for situation awareness) for heterogeneous sensor networks don't exist. Motivated by the above challenges, we study human-inspired information integration for heterogeneous sensor networks.

The remaining of the paper is organized as follows. In Section 2, we present the heterogeneous information integration in Human brain and challenges to fuzzy logic system design. In Section 3, we give an overview on upper and lower membership design and describe how it can be used to the new fuzzy logic system design. In Section 4, we present the inference engine for favor weak fuzzy logic system, and its relations with the interval type-2 fuzzy logic systems are described in Section 5. The application to situation understanding based on heterogeneous sensor network is presented in Section 6. Section 7 concludes this paper.

2 Heterogeneous Information Integration in Human Brain and Challenges to Fuzzy Logic System Design

One of the great mysteries of the brain is cognitive control. How can the interactions between millions of neurons result in behavior that is coordinated and appears willful and voluntary? There is consensus that it depends on the prefrontal cortex (PFC) [31][35]. A schematic diagram of some of the extrinsic and intrinsic connections of the PFC is depicted in Fig. 1 [31].

3

Many PFC areas receive converging inputs from at least two sensory modalities [4][15]. For example, the dorsolateral (DL) (areas 8, 9, and 46) and ventrolateral (12 and 45) PFC both receive projections from visual, auditory, and somatosensory cortex. Furthermore, the PFC is connected with other cortical regions that are themselves sites of multimodal convergence. Many PFC areas (9, 12, 46, and 45) receive inputs from the rostral superior temporal sulcus, which has neurons with bimodal or trimodal (visual, auditory, and somatosensory) responses [1][36]. The arcuate sulcus region (areas 8 and 45) and area 12 seem to be particularly multimodal. They contain zones that receive overlapping inputs from three sensory modalities [36]. Observe, for example, that mid-dorsal area 9 directly processes and integrates visual, auditory, and multimodal information.

2.1 PFC Top-Down Control (Favor Weak) and Rule-Based Mechanisms

According to [31][35], the PFC is modulatory rather than transmissive. That is, the pathway from input to output does not "run through" the PFC. Instead, the PFC guides activity flow along task-relevant pathways in more posterior and/or subcortical areas. The PFC is important when "top-down" processing is needed; that is, when behavior must be guided by internal states or intentions. The PFC is critical in situations when the mappings between sensory inputs, thoughts, and actions either are *weakly established* relative to other existing ones or are *rapidly changing*. This is when we need to use the "*rules* of the game," internal representations of goals and the means to achieve them [31]. Several investigators have argued that this is a cardinal function of the PFC [6][37][11][41][30]. The top-down control and favor weak mechanism can be illustrated using the Stroop task Wisconsin card sort task (WCST).

In the Stroop task [40][27], subjects either read words or name the color in which they are written. To perform this task, subjects must selectively attend to one attribute. This is especially so when naming the color of a conflict stimulus (e.g. the word GREEN displayed in red), because there is a strong prepotent tendency to read the word ("green"), which competes

4

with the response to the color ("red"). This illustrates one of the most fundamental aspects of cognitive control and goal-directed behavior: the ability to select a weaker, task-relevant response (or source of information) in the face of competition from an otherwise stronger, but task-irrelevant one. Patients with frontal impairment have difficulty with this task, especially when the instructions vary frequently, which suggests that they have difficulty adhering to the goal of the task or its rules in the face of a competing stronger (i.e. more salient or habitual) response [31]. Similar findings are evident in the WCST [32]. Subjects are instructed to sort cards according to the shape, color, or number of symbols appearing on them and the sorting rule varies periodically. Thus, any given card can be associated with several possible actions, no single stimulus-response mapping will work, and the correct one changes and is dictated by whichever rule is currently in effect. Humans with PFC damage show stereotyped deficits in the WCST. They are able to acquire the initial mapping without much difficulty but are unable to adapt their behavior when the rule varies [32]. Monkeys with PFC lesions are impaired in an analog of this task and in others when they must switch between different rules [31].

The Stroop task, naming the color of a conflict stimulus, and WCST [32] are variously described as tapping the cognitive functions of either **selective attention, behavioral inhibition, top-down control, working memory, or rule-based or goal-directed behavior** [31]. As suggested by Desimone and Duncan [9], selective attention and behavioral inhibition are two sides of the same coin: attention is the effect of biasing competition in favor of task-relevant information, and inhibition is the consequence that this has for the irrelevant information. In this project, we will study human brain top-down control and rule-based mechanisms inspired information integration. In current HSN design, the clusterhead only serves a "transmissive" (data collection and relay to gateway) function. In this project, the HSN clusterhead will also provide a "modulatory" function, i.e., multimodal information integration. In natural disaster or terrorist attack recovery, the most dangerous potential threat factors (stimuli) are weak or hidden but are highly correlated with the situation understanding task, and of course,

5

they are time sensitive (rapidly changing), which indicates that the PFC "top-down" control mechanism can be applied to HSN-based situation understanding.

The PFC top-down control signals *favor weak (but task-relevant) stimulus-response mappings* when they are in competition with more habitual, stronger ones (as in the Stroop task, where the word GREEN is stronger and the color red is weak), especially when flexibility is needed (such as in the WCST) [31]. Moreover, all of the PFC neural mechanisms depend on the representation of goals and *rules* in the form of patterns of activity in the PFC, which configure processing in other parts of the brain in accordance with current task demands [31][35]. Such mechanisms motivate us to heavily revisit a rule-based approach: fuzzy logic systems (FLS), mimicking the rule-based PFC neural mechanism, and subsequently applying it to HSN-based situation awareness.

2.2 Overview of Fuzzy Logic Systems and Its Shortfall

The current type-1 FLS designs doesn't have "favor strong or favor weak control". In a type-1 FLS with a rule base of M rules, in which each rule has p antecedents, let the lth rule be denoted by R^l, where R^l: IF x_1 is F_1^l, and x_2 is F_2^l, and, ..., and x_p is F_p^l THEN y is G^l. The membership function, $\mu_{B^l}(y)$, of a fired rule can be expressed by the following sup-star composition [29]:

$$\mu_{B^l}(y) = \sup_{\mathbf{x} \in A^*} [\mu_{A^*}(\mathbf{x}) \star \mu_{A^l \to B^l}(\mathbf{x}, y)] \tag{1}$$

where A^* is a p-dimensional Cartesian product space, $A^* = A_1^* \times \cdots \times A_p^*$, A_k^* is the measurement domain of input x_k, $(k = 1, \cdots, p)$; and, A^* is given by

$$\mu_{A^*}(\mathbf{x}) = \mu_{A_1^* \times \cdots \times A_p^*}(\mathbf{x}) = \mu_{X_1}(x_1) \star \cdots \star \mu_{X_p}(x_p) \tag{2}$$

In the current type-1 FLS design,

$$\mu_{A^l \to \tilde{B}^l}(\mathbf{x}, y) = \mu_{F_1^l}(x_1) \star \mu_{F_2^l}(x_2) \star \cdots \star \mu_{F_p^l}(x_p) \star \mu_{G^l}(y) \tag{3}$$

6

For the Stroop task, to name the color of a conflict stimulus (e.g. the word GREEN displayed in red), needs the favor weak mechanism because there is a strong prepotent tendency to read the word ("green"), which competes with the response to the color ("red"). In Fig. 2, we illustrate the schematic of the Stroop model using the example to name the color when the word GREEN displayed in red [31].

So in the FLS design, the firing degree for "red" should be boosted to reflect the "favor weak" mechanism if a conflict stimulus presents, but no control should be taken if no conflict stimulus presents (e.g., name the word when the word GREEN displayed in red). This motivates us to use different membership degrees under different scenarios. We propose to use interval type-2 fuzzy membership function for this favor weak (using upper membership function) or no control (using lower membership function) mechanism.

3 Upper and Lower Membership Functions

An upper MF and a lower MF are two type-1 MFs which are bounds for the footprint of uncertainty of an interval type-2 MF. The upper MF is a subset which has the maximum membership grade of the footprint of uncertainty; and, the lower MF is a subset which has the minimum membership grade of the footprint of uncertainty [17].

Same as that in [17], we use an overbar (underbar) to denote the upper (lower) MF. For example, the upper and lower MFs of $\mu_{\tilde{A}_k^l}(x_k)$ are $\overline{\mu}_{\tilde{A}_k^l}(x_k)$ and $\underline{\mu}_{\tilde{A}_k^l}(x_k)$, respectively, so that

$$\mu_{\tilde{A}_k^l}(x_k) = \int_{q^l \in [\underline{\mu}_{\tilde{A}_k^l}(x_k), \overline{\mu}_{\tilde{A}_k^l}(x_k)]} 1/q^l \tag{4}$$

Example 1: Gaussian Primary MF with Uncertain Standard Deviation

Consider the case of a Gaussian primary MF having a fixed mean, m_k^l, and an uncertain standard deviation that takes on values in $[\sigma_{k1}^l, \sigma_{k2}^l]$, i.e.,

$$\mu_k^l(x_k) = \exp\left[-\frac{1}{2}\left(\frac{x_k - m_k^l}{\sigma_k^l}\right)^2\right], \quad \sigma_k^l \in [\sigma_{k1}^l, \sigma_{k2}^l] \tag{5}$$

7

where: $k = 1, \ldots, p$; p is the number of antecedents; $l = 1, \ldots, M$; and, M is the number of rules. The upper MF, $\overline{\mu}_k^l(x_k)$, is (see Fig. 3b)

$$\overline{\mu}_k^l(x_k) = \mathcal{N}(m_k^l, \sigma_{k2}^l; x_k), \tag{6}$$

and the lower MF, $\underline{\mu}_k^l(x_k)$, is (see Fig. 3)

$$\underline{\mu}_k^l(x_k) = \mathcal{N}(m_k^l, \sigma_{k1}^l; x_k) \tag{7}$$

$\square$

This example illustrates how to define $\overline{\mu}$ and $\underline{\mu}$, so that it is clear how to define these membership functions for other situations (e.g., triangular, trapezoidal, bell MFs).

4 The Inference Engine for Favor Weak FLSs

In a favor weak FLS with a rule base of M rules, in which each rule has p antecedents, let the lth rule be denoted by R^l, where R^l: IF x_1 is $\tilde{F}_1^l$, and x_2 is $\tilde{F}_2^l$, and, $\ldots$, and x_p is $\tilde{F}_p^l$ THEN y is G^l. Although the rule may look the same as that of the interval type-2 FLS, but the inference engine is different.

In a favor weak FLS with p antecedents, without loss of generality, assume the first w ($w < p$) antecedents are weak and should be favored, and all other antecedents ($w+1, i_{w+2}, \cdots, i_p$) should be in no control. If the antecedents are not in this order, they can be re-orderred. Then we can obtain the following Theorem. Our major result for favor weak FLSs is given in:

Theorem 1 *In a favor weak nonsingleton FLS (the first w antecedents are weak and should be favored) with type-2 fuzzification and meet under minimum or product t-norm: (a) the firing degree for rule l, i.e., the result of the input and antecedent operations, is*

$$f^l = \sup_{\mathbf{x} \in X} \int_{X_1} \cdots \int_{X_p} [\overline{\mu}_{\tilde{X}_1}(x_1) \star \overline{\mu}_{\tilde{F}_1^l}(x_1)] \star \cdots \star [\overline{\mu}_{\tilde{X}_w}(x_w) \star \overline{\mu}_{\tilde{F}_w^l}(x_w)] \tag{8}$$

$$\star [\underline{\mu}_{\tilde{X}_{w+1}}(x_{w+1}) \star \underline{\mu}_{\tilde{F}_{w+1}^l}(x_{w+1})] \star \cdots \star [\underline{\mu}_{\tilde{X}_p}(x_p) \star \underline{\mu}_{\tilde{F}_p^l}(x_p)] / \mathbf{x}; \tag{9}$$

8

the supremum is attained when each term in brackets attains its supremum;

(b) the rule R^l fired output consequent set, $\mu_{B^l}(y)$, is

$$\mu_{B^l}(y) = f^l \star \mu_{G^l}(y) \tag{10}$$

where $\underline{\mu}_{\tilde{G}^l}(y)$ and $\overline{\mu}_{\tilde{G}^l}(y)$ are the lower and upper membership grades of $\mu_{\tilde{G}^l}(y)$; and,

(c) the output fuzzy set, $\mu_B(y)$, is

$$\mu_{\tilde{B}}(y) = \bigcup_{l=1}^{M} \mu_{B^l}(y) \tag{11}$$

When the input is fuzzified to a type-1 fuzzy set, so that $\mu_{\tilde{X}_k} \to \mu_{X_k}$ $(k = 1, \ldots, p)$, the upper and lower MFs of $\mu_{\tilde{X}_k}$ merge into one MF, $\mu_{X_k}(x_k)$, in which case Theorem 1 simplifies to:

Corollary 1 *In a favor weak FLS (the first w antecedents are weak and should be favored) with* nonsingleton type-1 fuzzification *and meet under minimum or product t-norm, f^l in (9) simplifies to: the firing degree for rule l is*

$$f^l = \sup_{\mathbf{x} \in X} \int_{X_1} \cdots \int_{X_p} [\mu_{X_1}(x_1) \star \overline{\mu}_{\tilde{F}_1^l}(x_1)] \star \cdots \star [\mu_{X_w}(x_w) \star \overline{\mu}_{\tilde{F}_w^l}(x_w)] \tag{12}$$

$$\star [\mu_{X_{w+1}}(x_{w+1}) \star \underline{\mu}_{\tilde{F}_{w+1}^l}(x_{w+1})] \star \cdots \star [\mu_{X_p}(x_p) \star \underline{\mu}_{\tilde{F}_p^l}(x_p)] / \mathbf{x} \, ; \tag{13}$$

the supremum is attained when each term in brackets attains its supremum;

When a singleton fuzzifier is used, the upper and lower MFs of $\mu_{\tilde{X}_k}(x_k)$ merge into one crisp value, namely 1, in which case Theorem 1 simplifies further to:

Corollary 2 *In a favor weak FLS (the first w antecedents are weak and should be favored) with* singleton fuzzification *and meet under minimum or product t-norm, f^l in (9) simplifies to: the firing degree for rule l, i.e., the result of the input and antecedent operations,*

$$f^l = \overline{\mu}_{\tilde{F}_1^l}(x_1) \star \cdots \star \overline{\mu}_{\tilde{F}_w^l}(x_w) \star \underline{\mu}_{\tilde{F}_{w+1}^l}(x_{w+1}) \star \cdots \star \underline{\mu}_{\tilde{F}_p^l}(x_p) \tag{14}$$

where x_i $(i = 1, \ldots, p)$ denotes the location of the singleton.

9

5 Relations between Favor Weak FLS and Interval Type-2 FLS

In decision theory, *ambiguity* about probabilities should not affect choices. However, recent experiments [13] showed that many people are more willing to bet on risky outcomes (e.g., gambling on a roulette wheel) than on an ambiguous one (e.g., chance of a terrorist attack based on meager or conflicting evidence), holding the judged probability of outcomes constant. So, the confidence in judged probability can vary widely for "risky" and "ambiguous". Using functional brain imaging, Hsu et al [13] showed that the *level of ambiguity* in choices correlates positively with activation in the amygdala and orbitofrontal cortex, and negatively with a striatal system. This suggests that *degree of uncertainty* should be considered in decision making, contrary to traditional decision theory. Type-2 fuzzy sets and FLSs are successful in handling the uncertainties [17]. Type-2 fuzzy sets have grades of membership that are themselves fuzzy. A type-2 membership grade can be any subset in $[0, 1]$ – the *primary membership*; and, corresponding to each primary membership, there is a *secondary membership* (which can also be in $[0, 1]$) that defines the possibilities for the primary membership. Figure 4 shows an example of a type-2 set. The domain of the membership grade corresponding to $x = 4$ is also shown.

In [17][20][22][23][24], Liang and Mendel proposed the theory and design of interval type-2 FLS. With their pioneering works, people are able to efficiently handle uncertainties. They applied interval type-2 FLS to a number of very important applications where uncertainties abound, such as fading channel equalization [18] and co-channel interference elimination [19], network video traffic modeling and classification [21], connection admission control for ATM network [16]. Recently, Liang and his students applied interval type-2 FLSs to sensor network lifetime estimation[39][38], event forecasting in wireless sensor networks[25][26], and cross-layer optimization in ad hoc networks[43][42].

In this paper, PFC's "top-down control (favor weak)", "rule-based", and "brain handling ambiguity" mechanisms are incorporated into the favor weak FLS design to mimic human

10

brain learning and decision making for associating, integrating and understanding/inferencing discovered knowledge from disparate sources. The favor weak FLS we proposed in this paper is a type-1 FLS which is embeded in the interval type-2 FLS.

6 Application to Situation Understanding Based on Heterogeneous Sensor Network

Some valuable work has been reported on situation understanding (situation awareness and threat assessment). In [10], an intelligent threat assessment processor using genetic algorithms and fuzzy logic was proposed. In [33], threat assessment was studied in tactical airborne environments. In [14], a neural network was applied to threat assessment for automated visual surveillance. In [8], an intelligent assistant was proposed to provide automatic situation and threat advice in the Air Defence Ground Environment. In [2], a situation and threat assessment model based on group analysis was proposed. A situation/threat assessment fusion system was proposed in [5]. Other approaches that have appeared include multiple attribute decision making [3], bayesian networks [34], etc. Unfortunately, none of these approaches is appropriate for the multimodal sensor network scenario and none of them have used models derived from human or biological system mechanisms, although some computational intelligence models (such as neural networks and fuzzy logic) were used.

In situation awareness, the "weak" can be interpreted as, for example, 1) a target (or entity) rarely appears in the sensor field; or 2) the behavior pattern of this target (or entity) has low match with the existing ones in database; or 3) space/time correlation of data/entities to events is low, etc. All the above information can be obtained based on the assumption that high quality information about objects and events is available as a contributor to situation awareness. In general, however, such information is insufficient to provide adequate situation awareness. Actually, some lessons gained from terrorist attacks have already demonstrated

11

that the above "weaks" should be favored in situation awareness. Situation awareness needs the "favor weak" and rule-based mechanisms from PFC.

The new favor weak FLS can be used for level 2/3 fusion (situation awareness and threat assessment) for inferring activities, relationships, and intentions of objects and people in the battlespace based on retrieved knowledge consisting of behavioral patterns, new activities, and anticipated behavior, and also taking into account contextual information (terrain, roads, weather, etc). The level 1 data fusion results (traditional automatic target recognition and pattern recognition) from multimodal sensors will be used as antecedents. For example, considering a heterogeneous sensor network with radar, image/video sensors, and GPS sensor, we can choose the following three antecedents:

1. The number of switches from non-maneuvering set (constant behavior in speed, acceleration, and direction, etc) to the maneuvering set (varying behavior in speed, acceleration, and direction, etc). When a target is beginning a maneuver from a non-maneuvering class, the tracking system can switch the algorithms applied to the problem from a non-maneuvering set to the maneuvering set. The errors in distance from where the tracker estimates the position of a target between the actual position can be very large when the incorrect motion models are applied to the problem. Additionally, when the tracker does finally catch up to the target after the maneuver, the track will "jump" across the operator's scope giving a very unrealistic and unreliable picture of what that target is actually doing. So a threat target will quite often switch from a non-maneuvering set to the maneuvering set, and vice versa, to avoid being tracked all the time. This knowledge can be used as an antecedent for situation awareness.

2. The frequency of appearance of such type of target based on some a priori knowledge such as archival radar data. Generally threat targets are new comparing to archival radar data.

12

3. The importance of geolocation of this target based on the geographical information systems (GISs). Examples of important geolocations include large metroplex, landmarks, military bases, airport, etc. Threats happen quite often in such areas.

Of the above three antecedents, *the frequency of appearance of such type of target* is weak stimulus and should be favored. A typical rule using the above three antecedents can be

IF the number of switches from non-maneuvering set to the maneuvering set is *High*, and the frequency of appearance of such target is *Low*, and the importance of geolocation of such type of target is *High*, THEN the possibility that an I&W needs to be issued is *Very Strong*.

The linguistic variables used to represent each antecedent are divided into three levels: *Low*, *Moderate*, and *High*. The consequent – the possibility that an indication and warning (I&W) needs to be issued – is divided into 5 levels, *Very Strong, Strong, Medium, Weak, Very Weak*. So we need to set up $3^3 = 27$ (because every antecedent has 3 fuzzy sub-sets, and there are 3 antecedents) rules for this FLS. Table 1 summarizes the fuzzy rules we use in this paper. We show these MFs in Fig. 5.

For input (x_1, x_2, x_3), the output is computed using

$$y(x_1, x_2, x_3) = \frac{\sum_{l=1}^{27} \underline{\mu}_{\tilde{F}_l^1}(x_1)\overline{\mu}_{\tilde{F}_l^2}(x_2)\underline{\mu}_{\tilde{F}_l^3}(x_3)c_{avg}^l}{\sum_{l=1}^{27} \underline{\mu}_{\tilde{F}_l^1}(x_1)\overline{\mu}_{\tilde{F}_l^2}(x_2)\underline{\mu}_{\tilde{F}_l^3}(x_3)} \tag{15}$$

By repeating these calculations for $\forall x_i \in [0, 10]$, we obtain a hypersurface $y(x_1, x_2, x_3)$. This equation represents the nonlinear mapping between three inputs and one output of the FLS. Since it's a 4-D surface (x_1, x_2, x_3, y), it's impossible to be plotted visually.

If we have $x_3 = 8$, and two other antecedents, x_1 and x_2 are variables, we obtain a hypersurface $y(x_1, x_2, 8)$ based on the favor weak FLS, as plotted in Fig. 6(a). In contrast, we use a type-1 FLS where the antecedent membership functions are the lower membership functions in Fig. 5a since favor weak mechanism is not used, and its output hypersurface $y(x_1, x_2, 8)$ is plotted in Fig. 6(b). Observe that from Fig. 6, the favor weak FLS provides a higher possibility

13

that this target is a threat, which makes sense because the weak factor, frequency of appearance of such type of target, has been favored. So our proposed favor weak FLS can increase the probability of threat detection, and provides timely I&W.

7 Conclusions

Humans use multiple sources of sensory information to estimate environmental properties and has innate ability to integrate information from heterogeneous data sources. There is consensus that it depends on the brain PFC. The PFC has top-down control (favor weak) and rule-based mechanisms, which can be illustrated using the Stroop model. In this paper, we proposed to incorporate the favor weak mechanism into rule-based fuzzy logic systems (FLS) via using upper and lower membership functions. The inference engine of favor weak fuzzzy logic system was proposed under three different categories based on fuzzifiers. We analyzed that the favor weak FLS is a special type-1 FLS which is embeded in an interval type-2 FLS, so it's much simpler in computing than an interval type-2 FLS. We apply the favor weak FLS to situation understanding based on heterogeneous sensor network, and it shows that our favor weak fuzzy logic system has clear advantage comparing to the type-1 FLS. The favor weak FLS can increase the probability of threat detection, and provides timely indication & warning (I&W).

Acknowledgement

14

References

[1] C. Bruce C, R. Desimone, C. G. Gross, "Visual properties of neurons in a polysensory area in superior temporal sulcus of the macaque," *J. Neurophysiol.*, vol. 46 369- 84, 1981.

[2] Y. Cai, et al, "A Situation and Threat Assessment Model Based on Group Analysis," *Proceedings of 2005 International Conference on Machine Learning and Cybernetics*, Aug. 2005, pp. 356 - 361.

[3] Q. Changwen, H. You, "A method of threat assessment using multiple attribute decision making," *6th International Conference on Signal Processing*, Aug. 2002, pp. 1091 - 1095.

[4] D. A. Chavis, D. N. Pandya, "Further observations on cortico-frontal connections in the rhesus monkey," *Brain Res.*, vol. 117, pp. 369-386, 1976.

[5] J. W. Choi; J. W. Joo; D. L. Cho, "Situation/Threat Assessment Fusion System (STAFS)," *Proceedings of the Fifth International Conference on Information Fusion*, July 2002, pp. 1374 - 1380.

[6] J. D. Cohen, D. Servan-Schreiber, "Context, cortex and dopamine: a connectionist approach to behavior and biology in schizophrenia," *Psychol. Rev.*, vol. 99, pp. 45-77.

[7] B. D. Corneil, and D. P. Munoz, "The Influence of Auditory and Visual Distractors on Human Orienting Gaze Shifts," *The Journal of Neuroscience*, vol. 16, no. 24, pp. 8193-8207, December 15, 1996.

[8] I. W. Dall, "Threat assessment without situation assessment," *Proc of Information, Decision and Control*, Feb. 1999, pp. 365 - 370.

[9] R. Desimone, J. Duncan, "Neural mechanisms of selective visual attention," *Annu. Rev. Neurosci.*, vol. 18, pp. 193–222, 1995.

15

[10] P. Gonsalves, et al, "Intelligent threat assessment processor (ITAP) using genetic algorithms and fuzzy logic," *Proceedings of the Third International Conference on Information Fusion*, 2000.

[11] J. Grafman, "Alternative frameworks for the conceptualization of prefrontal functions," *Handbook of Neuropsychology*, ed. F Boller, J Grafman, pp. 187. Amsterdam: Elsevier.

[12] J. M. Hillis, M. O. Ernst, M. S. Banks, and M. S. Landy, "Combining sensory information: Mandatory fusion within, but not between, senses," *Science*, vol. 298, No. 5598, pp. 1627-1630, 2002.

[13] M. Hsu, et al, "Neural systems responding to degrees of uncertainty in human decision making," *Science*, vol. 310, pp. 1680-1683, Dec 2005.

[14] T. Jan, "Neural network based threat assessment for automated visual surveillance," *IEEE International Joint Conference on Neural Networks*, vol. 2, July 2004, pp. 1309 - 1312.

[15] E. G. Jones, T. P. S. Powell, An anatomical study of converging sensory pathways within the cerebral cortex of the monkey," *Brain*, vol. 93, pp. 793–820, 1970.

[16] Q. Liang, N. Karnik, and J. M. Mendel, " Connection admission control in ATM network using survey-based type-2 fuzzy logic systems," *IEEE Transactions on Systems, Man, and Cybernetics, Part C*, vol. 30, no. 3, pp. 529-539, August 2000.

[17] Q. Liang and J. M. Mendel, "Interval type-2 fuzzy logic systems: theory and design," *IEEE Transactions on Fuzzy Systems*, vol. 8, no. 5, pp. 535-550, Oct 2000.

[18] Q. Liang and J. M. Mendel, "Equalization of time-varying nonlinear channels using type-2 fuzzy adaptive filters," *IEEE Trans. on Fuzzy Systems*, vol. 8, no. 5, pp. 551-563, Oct 2000.

16

[19] Q. Liang and J. M. Mendel, " Overcoming time-varying co-channel interference using type-2 fuzzy adaptive filters", *IEEE Transactions on Circuits and Systems, II*, vol. 47, no. 12, pp. 1419-1428, Dec 2000.

[20] Q. Liang, J. M. Mendel, "Design interval type-2 fuzzy logic systems using SVD-QR method: rule reduction," *International Journal of Intelligent Systems*, vol. 15, no. 10, pp. 939957, Oct 2000.

[21] Q. Liang and J. M. Mendel, " MPEG VBR video traffic modeling and classification using fuzzy techniques," *IEEE Transactions on Fuzzy Systems*, vol. 9, no. 1, pp.183-193, Feb 2001.

[22] Q. Liang, J. M. Mendel, "Chapter 13: TSK fuzzy logic systems," *Uncertain Rule-Based Fuzzy Logic Systems*, pp. 421-453, Prentice-Hall, Upper Saddle River, NJ, Dec 2000.

[23] Q. Liang, J. M. Mendel, "Introduction to type-2 TSK fuzzy logic systems," *IEEE International Conference on Fuzzy Systems*, August 1999, Seoul, Korea.

[24] Q. Liang, J. M. Mendel, "Interval type-2 fuzzy logic systems," *IEEE International Conference on Fuzzy Systems*, May 2000, San Antonio, TX.

[25] Q. Liang, L. Wang, "Event Forecasting for Wireless Sensor Networks Using Interval Type-2 Fuzzy Logic System," submitted to *IEEE Transactions on Systems, Man, and Cybernetics, Part B*.

[26] Q. Liang, L. Wang, "Sensed signal strength forecasting for wireless sensors using interval type-2 fuzzy logic systems," *IEEE Intl Conference on Fuzzy Systems*, Reno, NV, May 2005.

[27] C. M. MacLeod, "Half a century of research on the Stroop effect: an integrative review," *Psychol. Bull.*, vol. 109, 163-203, 1991.

17

[28] K. Matsumoto and K. Tanaka, Conflict and Cognitive Control, *Science*, vol. 303, pp. 969-970, Feb 2004.

[29] J. M. Mendel, " Fuzzy logic systems for engineering: a tutorial ," *Proc. of the IEEE*, vol. 83, no. 3, pp. 345-377, March 1995.

[30] E. K. Miller, "The prefrontal cortex: complex neural properties for complex behavior," *Neuron*, vol. 22, pp. 15-17, 1999.

[31] E. K. Miller, J. D. Cohen, "An Integrative Theory of Prefrontal cortex function," *Annu. Rev. Neurosci.*, vol. 24, pp. 167, 2001.

[32] B. Milner, "Effects of different brain lesions on card sorting," *Arch. Neurol.*, vol. 9, pp. 90, 1963.

[33] X. T. Nguyen, "Threat assessment in tactical airborne environments," *Proceedings of the Fifth International Conference on Information Fusion*, July 2002.

[34] N. Okello, G. Thorns, "Threat assessment using bayesian networks," *Proceedings of the Sixth International Conference of Information Fusion*, vol. 2, pp. 1102 - 1109, 2003.

[35] R. C. O'Reilly, "Biologically Based Computational Models of High-Level Cognition," *Science*, Oct 2006.

[36] D. N. Pandya, C. Barnes, "Architecture and connections of the frontal lobe," *The Frontal Lobes Revisited*, ed. E Perecman, pp. 41- 72. New York: IRBN, 1987.

[37] R. Passingham, *The Frontal Lobes and Voluntary Action*, Oxford, UK: Oxford Univ. Press.

[38] H. Shu, Q. Liang, "Wireless Sensor Network Lifetime Analysis Using Interval Type-2 Fuzzy Logic Systems," *IEEE Intl Conference on Fuzzy Systems*, Reno, NV, May 2005.

18

[39] H. Shu, Q. Liang, "Wireless Sensor Network Lifetime Analysis Using Interval Type-2 Fuzzy Logic Systems," *IEEE Transactions on Fuzzy Systems*, vol. 16, no. 2, April 2008.

[40] J. R. Stroop, "Studies of interference in serial verbal reactions," *J. Exp. Psychol.* vol. 18, pp. 643- 62, 1935.

[41] S. P. Wise, et al, "The frontal-basal ganglia system in primates," *Crit. Rev. Neurobiol.*, vol. 10, pp. 317-356.

[42] X. Xia and Q. Liang, "Cross-Layer Optimization for Mobile Ad Hoc Networks Using Fuzzy Logic Systems," accepted by *International Journal of Uncertainty, Fuzziness and Knowledge-Based Systems*.

[43] X. Xia and Q. Liang, "Cross-Layer Optimization for Mobile Ad Hoc Networks Using Interval Type-2 Fuzzy Logic Systems," accepted by *IEEE GLOBECOM*, Nov 2006, San Francisco, CA.

[44] L. A. Zadeh, " The concept of a linguistic variable and its application to approximate reasoning - I," *Information Sciences*, vol. 8, pp. 199-249, 1975.

19

List of Tables

Table 1: Fuzzy rules used in the application. Ante 1 is the number of switches from non-maneuvering set to the maneuvering set or vice versa; Ante 2 the frequency of appearance of such type of target; Ante 3 is the importance of geolocation of this target; and Consequent is the possibility that this target is a threat.

Rule #	Ante 1	Ante 2	Ante 3	Consequent
1	low	low	low	Weak
2	low	low	moderate	Medium
3	low	low	high	Strong
4	low	moderate	low	Very Weak
5	low	moderate	moderate	Weak
6	low	moderate	high	Medium
7	low	high	low	Very Weak
8	low	high	moderate	Weak
9	low	high	high	Medium
10	moderate	low	low	Medium
11	moderate	low	moderate	Strong
12	moderate	low	high	Very Strong
13	moderate	moderate	low	Weak
14	moderate	moderate	moderate	Medium
15	moderate	moderate	high	Strong
16	moderate	high	low	Very Weak
17	moderate	high	moderate	Weak
18	moderate	high	high	Medium
19	high	low	low	Medium
20	high	low	moderate	Strong
21	high	low	high	Very Strong
22	high	moderate	low	Weak
23	high	moderate	moderate	Medium
24	high	moderate	high	Strong
25	high	high	low	Very Weak
26	high	high	moderate	Weak
27	high	high	high	Moderate

20

List of Figures

Figure 1: Schematic diagram of some of the extrinsic and intrinsic connections of the PFC. Most connections are reciprocal; the exceptions are indicated by arrows. The frontal eye field (FEF) has variously been considered either adjacent to, or part of, the PFC.

21

No Control

Verbal Response · Control (Prefrontal Cortex)

"red" "green" · colors words

RED GREEN

Color Stimuli · Word Stimuli

Conflict Stimulus: GREEN

(a)

Color Naming

Verbal Response · Control (Prefrontal Cortex)

"red" "green" · colors words

RED GREEN

Color Stimuli · Word Stimuli

Conflict Stimulus: GREEN

(b)

Figure 2: Schematic of the Stroop model. (a) No control. Activation of conflicting inputs in the two pathways produces a response associated with the word, due to the stronger connections in the word reading pathway. (b) Presentation of a conflict stimulus. The color unit is activated (indicated by the orange fill), representing the current intent to name the color. This passes activation to the intermediate units in the color naming pathway (indicated by arrows), which primes those units (indicated by larger size), and biases processing in favor of activity flowing along this pathway. This biasing effect favors activation of the response unit corresponding to the color input, even though the connection weights in this pathway are weaker than in the word pathway.

22
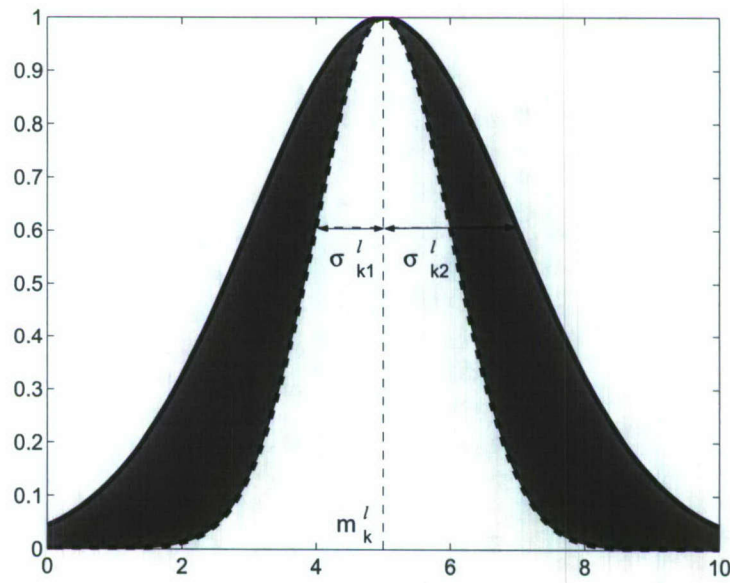
Figure 3: The type-2 MFs for Example 1. The thick solid lines denote upper MFs, and the thick dashed lines denote lower MFs. The shaded regions are the footprints of uncertainty for interval secondaries. The center of the Gaussian MFs is 5, and the variance varies from 1.0 to 2.0.

23
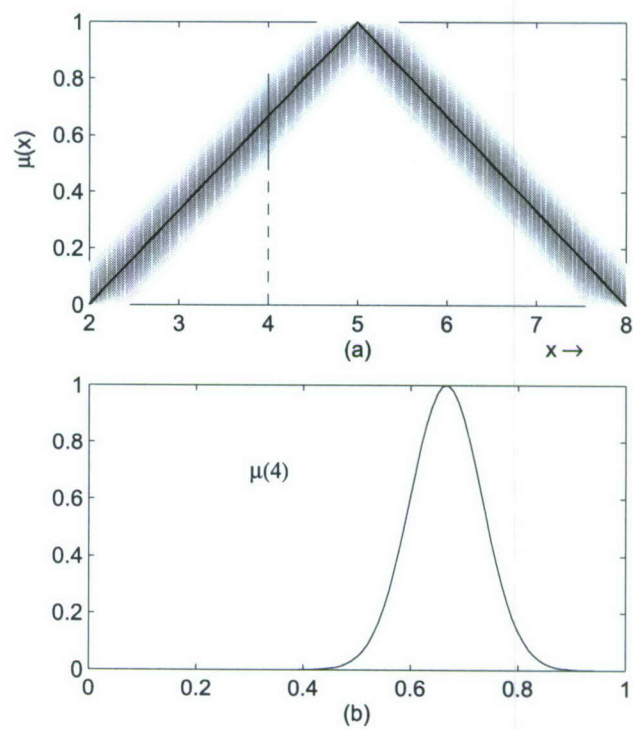
Figure 4: (a) Pictorial representation of a type-2 fuzzy set. The secondary memberships are shown in (b) to represent the confidence of the primary memberships.

24
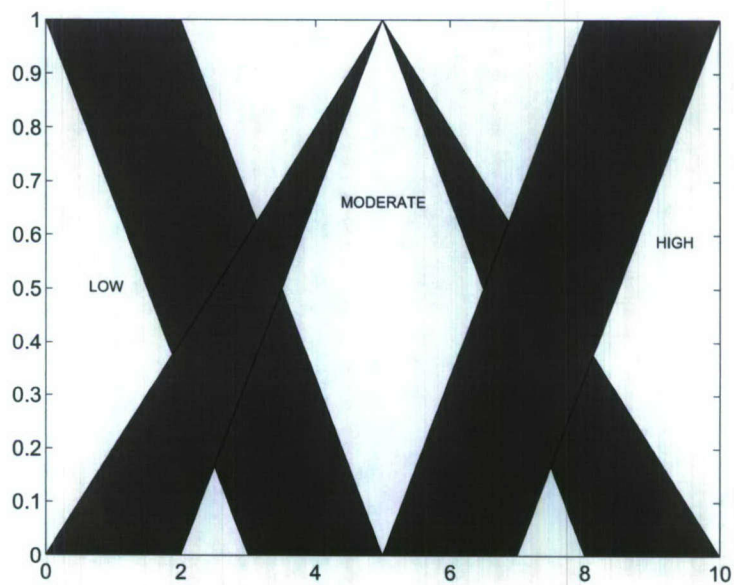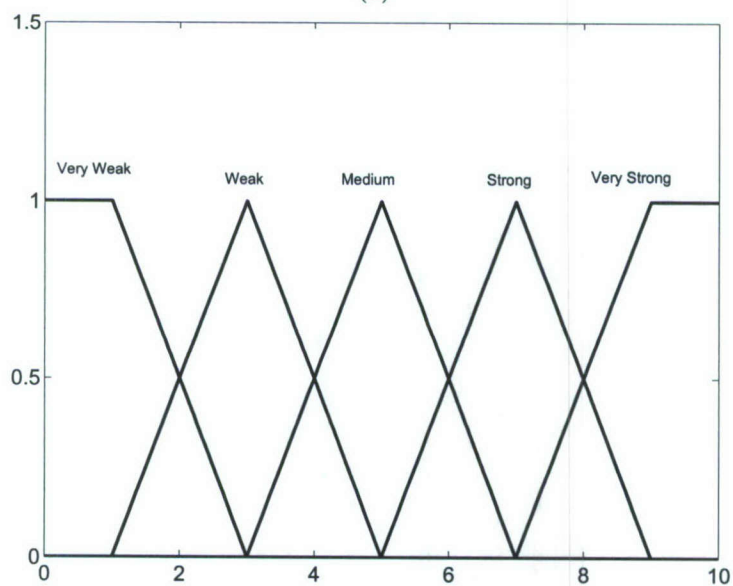
Figure 5: The MFs used to represent the linguistic labels. (a) MFs for antecedents, and (b) MFs for consequent.

25
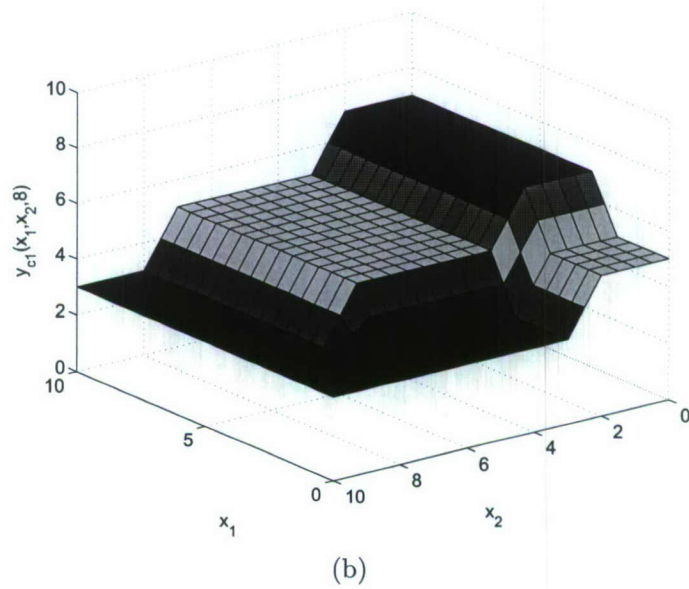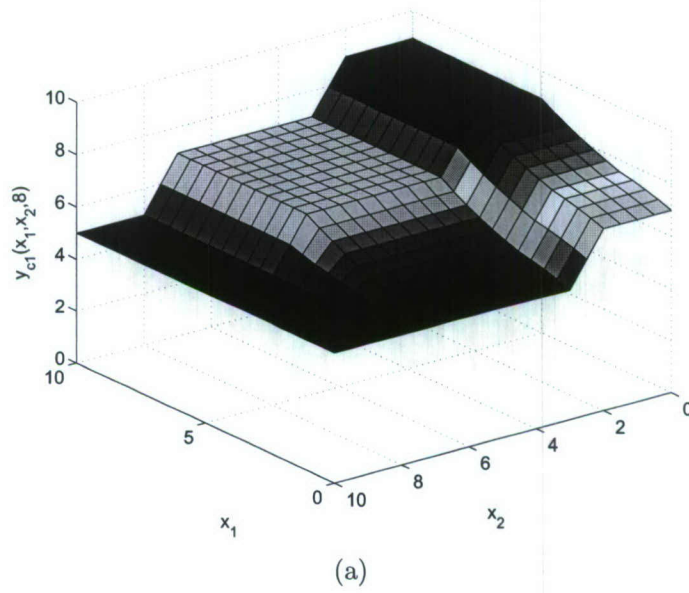
Figure 6: The threat assessment surface for different FLSs when $x_3 = 8$. (a) Favor weak FLS, and (b) Traditional type-1 FLS.

26

Cognitive Radar Sensor Networks: A Human-Inspired Information Integration and Fuzzy Logic System-Based Approach

Qilian Liang, *Senior Member, IEEE*

Dept of Electrical Engineering

University of Texas at Arlington

Arlington, TX 76019-0016, USA

E-mail: liang@uta.edu

Abstract

Inspired by human's innate ability to process and integrate information from disparate, network-based sources, we apply human-inspired information integration mechanisms to target detection in cognitive radar sensor network. Humans' information integration mechanisms have been modelled using maximum-likelihood estimation (MLE) or soft-max approaches. In this paper, we apply these two algorithms to cognitive radar sensor networks target detection. Discrete-cosine-transform (DCT) is used to process the integrated data from MLE or soft-max. We apply fuzzy logic system (FLS) to automatic target detection based on the AC power values from DCT. Simulation results show that our MLE-DCT-FLS and soft-max-DCT-FLS approaches perform very well in the radar sensor network target detection, whereas the existing 2-D construction algorithm doesn't work in this study.

Index Terms : Human-inspired, cognitive radar sensor networks, fuzzy logic systems, automatic target recognition, maximum-likelihood estimation.

1

1 Introduction and Motivation

A cognitive network is one that is aware of changes in user needs and its environment, adapts its behavior to those changes, learns from its adaptations, and exploits knowledge to improve its future behavior. A cognitive radar sensor network consists of multiple networked radar sensors and radar sensors sense and communicate with each other collaboratively to complete a mission. In real world, cognitive radar sensor network information integration is necessary in different applications. For example, in an emergency natural disaster scenario, such as Utah Mine Collapse in August 2007 or West Virginia Sago mine disaster in January 2006, cognitive radar sensor network-based information integration for first responders is critical for search and rescue. Danger may appear anywhere at any time, therefore, first responders must monitor a large area continuously in order to identify potential danger and take actions. Due to the dynamic and complex nature of natural disaster, some buried/foleage victims may not be found with image/video sensors, and UWB radar sensors are needed for penetrating the ground or sense-through-wall. Unfortunately, the radar data acquired are often limited and noisy. Unlike medical imaging or synthetic aperture radar imaging where abundance of data is generally available through multiple looks and where processing time may not be crucial, practical cognitive radar sensor networks are typically the opposite: availability of data is limited and required processing time is short. This need is also motivated by the fact that humans display a remarkable capability to quickly perform target recognition despite noisy sensory signals and conflicting inputs. Humans are adept at network visualization, and at understanding subtle implications among the network connections. To date, however, human's innate ability to process and integrate information from disparate, network-based sources for situational understanding has not translated well to automated systems. In this paper, we apply human information integration mechanisms to information fusion in cognitive radar sensor network.

2

2 Sense-through-Foliage Radar Sensor Networks Data Measurement and Collection

Our work is based on the sense-through-foliage UWB radar sensor networks. The foliage experiment was constructed on a seven-ton man lift, which had a total lifting capacity of 450 kg. The limit of the lifting capacity was reached during the experiment as essentially the entire measuring apparatus was placed on the lift. (as shown in Fig. 1). The principle pieces of equipment secured on the lift are: Barth pulser, Tektronix model 7704 B oscilloscope, dual antenna mounting stand, two antennas, rack system, IBM laptop, HP signal Generator, Custom RF switch and power supply and Weather shield (small hut). The target is a trihedral reflector (as shown in Fig. 2). Throughout this work, a Barth pulse source (Barth Electronics, Inc. model 732 GL) was used. The pulse generator uses a coaxial reed switch to discharge a charge line for a very fast rise time pulse outputs. The model 732 pulse generator provides pulses of less than 50 picoseconds (ps) rise time, with amplitude from 150 V to greater than 2 KV into any load impedance through a 50 ohm coaxial line. The generator is capable of producing pulses with a minimum width of 750 ps and a maximum of 1 microsecond. This output pulse width is determined by charge line length for rectangular pulses, or by capacitors for 1/e decay pulses.

For the data we used in this paper, each sample is spaced at 50 picosecond interval, and 16,000 samples were collected for each collection for a total time duration of 0.8 microseconds at a rate of approximately 20 Hz. We plot the transmitted pulse (one realization) in Fig. 3a) and the received echos in one collection in Fig. 3b (averaged over 35 pulses). The data collections were extensive. 20 different positions were used, and 35 collections were performed at each position using UWB radar sensor networks.

3

3 Human Information Integration Mechanisms

Recently, a maximum-likelihood estimation (MLE) approach was proposed for multi-sensory data fusion in human [4]. In the MLE approach [4], sensory estimates of an environmental property can be represented by $\hat{S}_j = f_i(S)$ where S is the physical property being estimated, f is the operation the nervous system performs to derive the estimate, and $\hat{S}$ is the perceptual estimate. Sensory estimates are subject to two types of error: random measurement error and bias. Thus, estimates of the same object property from different cues usually differ. To reconcile the discrepancy, the nervous system must either combine estimates or choose one, thereby ignoring the other cues. Assuming that each single-cue estimate is unbiased but corrupted by independent Gaussian noise, the statistically optimal strategy for cue combination is a weighted average [4]

$$\hat{S}_c = \sum_{i=1}^{M} w_i \hat{S}_i \tag{1}$$

where $w_i = \frac{1/\sigma_i^2}{\sum_j 1/\sigma_j^2}$ and is the weight given to the ith single-cue estimate, σ_i^2 is that estimates variance, and M is the total number of cues. Combining estimates by this MLE rule yields the least variable estimate of S and thus more precise estimates of object properties.

Besides, some other summation rules have been proposed in perception and cognition such as soft-max rule: $y = (\sum_{i=1}^{M} x_i^n)^{\frac{1}{n}}$ [3] where x_i denotes the input from an input source i, and M is the total number of sources. In this paper, we will apply MLE and soft-max human brain information integration mechanisms to cognitive radar sensor network information integration.

4 Human-Inspired Sense-through-Foliage Target Detection

In Figs. 4a and 4b, we plot two collections of UWB radars. Fig. 4a has no target on range, and Fig. 4b has target at samples around 13,900. We plot the echo differences between Figs. 4a and 4b in Fig. 4c. However, it is impossible to identify whether there is any target and where there is target

4

based on Fig. 4c. Since significant pulse-to-pulse variability exists in the echos, this motivate us to explore the spatial and time diversity using Radar Sensor Networks (RSN).

In RSN, the radar sensors are networked together in an ad hoc fashion. They do not rely on a preexisting fixed infrastructure, such as a wireline backbone network or a base station. They are self-organizing entities that are deployed on demand in support of various events surveillance, battlefield, disaster relief, search and rescue, etc. Scalability concern suggests a hierarchical organization of radar sensor networks with the lowest level in the hierarchy being a cluster. As argued in [7] [6] [5] [9], in addition to helping with scalability and robustness, aggregating sensor nodes into clusters has additional benefits:

1. conserving radio resources such as bandwidth;

2. promoting spatial code reuse and frequency reuse;

3. simplifying the topology, e.g., when a mobile radar changes its location, it is sufficient for only the nodes in attended clusters to update their topology information;

4. reducing the generation and propagation of routing information; and,

5. concealing the details of global network topology from individual nodes.

In RSN, each radar can provide their pulse parameters such as timing to their clusterhead radar, and the clusterhead radar can combine the echos (RF returns) from the target and clutter. In this paper, we propose a RAKE structure for combining echos, as illustrated by Fig. 5. The integration means time-average for a sample duration T and it's for general case when the echos are not in discrete values. It is quite often assumed that the radar sensor platform will have access to Global Positioning Service (GPS) and Inertial Navigation Unit (INU) timing and navigation data [1]. In this paper, we assume the radar sensors are synchronized in RSN. In Fig. 5, the echo, i.e., RF

5

response by the pulse of each cluster-member sensor, will be combined by the clusterhead using a weighted average, and the weight w_i is determined by the two human-inspired mechanisms.

We applied the human-inspired MLE algorithm to combine the sensed echo collection from $M = 30$ UWB radars, and then the combined data are processed using discrete-cosine transform (DCT) to obtain the AC values. Based on our experiences, echo with a target generally has high and nonfluctuating AC values and the AC values can be obtained using DCT. We plot the power of AC values in Figs. 6a and 6b using MLE and DCT algorithms for the two cases (with target and without target) respectively. Observe that in Fig. 6b, the power of AC values (around sample 13,900) where the target is located is non-fluctuating (somehow monotonically increase then decrease). Although some other samples also have very high AC power values, it is very clear that they are quite fluctuating and the power of AC values behaves like random noise because generally the clutter has Gaussian distribution in the frequency domain.

Similarly, we applied the soft-max algorithm ($n = 2$) to combine the sensed echo collection from $M = 30$ UWB radars, and then used DCT to obtain the AC values. We plot the power of AC values in Figs. 6a and 6b using soft-max and DCT algorithms for the two cases (with target and without target) respectively. Observe that in Fig. 7b, the power of AC values (around sample 13,900) where the target is located is non-fluctuating (somehow monotonically increase then decrease).

We made the above observations. However, in real world application, automatic target detection is necessary to ensure that our algorithms could be performed in real time. In Section 5, we apply fuzzy logic systems to automatic target detection based on the power of AC values (obtained via MLE-DCT or soft-max-DCT).

We compared our approaches to the scheme proposed in [10]. In [10], 2-D image was created via adding voltages with the appropriate time offset. In Figs. 8a and 8b, we plot the 2-D image created based on the above two data sets (from samples 13,800 to 14,200). The sensed data from

6

30 radars are averaged first, then plotted in 2-D [10]. However, it's not clear which image shows there is target on range.

5 Fuzzy Logic System for Automatic Target Detection

5.1 Overview of Fuzzy Logic Systems

Figure 9 shows the structure of a fuzzy logic system (FLS) [8]. When an input is applied to a FLS, the inference engine computes the output set corresponding to each rule. The defuzzifer then computes a crisp output from these rule output sets. Consider a p-input 1-output FLS, using singleton fuzzification, *center-of-sets* defuzzification [8] and "IF-THEN" rules of the form

$$R^l : \text{IF } x_1 \text{ is } F_1^l \text{ and } x_2 \text{ is } F_2^l \text{ and } \cdots \text{ and } x_p \text{ is } F_p^l, \text{ THEN } y \text{ is } G^l.$$

Assuming singleton fuzzification, when an input $\mathbf{x}' = \{x_1', \ldots, x_p'\}$ is applied, the degree of firing corresponding to the lth rule is computed as

$$\mu_{F_1^l}(x_1') \star \mu_{F_2^l}(x_2') \star \cdots \star \mu_{F_p^l}(x_p') = \mathcal{T}_{i=1}^p \mu_{F_i^l}(x_i') \qquad (2)$$

where $\star$ and $\mathcal{T}$ both indicate the chosen t-norm. There are many kinds of defuzzifiers. In this paper, we focus, for illustrative purposes, on the center-of-sets defuzzifier [8]. It computes a crisp output for the FLS by first computing the centroid, c_{G^l}, of every consequent set G^l, and, then computing a weighted average of these centroids. The weight corresponding to the lth rule consequent centroid is the degree of firing associated with the lth rule, $\mathcal{T}_{i=1}^p \mu_{F_i^l}(x_i')$, so that

$$y_{cos}(\mathbf{x}') = \frac{\sum_{l=1}^M c_{G^l} \mathcal{T}_{i=1}^p \mu_{F_i^l}(x_i')}{\sum_{l=1}^M \mathcal{T}_{i=1}^p \mu_{F_i^l}(x_i')} \qquad (3)$$

where M is the number of rules in the FLS. In this paper, we design a FLS for automatic target recognition based on the AC values obtained using MLE-DCT or soft-max-DCT.

7

5.2 FLS for Automatic Target Detection

Observe that in Figs. 6 and 7, the power of AC values are quite fluctuating and have lots of uncertainties. FLS is well known to handle the uncertainties. For convenience in describing the FLS design for Automatic Target Detection (ATD), we first give the definition of *footprint of uncertainty* of AC power values and *region of interest* in the footprint of uncertainty.

Definition 1 (Footprint of Uncertainty) *Uncertainty in the AC power values and time index consists of a bounded region, that we call the* footprint of uncertainty *of AC power values. It is the union of all AC power values.*

Definition 2 (Region of Interest (RoI)) *An RoI in the footprint of uncertainty is a contour consisting of a large number (greater than 50) of AC power values where AC power values increase then decrease.*

Definition 3 (Fluctuating Point in RoI) $P(i)$ *is called a* fluctuating point *in the RoI if* $P(i - 1), P(i), P(i + 1)$ *are non-monotonically increasing or decreasing.*

Our FLS for automatic target detection will classify each ROI (with target or no target) based on two antecedents: *the centroid of the ROI* and *the number of fluctuating points in the ROI*. The linguistic variables used to represent these two antecedents were divided into three levels: *low, moderate,* and *high*. The consequent – the possibility that there is a target at this RoI – was divided into 5 levels, *Very Strong, Strong, Medium, Weak, Very Weak*. We used trapezoidal membership functions (MFs) to represent *low, high, very strong,* and *very weak*; and triangle MFs to represent *moderate, strong, medium,* and *weak*. All inputs to the antecedents are normalized to 0–10.

Based on the fact the AC power value of target is non-fluctuating (somehow monotonically increase then decrease), and the AC power value of clutter behaves like random noise because

generally the clutter has Gaussian distribution in the frequency domain, we design a fuzzy logic system using rules such as:

R^l : IF *centroid of a RoI* (x_1) is F_l^1, and *the number of fluctuating points in the ROI* (x_2) is F_l^2,

THEN the possibility that there is a target at this RoI (y) is G^l.

where $l = 1, \ldots, 9$. We summarize all the rules in Table 1. For every input (x_1, x_2), the output is computed using

$$y(x_1, x_2) = \frac{\sum_{l=1}^{9} \mu_{F_l^1}(x_1) \mu_{F_l^2}(x_2) c_{avg}^l}{\sum_{l=1}^{9} \mu_{F_l^1}(x_1) \mu_{F_l^2}(x_2)} \tag{4}$$

We ran simulations to 1000 collections in the real world sense-through-foliage experiment, and found that our FLS performs very well in the automatic target detection based on the AC power values obtained from MLE-DCT or soft-max-DCT, and achieve probability of detection $p_d = 100\%$ and false alarm rate $p_{fa} = 0$.

6 Conclusions

Inspired by human's innate ability to process and integrate information from disparate, network-based sources, we applied human-inspired information integration mechanisms to target detection in cognitive radar sensor network. Humans' information integration mechanisms have been modelled using maximum-likelihood estimation (MLE) or soft-max approaches. In this paper, we applied these two algorithms to cognitive radar sensor networks target detection. Discrete-cosine-transform (DCT) was used to process the integrated data from MLE or soft-max. We applied fuzzy logic system (FLS) to automatic target detection based on the AC power values from DCT. Simulation results showed that our MLE-DCT-FLS and soft-max-DCT-FLS approaches performed very well in the radar sensor network target detection, whereas the existing 2-D construction algorithm couldn't work in this study.

9

Acknowledgement

References

[1] ONR BAA 07-017, "NET-SENTRIC Surveillance," http://www.onr.navy.mil/02/baa/.

[2] D. K. Barton, *Radar System Analysis and Modeling*, Artech House, Boston, MA, 2006.

[3] N. V. S. Graham, "Visual pattern analyzers," pp. xvi, 646, New York, NY, US: Oxford University Press, 1989.

[4] J. M. Hillis, M. O. Ernst, M. S. Banks, and M. S. Landy, "Combining sensory information: Mandatory fusion within, but not between, senses," *Science*, vol. 298, No. 5598, pp. 1627-1630, 2002.

[5] T.-C. Hou and T-J. Tsai, " An access-based clustering protocol for multihop wireless ad hoc networks," *IEEE J. Selected Areas in Communications*, vol. 19, no. 7, pp. 1201-1210, July 2001.

[6] A. Iwata, C. C. Chiang, G. Pei, M. Gerla, and T. W. Chen, " Scalable routing strategies for ad hoc networks," *IEEE J. Selected Areas in Communications*, vol. 17, pp. 1369-1379, 1999.

[7] C. R. Lin and M. Gerla, "Adaptive clustering in mobile wireless networks," *IEEE J. Selected Areas in Communications*, vol. 16, pp. 1265-1275, 1997.

10

[8] J. M. Mendel, *Uncertain Rule-Based Fuzzy Logic Systems*, Prentice-Hall, Upper Saddle River, NJ, 2001.

[9] C. E. Perkins, "Chapter 4, Cluster-Based Networks," *Ad Hoc Networking*, Edited by C. E. Perkins, pp. 75-138, Addison-Wesley, 2001.

[10] P. Withington , H. Fluhler, and S. Nag , "Enhancing homeland security with advanced UWB sensors," *IEEE Microwave Magazine*, Sept 2003.

11

List of Tables

Table 1: The rules for target detection. Antecedent 1 is *centroid of a RoI*, Antecedent 2 is *the number of fluctuating points in the ROI*, and Consequent is *the possibility that there is a target at this RoI*.

Rule #	Antecedent 1	Antecedent 2	Consequent
1	low	low	medium
2	low	moderate	weak
3	low	high	very weak
4	moderate	low	strong
5	moderate	moderate	medium
6	moderate	high	weak
7	high	low	very strong
8	high	moderate	strong
9	high	high	medium

12

List of Figures

Figure 1: This figure shows the lift with the experiment. The antennas are at the far end of the lift from the viewer under the roof that was built to shield the equipment from the elements. This picture was taken in September with the foliage largely still present. The cables coming from the lift are a ground cable to an earth ground and one of 4 tethers used in windy conditions.

13

Figure 2: The target (a trihedral reflector) is shown on the stand at 300 feet from the lift.

14

(a)

(b)

Figure 3: Transmitted pulse and received echos in one experiment. (a) Transmitted pulse. (b) Received echos.

.

15
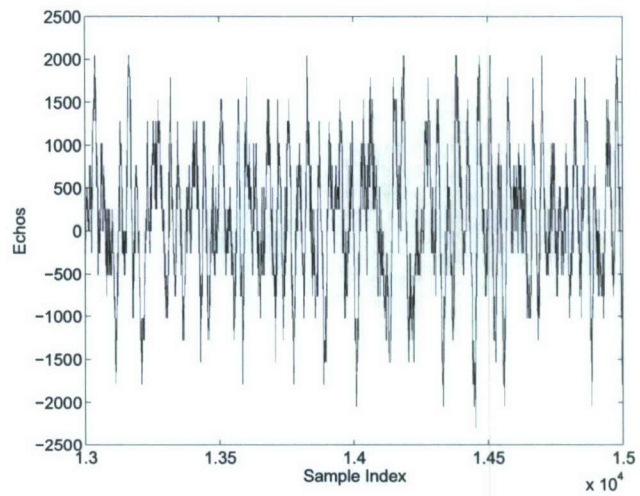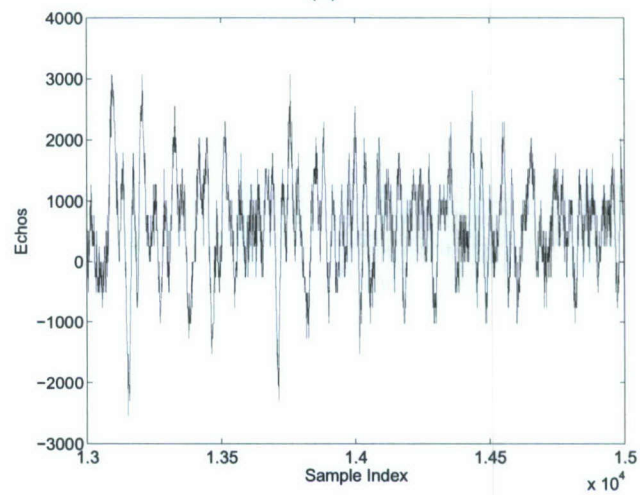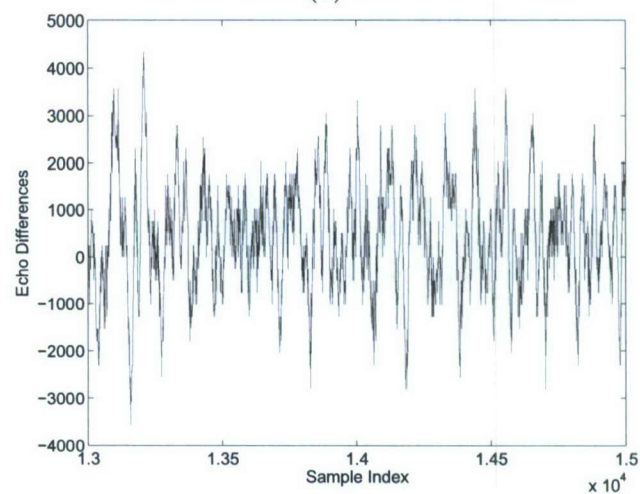
Figure 4: Measurement with 35 pulses average. (a) Expanded view of traces (no target) from sample 13,001 to 15,000. (b) Expanded view of traces (with target) from samples 13,001 to 15,000. (c) The differences between (a) and (b).

16
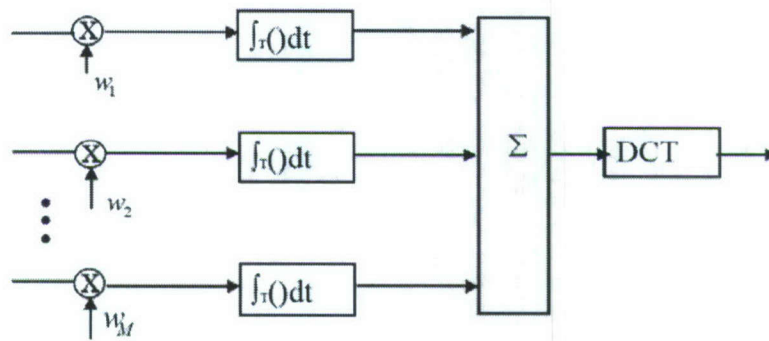
Figure 5: Echo combining by clusterhead in RSN.
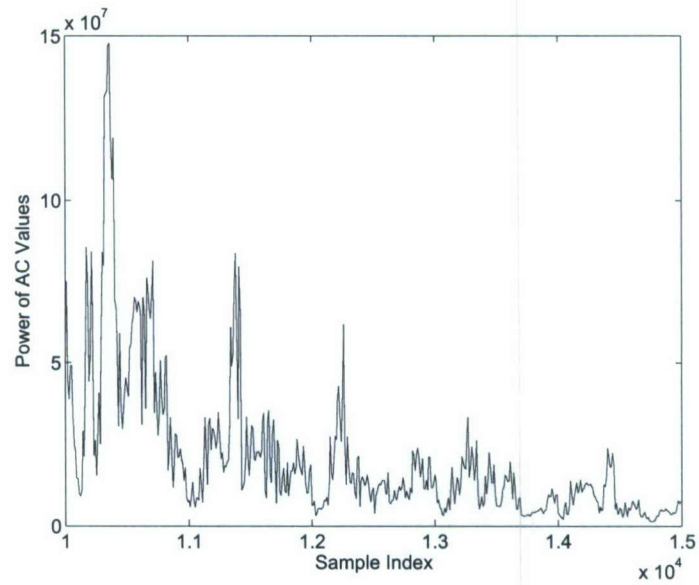
(a)
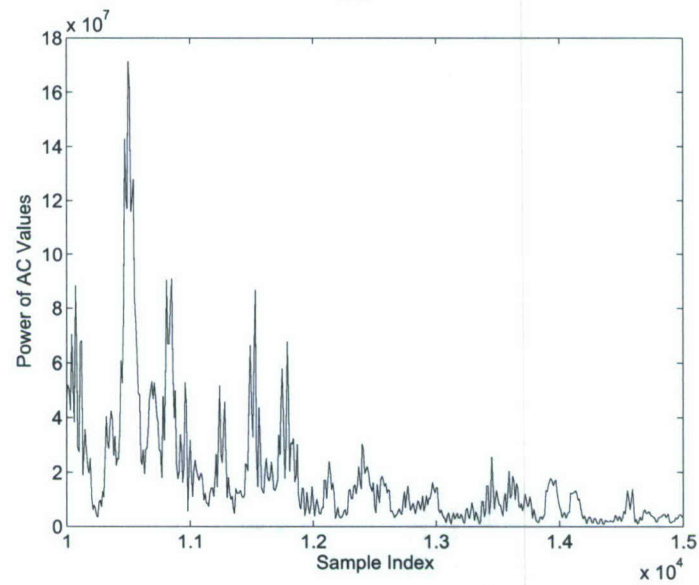
(b)

Figure 6: Power of AC values using MLE-based information integration and DCT. (a) No target (b) With target in the field.
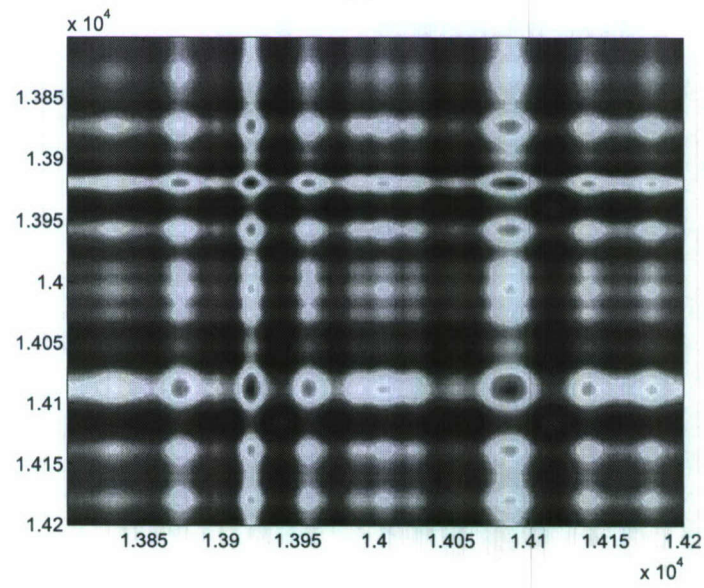
18
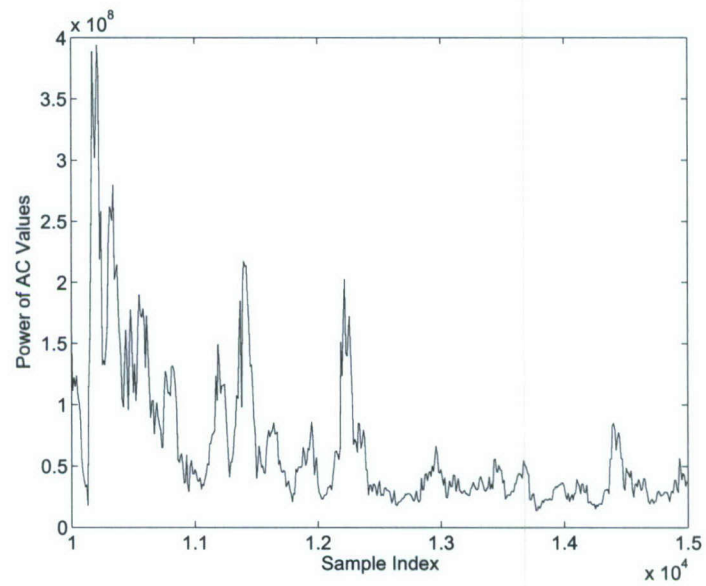
(a)
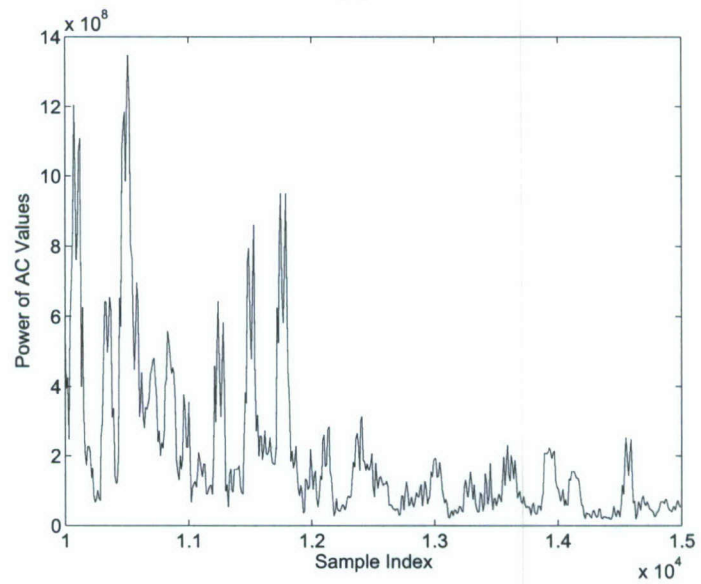
(b)

Figure 7: Power of AC values using soft-max based information integration and DCT. (a) No target (b) With target in the field.

19
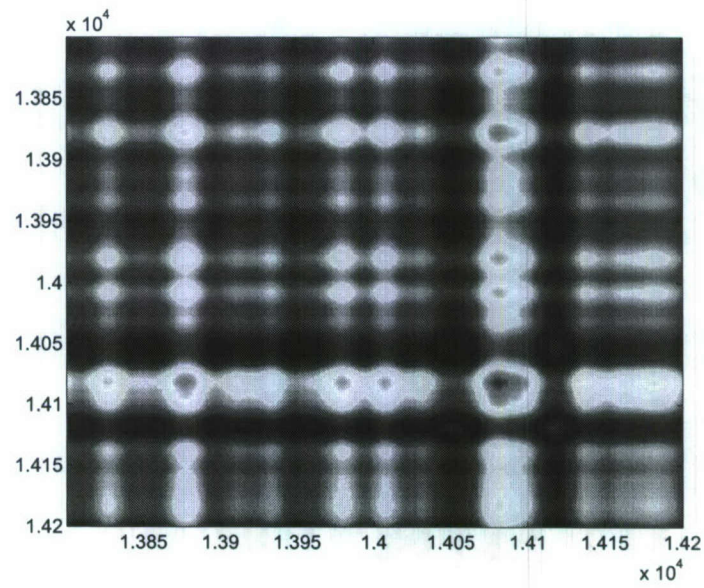
Figure 8: 2-D image created via adding voltages with the appropriate time offset. (a) No target (b) With target in the field.
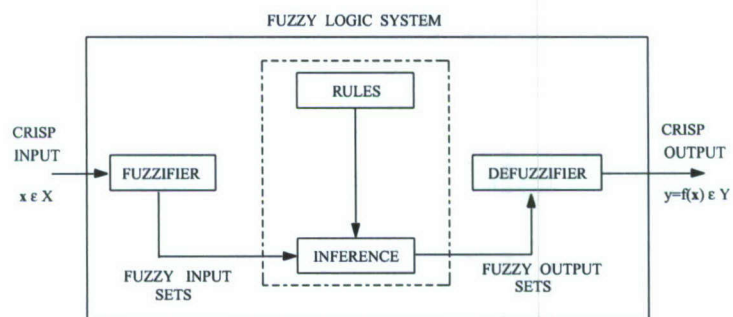
20

FUZZY LOGIC SYSTEM

RULES

CRISP
INPUT

FUZZIFIER

$x \, \varepsilon \, X$

FUZZY INPUT
SETS

INFERENCE

DEFUZZIFIER

CRISP
OUTPUT

$y = f(x) \, \varepsilon \, Y$

FUZZY OUTPUT
SETS

Figure 9: The structure of a fuzzy logic system.

21

Wireless Channel Modeling in Foliage Environment:

UWB versus Narrowband

Qilian Liang, *Senior Member, IEEE*

Dept of Electrical Engineering

University of Texas at Arlington

Arlington, TX 76019-0016, USA

E-mail: liang@uta.edu

Abstract

In this paper, we study the wireless channel modeling in foliage environment, a rich scattering and time-varying environment, based on extensive data collected using UWB and narrowband (200MHz and 400MHz) radars. We apply two approaches to the wireless channel modeling: Saleh and Valenzuela (S-V) method for UWB channel modeling and CLEAN method for narrowband and UWB channel modeling. We validated that UWB echo signals (within a burst) don't hold self-similarity, which means the future signals can't be forecasted based on the received signals and channel modeling is necessary from statistical point of view. Based on the S-V method for UWB channel modeling, in foliage UWB channel, the multi-path contributions arrive at the receiver are grouped into clusters. The time of arrival of clusters can be modeled as a Poisson arrival process, while within each cluster, subsequent multipath contributions or rays also arrive according to a Poisson process. At different field (near field, medium field, and far field), we observe that the Poisson process parameters are quite different. We also observe that the amplitude of channel coefficient at each path follows Rician distribution for medium and far field, and it's non-stationary for paths from near field (one of two Rician distributions),

1

and these observations are quite different with the IEEE indoor UWB channel model and S-V indoor channel model. Based on the CLEAN method, the narrowband (200MHz and 400MHz) and UWB channel impulse responses have many similarities: both can be modeled as linear time-variant filter channel.

1 Introduction and Motivation

The true challenge for new communication technologies is to "make the thing work" in real-world wireless channels. System designers classically focus on the impact of the radio channel on the received signals and use propagation models for testing and evaluation of receiver designs and transmission schemes. Yet, the needs for such models evolve as new applications emerge with different bandwidths, terminal mobility, higher carrier frequencies, new antennas, and so forth. Furthermore, channel characterization also yields the fundamental ties to classical electromagnetics and physics, as well as the answers to some crucial questions in communication and information theory [8]. While many efforts have been spent on indoor channel modeling as well as outdoor open space (or less scattering) environment, wireless channel modeling in foliage (forest) environment has not been studied. In Vietnam, Bosnia, Kosovo, and in the jungles of Columbia, air to ground communnications have been thwarded by the presence of foliage that protects and hides the enemy. In this paper, we study UWB and narrowband channel modeling in foliage environment.

In July 2003, the Channel Modeling sub-committee of study group IEEE 802.15.SG3a published the final report regarding the UWB indoor multipath channel model [6]. It is a modified version of the indoor Saleh and Valenzuela (S-V) channel model [10]. The S-V model was developped for NLOS channel, and it has also been applied to LOS channels where it is perhaps less valid, unless LOS components are specifically added [9] The IEEE suggested an initial set of values for the indoor UWB channel model which has range less than 10 meters. However, lots of applications

2

of UWB are for outdoor activities such as sense-through-foliage target detection. Forests favor asymmetric threats because the warfighter has a limited sensing capability. Forests provide excellent concealment from observation, ambush, and escape, as well as provide secure bases for enemy Command & Control (C2), weapons caches, and Improvised Explosive Device (IED)/ Weapon of Mass Destruction (WMD) assembly. These have become "the high ground" in fourth-generation warfare, providing a significant strategic advantage. Unfortunately, no work has been done on the outdoor UWB channel modeling.

In this paper, we will model the UWB and narrowband channels using UWB and narrowband radars in foliage environment which is a rich scattering and time-varying environment. UWB radar emissions are at a relatively low frequency-typically between 100 MHz and 3 GHz. Additionally, the fractional bandwidth of the signal is very large (greater than 0.2). Such radar sensor has exceptional range resolution that also has an ability to penetrate many common materials (e.g., walls). Law enforcement personnel have used UWB ground penetrating radars (GPRs) for at least a decade. Like the GPR, sense-through-foliage radar takes advantage of UWB's very fine resolution (time gating) and low frequency of operation.

The rest of this paper is organized as follows. In Section 2, we summarize the measurement and collection of data we used in this paper. In Section 3, we demonstrate that the UWB reflected signal in foliage environment does not hold self-similarity, and validate that outdoor channel modeling is necessary. In Section 4, we present our outdoor UWB channel model in rich scattering and time-varying environment. In Section 5, we study the channel impulse response based on CLEAN method for narrowband and UWB channels. We conclude this paper in Section 6.

3

2 Experiment Setup and Data Collection

Our work is based on the data collected in UWB radar-based sense-through-foliage experiment in late summer and fall. Late summer foliage, because of the limited rainfall, involved foliage with decreased water content. Late fall and winter measurements involved largely defoliated but dense forest, so it's a rich scattering environment. Because of wind or different temperature in dense forest, it's also a time-varying environment. The UWB radar-based experiment was constructed on a seven-ton man lift, which had a total lifting capacity of 450 kg. The limit of the lifting capacity was reached during the experiment as essentially the entire measuring apparatus was placed on the lift (as shown in Fig. 1). The principle pieces of equipment secured on the lift are: Barth pulser, Tektronix model 7704 B oscilloscope, dual antenna mounting stand, two antennas, rack system, IBM laptop, HP signal Generator, Custom RF switch and power supply and Weather shield (small hut). Throughout this work, a Barth pulse source (Barth Electronics, Inc. model 732 GL) was used. The pulse generator uses a coaxial reed switch to discharge a charge line for a very fast rise time pulse outputs. The model 732 pulse generator provides pulses of less than 50 picoseconds (ps) rise time, with amplitude from 150 V to greater than 2 KV into any load impedance through a 50 ohm coaxial line. The generator is capable of producing pulses with a minimum width of 750 ps and a maximum of 1 microsecond. This output pulse width is determined by charge line length for rectangular pulses, or by capacitors for 1/e decay pulses.

For the UWB data we used in this paper, each sample is spaced at 50 picosecond interval, and 16,000 samples were collected for each collection for a total time duration of 0.8 microseconds at a rate of approximately 20 Hz. The Barth pulse source was operated at low amplitude and 35 pulses reflected signal were averaged for each collection. Significant pulse-to-pulse variability was noted for these collections. We plot the transmitted pulse (one realization) in Fig. 2a) and the received echos in one collection in Fig. 2b (averaged over 35 pulses).

4

For comparison, we also studied narrowband (200MHz and 400MHz) radar signal propagation. Henry Radio preamplifiers were model 50B-200 and 50B-400 for 200MHz and 400MHz respectively. The Henry Radio power amplifiers were TEMPO-2002A and TEMPO-2400A for 1 KW pulsed at 200MHz and 400MHz respectively. The amplifier was speced at a minimum bandwidth of 2 MHz around it center frequency. The source for 200MHz and 400MHz narrow band wave signal was an Agilent 8648A signal generator. For the data we used in this paper, each sample is spaced at 50 picosecond interval, and 16,000 samples were collected for each collection for a total time duration of 0.8 microseconds at a rate of approximately 20 Hz. Fig. 3a shows the transmitted signal and Fig. 3b shows the received echos (averaged over 35 pulses) for 200MHz narrowband radar. Fig. 4a shows the transmitted signal and Fig. 4b shows the received echos (averaged over 35 pulses) for 400MHz narrowband radar. The data collections were extensive. 20 different positions were used, and 35 collections were performed at each position for UWB, 200MHZ, and 400MHz radars.

3 Self-Similarity Properties of UWB Reflected Signals

It has been observed that ethernet video/voice/data traffic have self-similarity [7] [4] [13]. According to Stallings [12], "Self-similarity is such an important concept that, in a way, it is surprising that only recently has it been applied to data communications traffic analysis.", and "Since 1993, a number of studies reported in the literature have documented that the pattern of data traffic is well modeled by self-similar processes in a wide variety of real-world networking situations." Such self-similarity is quite common in both natural and human-made phenomena [12] such as the distribution of earthquakes, ocean waves, fluctuation of the stock market. But the self-similarity of UWB signals has not been studied.

For a detailed discussion on self-similarity in time-series, see [13] [12]. Here we briefly present its definition [3]. Given a zero-mean, stationary time-series $X = (X_t; t = 1, 2, 3, \cdots)$, we define

5

the m-aggregated series $X^{(m)} = (X_k^{(m)}; k = 1, 2, 3, \cdots)$ by summing the original series X over nonoverlapping blocks of size m. Then it's said that X is H-self-similar, if, for all positive m, $X^{(m)}$ has the same distribution as X rescaled by m^H. That is,

$$X_t \stackrel{\triangle}{=} m^{-H} \sum_{i=(t-1)m+1}^{tm} X_i \ \forall m \in N \tag{1}$$

If X is H-self-similar, it has the same autocorrelation function $r(k) = E[(X_t - \mu)(X_{t+k} - \mu)]/\sigma^2$ as the series $X^{(m)}$ for all m, which means that the series is distributionally self-similar: the distribution of the aggregated series is the same as that of the original.

Self-similar processes can show *long-range dependence*. A process with long-range dependence has an autocorrelation function $r(k) \sim k^{-\beta}$ as $k \to \infty$, where $0 < \beta < 1$. The degree of self-similarity can be expressed using *Hurst* parameter $H = 1 - \beta/2$. For self-similar series with long-range dependence, $1/2 < H < 1$. As $H \to 1$, the degree of both self-similarity and long-range depence increases.

One method that has been widely used to verify self-similarity is the *variance-time plot*, which relies on the slowly decaying variance of a self-similar series. The variance of $X^{(m)}$ is plotted against m on a log-log plot, and a straight line with slope $(-\beta)$ greater than -1 is indicative of self-similarity, and the parameter H is given by $H = 1 - \beta/2$. We use this method in this paper. In Fig. 5, we plot the variance of $X^{(m)}$ against m on a log-log plot for 10 different UWB data collections. From this figure, it's very clear that **the UWB signal does not has self-similarity** because its trace has slope lower than -1. This conclusion means that we can't use current received signals to forecast future reflected signals within one collection, so channel modeling is very important to UWB outdoor channel because the charateristics of the future reflected signal could be known in advance if its channel can be modelled.

6

4 UWB Channel Modeling Based on S-V Approaches

4.1 Introduction to Channel Modeling for Indoor UWB Channel

In the S-V model [10], the arrival of clusters is modelled as a Poisson arrival process with a rate Λ, while within each cluster, subsequent multipath contributions or rays also arrive according to a Poisson process with a rate λ (see Fig. 7). In the S-V model, the magnitude of the k-th path within the l-th cluster follows a Rayleigh distribution, and the phase of each path is assumed to be a statistically independent random variable over $[0, 2\pi)$. Besides, the average Power Decay Profile (PDP) is characterized by an exponential decay of the amplitude of the clusters, and a different exponential decay for the amplitude of the received pulses within each cluster, as shown in Fig. 8. In the IEEE UWB indoor channel model [6], the cluster approach was adopted (same as S-V model), but a log-normal distribution was suggested for characterizing the multi-path gain amplitude, and an additional log-normal variable was introduced for representing the fluctuations of the total multipath gain. Besides, the phase of each path is assumed to be either 0 or π with equal probability.

4.2 Outdoor UWB Channel Modeling

4.2.1 Cluster Arrival and Power Decay Profile

We study the outdoor UWB signal propagation in three cases: near field (less than $55m$), medium field ($55m$–$85m$), and far field (above $85m$ and up to $120m$ in this study). In the data collection, each sample is spaced at 50 picosecond interval, so these cases are corresponding to samples 1–7333 for near field, samples 7333–11333 for medium field, and samples 11334–16000 for far field. In Fig. 6, we plot the power profile of the received echos (averaged over 30 collections to eliminate the effect of random noise and each collection was averaged based on 35 pulses) for the three different

7

cases. Since the transmitted pulse (as plotted in Fig. 2a) is a very narrow impulse pulse (like a delta function in time domain), we analyzed the channel property based on the received echos power profile plotted in Fig. 6, and similar methodology was also used in S-V model studies [10].

Observe Fig. 6, multi-path contributions arrive at the receiver grouped into clusters. The time of arrival of clusters can be modeled as a Poisson arrival process with a rate Λ, while within each cluster, subsequent multipath contributions or rays also arrive according to a Poisson process with a rate λ (see Fig. 7). We define:

- T_l = the arrival time of the first path of the l-th cluster;

- $\tau_{k,l}$ = the delay of the k-th path within the l-th cluster relative to the first path arrival time T_l;

- Λ = the cluster arrival rate;

- λ = the ray arrival rate, i.e., the arrival rate of the paths within each cluster.

By definition, we have $\tau_{0l} = T_l$. The distributions of the cluster arrival time and the ray arrival time are given by

$$p(T_l|T_{l-1}) = \Lambda \exp\left(-\Lambda(T_l - T_{l-1}), l > 0\right.$$

$$p(\tau_{k,l}|\tau_{(k-1),l}) = \lambda \exp\left(-\lambda(\tau_{k,l} - \tau_{(k-1),l})\right), k > 0 \tag{2}$$

The above observations are very similar as that for the indoor UWB channel. Specifically, we also observed the Λ and λ are quite different for three different cases.

- Observe Fig. 6a for near field, Λ (1/ns) is around 0.02 (one cluster in every $50ns$ or 1000 samples), and λ (1/ns) is around 0.4 (one path in every $2.5ns$ or 50 samples). Perhaps it's because some major scatters in near field (such as tree stems) reflected signals, so some paths are quite dominant.

8

- Observe Fig. 6b for medium field, clusters arrive quite often. Λ (1/ns) is around 0.05 (one cluster in every $20ns$ or 400 samples), and λ (1/ns) is around 1 (one path in every $1ns$ or 20 samples).

- Observe Fig. 6c for far field, clusters almost always arrive (because of rich scattering), so Λ (1/ns) is around 0.5 (one cluster in every $2ns$ or 20 samples), and λ (1/ns) is around 4 (one path in every $250ps$ or 5 samples). Perhaps it's because of rich scattering, every path has very similar power level.

Besides, the average PDP can be represented by an exponential decay of the amplitude of the clusters, and a different exponential decay for the amplitude of the received pulses within each cluster, as shown in Fig. 8.

4.2.2 Statistical Distribution of Channel Coefficients

We also study the statistical distributions of each given path. We plot the histogram for some sample values of the above three cases based on 30 collections and each collection is averaged over 35 pulses. Near field samples are based on samples 5001–6000; medium field samples are based on samples 8001–9000; and far field samples are based on samples 12001–13000. Since the samples are very close (within 7.5m distance), so their path-loss effect can be ignored. For each case, we have 30000 samples, and we plot their histogram in Fig. 9.

First, observe Fig. 9c for far field, the histogram can be almost perfectly modelled by a non-zero-mean Gaussian distribution, which means the amplitude of the channel coefficient follows a Rician distribution,

$$p_\alpha(x) = \frac{x}{\sigma^2} \exp\{-\frac{x^2 + s^2}{2\sigma^2}\} I_0(\frac{xs}{\sigma^2}) \quad x \geq 0 \tag{3}$$

where s is the mean value of Gaussian and $I_0(\cdot)$ is the zero order modified Bessel function. This kind of channel is known as Rician fading channel. A Rician channel is characterized by two

9

parameters, Rician factor K which is the ratio of the direct path power to that of the multipath, i.e., $K = s^2/2\sigma^2$, and the Doppler spread (or single-sided fading bandwidth) f_d. Similarly, Fig. 9b for medium field, the histogram can be approximately modelled by a non-zero-mean Gaussian distribution, which means the amplitude of the channel coefficient follows a Rician distribution. Observe Fig. 9a for near field, the histogram can be approximately modelled by two non-zero-mean Gaussian distributions, which means it's non-stationary, and the amplitude of the channel coefficient follows one of two Rician distributions. **The above observations are quite different with the indoor UWB channel model (log-normal distribution) and S-V model (Rayleigh distribution).** The sign of channel coefficient is either +1 or -1, i.e., its phase is either 0 or π, which matches the IEEE indoor UWB channel model.

5 Wireless Channel Modeling Based on CLEAN Method

We apply the CLEAN algorithm to obtain the UWB channel model based on the transmitted pulses and received echos. The CLEAN algorithm was first introduced in [5] and has been applied to UWB measurements [2][11] and it assumes that the channel is a series of impulses which is consistent with the tapped-delay line channel model. This algorithm searches the received echos iteratively with the template to find the maximum correlation [1]. The steps are [9]:

1. Calculate the autocorrelation of the template $r_{ss}(t)$ and the cross-correlation of the template with the received waveform $r_{sy}(t)$.

2. Find the largest correlation peak in $r_{sy}(t)$, record the normalized amplitudes α_k and relative time delay τ_k of the correlation peak.

3. Subtract $r_{ss}(t)$ scaled by α_k from $r_{sy}(t)$ at the time delay τ_k.

4. If a stopping criterion (e.g., a minimum threshold on the peak correlation) is not met, go to

10

step 2. Otherwise stop.

Based on the CLEAN method, we successfully obtained the channel impulse responses for all transmit waveforms and receive echoes. For illustration purposes, in Figs. 10, 11, and 12, we plot the channel impulse responses for 200MHz, 400MHz, and UWB channels using CLEAN method in two experiments. Observe that for all channels, channel impulse responses have many similarities: all can be modeled as linear time-variant filter channel, which is a more general case of the S-V model.

6 Conclusions

In this paper, we studied the statistical modeling for outdoor wireless channels (200MHz, 400MHz, and UWB) in rich scattering and time-varying environment based on extensive data collected using narrowband and UWB radars. We validated that UWB echo signals (within a burst) don't hold self-similarity, which means the future signals can't be forecasted based on the received signals and channel modeling is necessary from statistical point of view. In outdoor UWB channel, the multi-path contributions arrive at the receiver are grouped into clusters. The time of arrival of clusters can be modeled as a Poisson arrival process, while within each cluster, subsequent multipath contributions or rays also arrive according to a Poisson process. At different field (near field, medium field, and far field), we observed that the Poisson process parameters are quite different. We also observed that the amplitude of channel coefficient at each path follows Rician distribution for medium and far field, and it's non-stationary for paths from near field (one of two Rician distributions), and these observations are quite different with the IEEE indoor UWB channel model and S-V model. Using CLEAN method, we observed that for all channels, channel impulse responses have many similarities: all can be modeled as linear time-variant filter channel, which is a more general case of the S-V model.

11

Acknowledgement

References

[1] R. M. Buehrer, et al, "Characterization of the UWB channel," *IEEE Conf on Ultra Wideband Systems and Technologies*, pp. 26-31, Reston, VA, Nov 2003.

[2] R. J.-M. Cramer, *An Evaluation of Ultrawideband Propagation Channels*, Ph.D Dissertation, USC, 2000.

[3] M. E. Crovella and A. Bestavros, "Self-similarity in world wide web traffic: evidence and possible causes," *IEEE Trans. on Networking*, vol. 5, no. 6, pp. 835-846, Dec 1997.

[4] M. W. Garrett and W. Willinger, "Analysis, modeling and generation of self-similar VBR video traffic," *SIGCOMM'94*, pp. 269-280, Aug. 1994, London, UK.

[5] J. A. Hogbom, "Aperture synthesis with a non-regular distribution of interferometer baseline," *Atronomy and Astrophysics Supplement Ser.*, vol. 15, 1974.

[6] IEEE 802.15.SG3a, "Channel modeling sub-committee report final," *IEEE P802.15-02/490r1-SG3a*, Feb 2003.

[7] W. E. Leland, M. S. Taqqu, W. Willinger, and D. V. Wilson, " On the self-similar nature of ethernet traffic," *IEEE Trans. on Networking*, vol. 2, no. 1, pp. 1-15, Feb 1994.

12

[8] C. Oestges, et. al, "Call for Paper: Special Issue on Advances in Propagation Modelling for Wireless Systems," *EURASIP J on Wireless Communications and Networking*, 2008.

[9] J. H. Reed, *An Introduction to Ultra Wideband Communication Systems*, Prentice Hall, Upper Saddler River, NJ, 2005.

[10] A. A. Saleh and R. A. Valenzuela, "A statistical model for indoor multipath propagation," *IEEE J. on Selected Areas in Communications*, vol. 5, no. 2, pp. 128-137, Feb 1987.

[11] R. A. Scholtz, M. Z. Win, and J. M. Cramer, "Evaluation of the Characteristics of the ultra-wideband propagation channel," *Proc of Antenna and Propagation Symposium*, vol. 2, no. 626-630, 1998.

[12] W. Stallings, *High-Speed Networks: TCP/IP and ATM Design Principles*, Upper Saddle River, NJ, 1998.

[13] W. Willinger, M. S. Taqqu, R. Sherman, and D. V. Wilson, "Self-similarity through high-variability: statistical analysis of ethernet LAN traffic at the source level," *IEEE Trans. on Networking*, vol. 5, no. 1, pp. 71-86, Feb 1997.

13

List of Figures
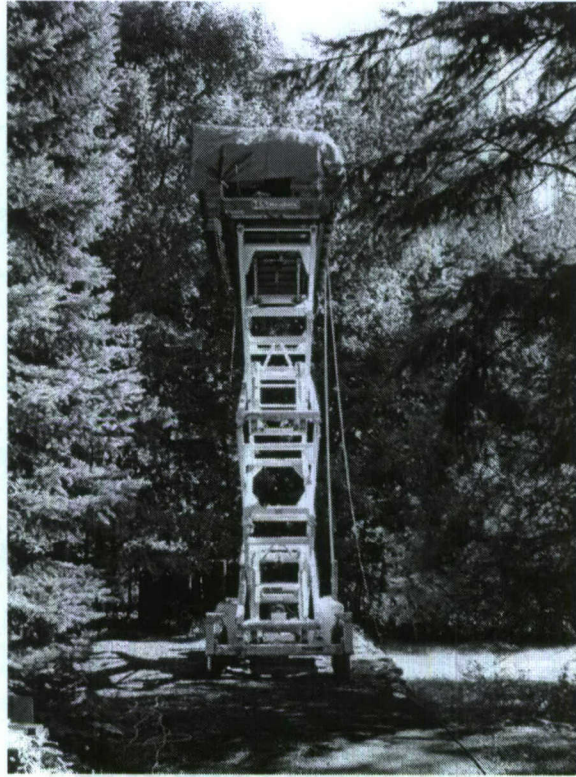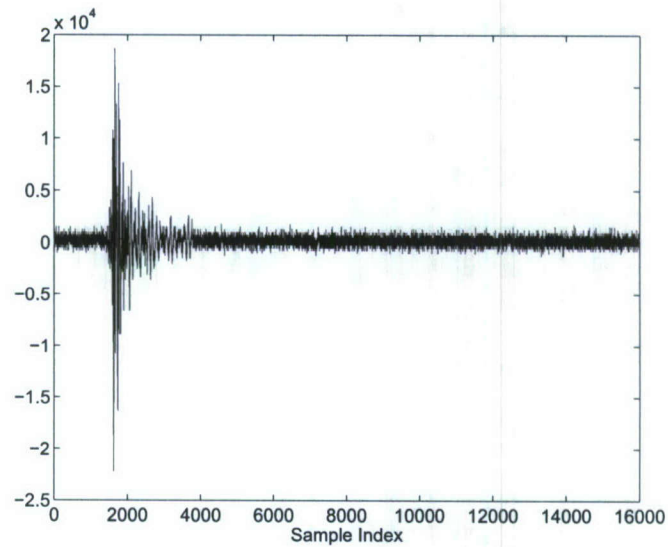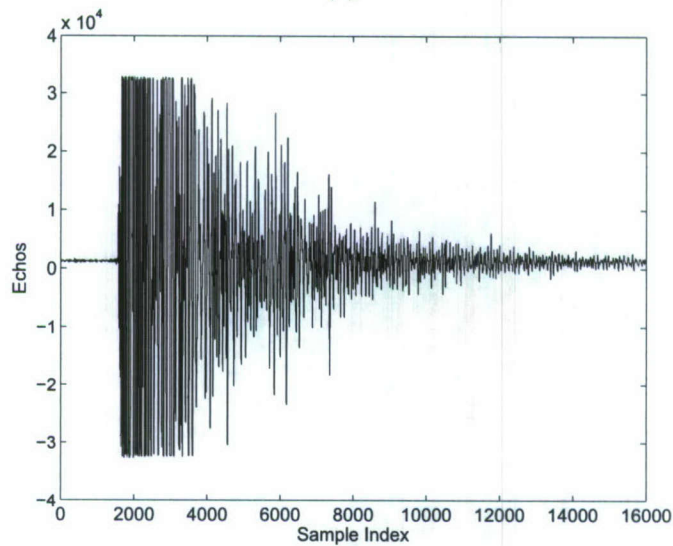
List of Figures : 1

List of Figures : 2

Figure 1: This figure shows the lift with the experiment. The antennas are at the far end of the lift from the viewer under the roof that was built to shield the equipment from the elements. This picture was taken in September with the foliage largely still present. The cables coming from the lift are a ground cable to an earth ground and one of 4 tethers used in windy conditions.
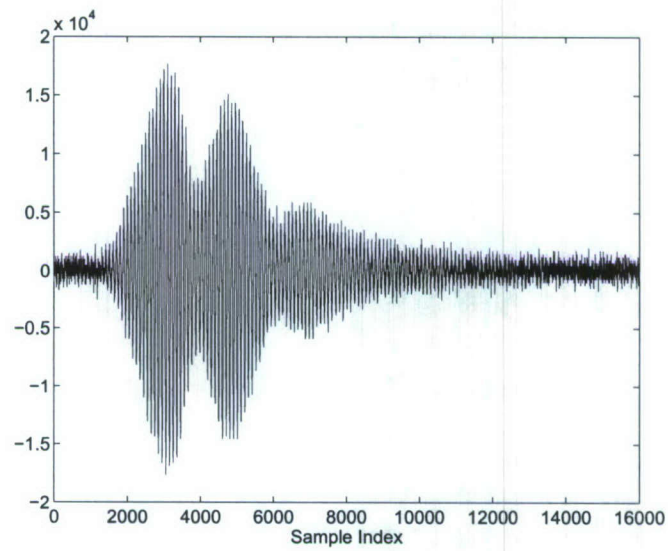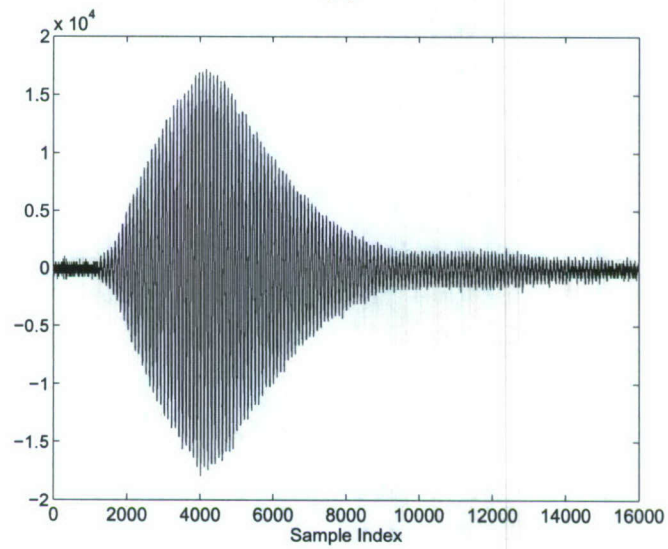
14

(a)

(b)

Figure 2: UWB radar Transmitted pulse and received echos in one experiment. (a) Transmitted pulse. (b) Received echos.
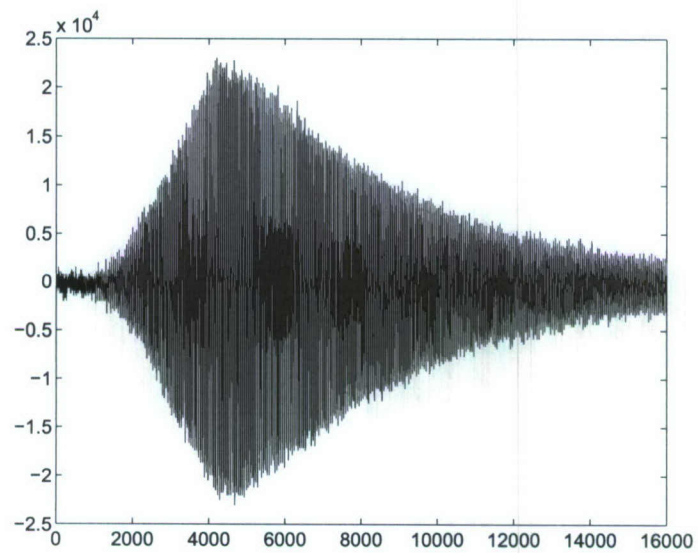
.

15
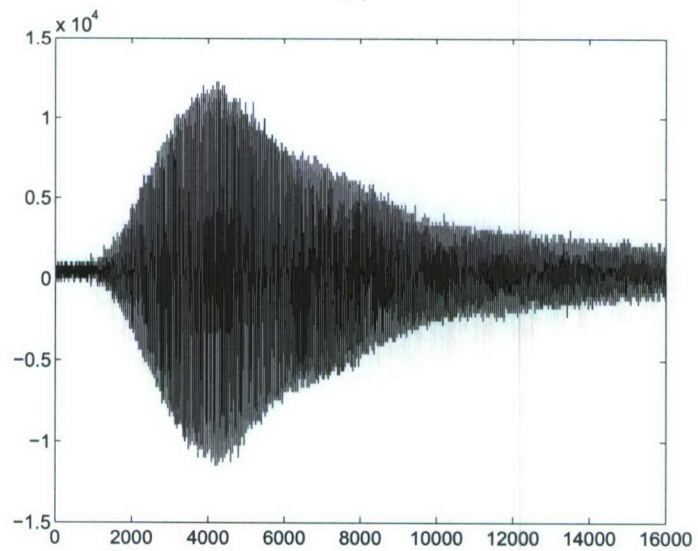
Figure 3: Narrowband radar (200MHz) transmitted pulse and received echos in one experiment. (a) Transmitted pulse. (b) Received echos.

16

Figure 4: Narrowband radar (400MHz) transmitted pulse and received echos in one experiment. (a) Transmitted pulse. (b) Received echos.
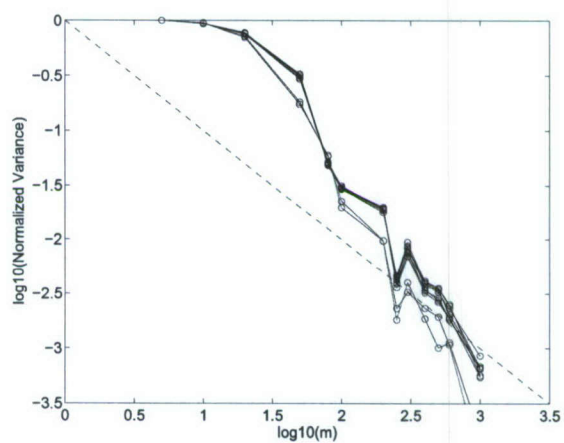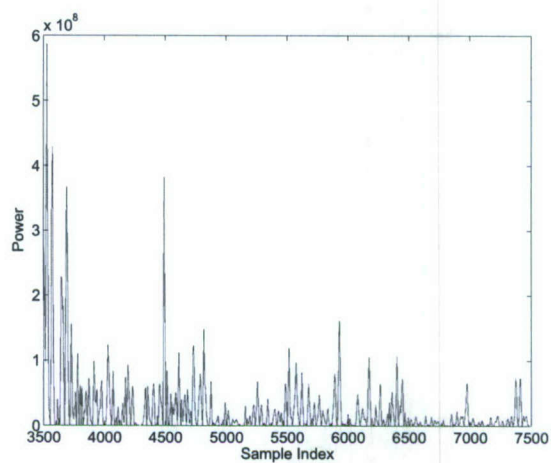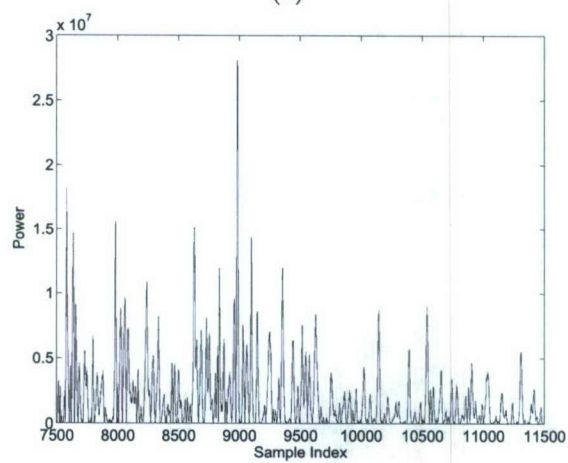
17

Figure 5: The *variance-time* plot of 10 UWB data collections, which demonstrates that UWB reflected signals are not self-similar within each collection.

18
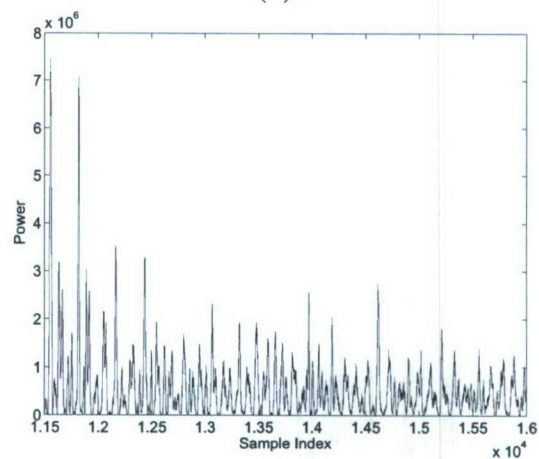
Figure 6: The power profile for three different cases: (a) near field, (b) medium field, and (c) far field.

19
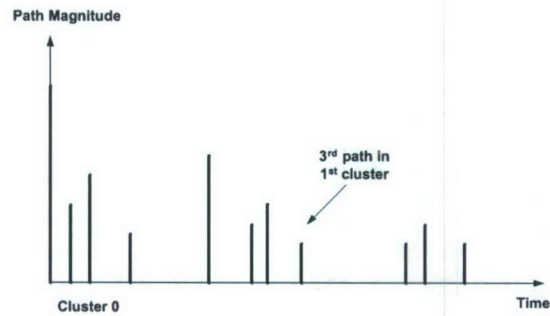
Figure 7: An illustration of the channel impulse response in S-V model.
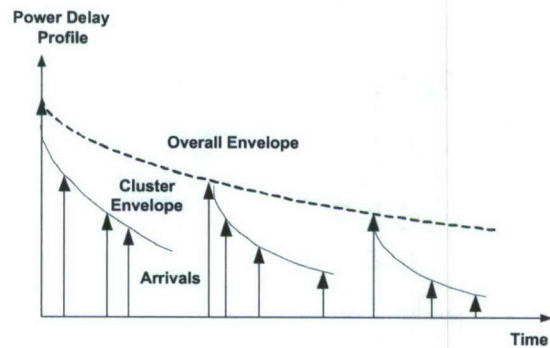
Figure 8: An illustration of the double exponential decay of the mean cluster power and the ray power within clusters in S-V model.

20
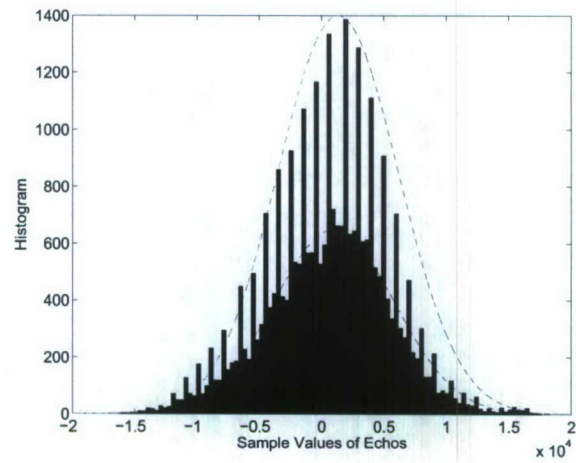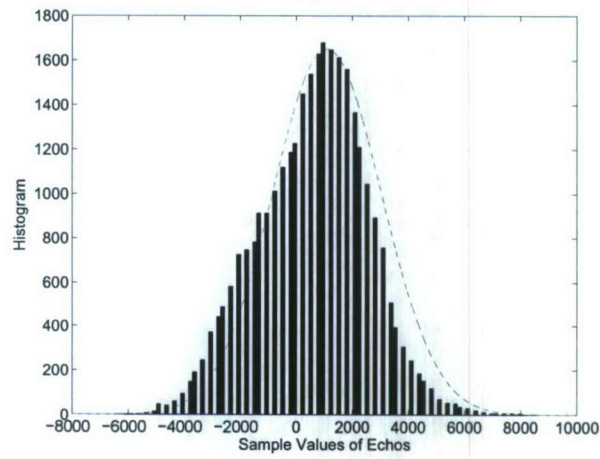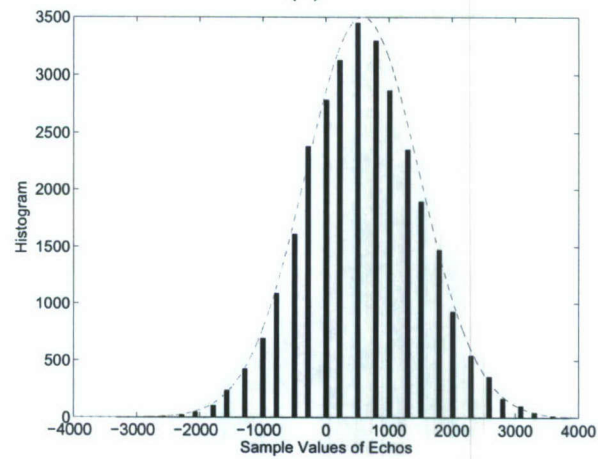
Figure 9: The histograms and their approximation using Gaussian distributions (dashed lines). The histograms are based on 30 collections and each collection is averaged over 35 pulses. (a) near field samples, (b) medium field samples, and (c) far field samples.

21
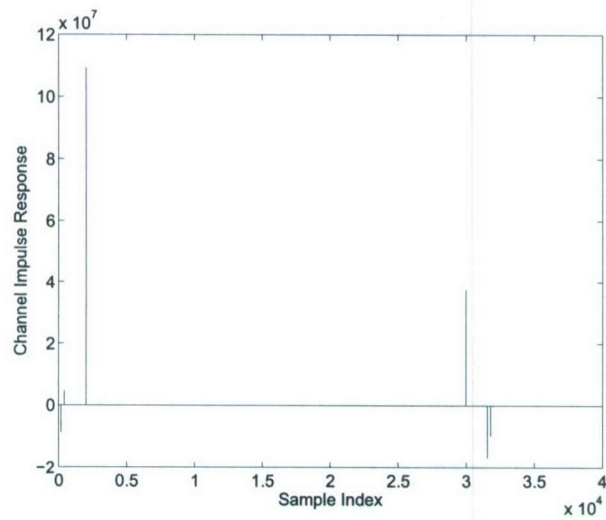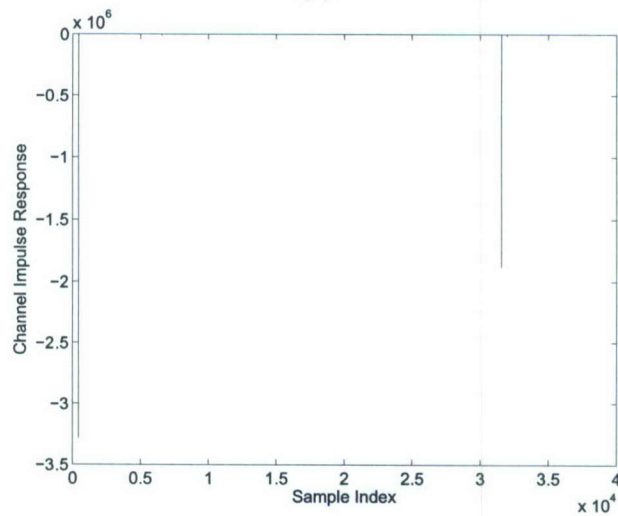
Figure 10: The channel impulse responses for 200MHz channel using CLEAN method in two experiments.

22
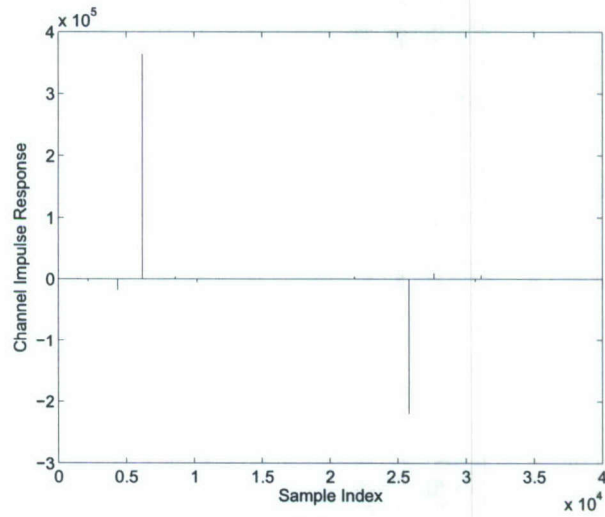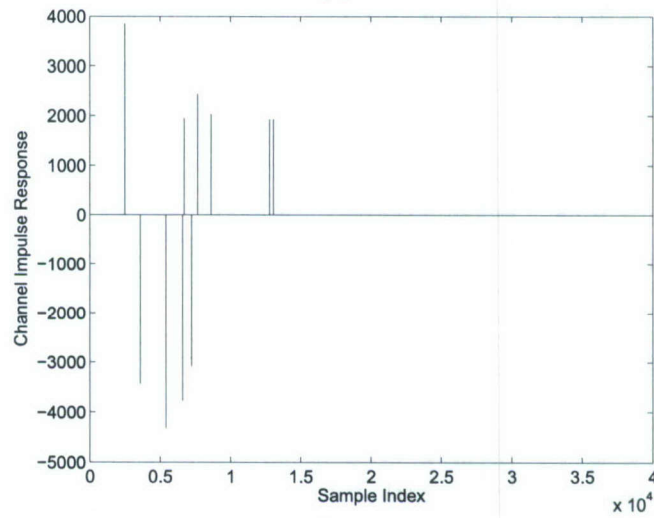
Figure 11: The channel impulse responses for 400MHz channels using CLEAN method in two experiments.

23
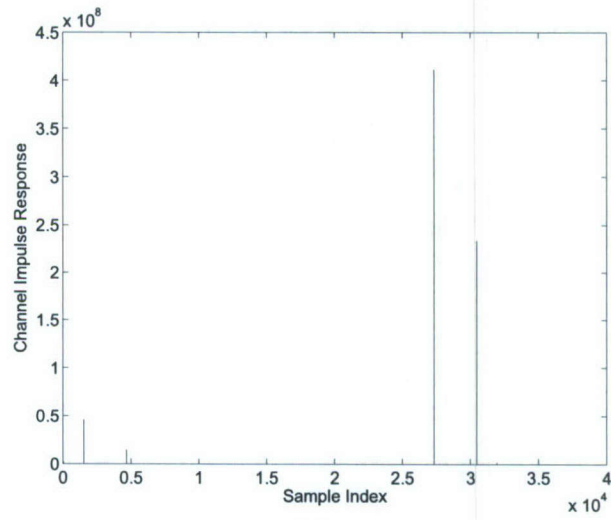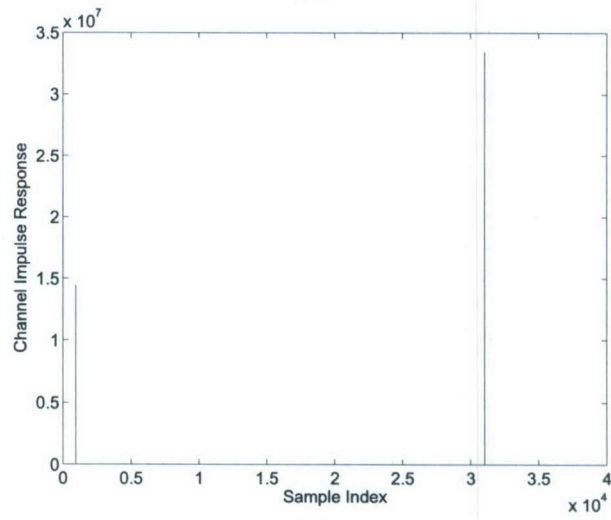
Figure 12: The channel impulse responses for UWB channels using CLEAN method in two experiments.

24

Human-Inspired Information Integration for UWB[1] Radar Sensor Networks

Qilian Liang
Department of Electrical Engineering
University of Texas at Arlington
Arlington, TX 76019-0016, USA
E-mail: liang@uta.edu

Abstract—**Inspired by human's innate ability to process and integrate information from disparate, network-based sources, we apply human-inspired information integration mechanisms to target detection in UWB radar sensor network. Humans' information integration mechanisms have been modelled using maximum-likelihood estimation (MLE) or soft-max approaches. In this paper, we apply these two algorithms to cognitive radar sensor networks target detection. Discrete-cosine-transform (DCT) is used to process the integrated data from MLE or soft-max. We apply fuzzy logic system (FLS) to automatic target detection based on the AC power values from DCT. Simulation results show that our MLE-DCT-FLS and soft-max-DCT-FLS approaches perform very well in the radar sensor network target detection, whereas the existing 2-D construction algorithm doesn't work in this study.**

Index Terms : Human-inspired, UWB radar sensor networks, fuzzy logic systems, automatic target recognition, maximum-likelihood estimation.

I. INTRODUCTION AND MOTIVATION

In real world, UWB radar sensor network information integration is necessary in different applications. For example, in an emergency natural disaster scenario, such as Utah Mine Collapse in August 2007 or West Virginia Sago mine disaster in January 2006, UWB radar sensor network-based information integration for first responders is critical for search and rescue. Danger may appear anywhere at any time, therefore, first responders must monitor a large area continuously in order to identify potential danger and take actions. Due to the dynamic and complex nature of natural disaster, some buried/foleage victims may not be found with image/video sensors, and UWB radar sensors are needed for penetrating the ground or sense-through-wall. Unfortunately, the radar data acquired are often limited and noisy. Unlike medical imaging or synthetic aperture radar imaging where abundance of data is generally available through multiple looks and where processing time may not be crucial, practical cognitive radar sensor networks are typically the opposite: availability of data is limited and required processing time is short. This need is also motivated by the fact that humans display a remarkable capability to quickly perform target recognition despite noisy sensory signals and conflicting inputs. Humans are adept at network visualization, and at understanding subtle implications among the network connections. To date, however, human's innate ability to process and integrate information from disparate, network-based sources for situational understanding has not translated well to automated systems. In this paper, we apply human information integration mechanisms to information fusion in UWB radar sensor network.

II. SENSE-THROUGH-FOLIAGE RADAR SENSOR NETWORKS DATA MEASUREMENT AND COLLECTION

Our work is based on the sense-through-foliage UWB radar sensor networks. The foliage experiment was constructed on a seven-ton man lift, which had a total lifting capacity of 450 kg. The limit of the lifting capacity was reached during the experiment as essentially the entire measuring apparatus was placed on the lift. The principle pieces of equipment secured on the lift are: Barth pulser, Tektronix model 7704 B oscilloscope, dual antenna mounting stand, two antennas, rack system, IBM laptop, HP signal Generator, Custom RF switch and power supply and Weather shield (small hut). The target is a trihedral reflector (as shown in Fig. 1). Throughout this work, a Barth pulse source (Barth Electronics, Inc. model 732 GL) was used. The pulse generator uses a coaxial reed switch to discharge a charge line for a very fast rise time pulse outputs. The model 732 pulse generator provides pulses of less than 50 picoseconds (ps) rise time, with amplitude from 150 V to greater than 2 KV into any load impedance through a 50 ohm coaxial line. The generator is capable of producing pulses with a minimum width of 750 ps and a maximum of 1 microsecond. This output pulse width is determined by charge line length for rectangular pulses, or by capacitors for 1/e decay pulses.

For the data we used in this paper, each sample is spaced at 50 picosecond interval, and 16,000 samples were collected for each collection for a total time duration of 0.8 microseconds at a rate of approximately 20 Hz. We plot the transmitted pulse (one realization) in Fig. 2a) and the received echos in one collection in Fig. 2b (averaged over 35 pulses).

Fig. 1. The target (a trihedral reflector) is shown on the stand at 300 feet from the lift.

Fig. 2. Transmitted pulse and received echos in one experiment. (a) Transmitted pulse. (b) Received echos.

III. HUMAN INFORMATION INTEGRATION MECHANISMS

Recently, a maximum-likelihood estimation (MLE) approach was proposed for multi-sensory data fusion in human [4]. In the MLE approach [4], sensory estimates of an environmental property can be represented by $\hat{S}_j = f_i(S)$ where S is the physical property being estimated, f is the operation the nervous system performs to derive the estimate, and $\hat{S}$ is the perceptual estimate. Sensory estimates are subject to two types of error: random measurement error and bias. Thus, estimates of the same object property from different cues usually differ. To reconcile the discrepancy, the nervous system must either combine estimates or choose one, thereby ignoring the other cues. Assuming that each single-cue estimate is unbiased but corrupted by independent Gaussian noise, the statistically optimal strategy for cue combination is a weighted average [4]

$$\hat{S}_c = \sum_{i=1}^{M} w_i \hat{S}_i \qquad (1)$$

where $w_i = \frac{1/\sigma_i^2}{\sum_j 1/\sigma_j^2}$ and is the weight given to the ith single-cue estimate, σ_i^2 is that estimates variance, and M is the total number of cues. Combining estimates by this MLE rule yields the least variable estimate of S and thus more precise estimates of object properties.

Besides, some other summation rules have been proposed in perception and cognition such as soft-max rule: $y = \left(\sum_{i=1}^{M} x_i^n\right)^{\frac{1}{n}}$ [3] where x_i denotes the input from an input source i, and M is the total number of sources. In this paper, we will apply MLE and soft-max human brain information integration mechanisms to cognitive radar sensor network information integration.

IV. HUMAN-INSPIRED SENSE-THROUGH-FOLIAGE TARGET DETECTION

In Figs. 3a and 3b, we plot two collections of UWB radars. Fig. 3a has no target on range, and Fig. 3b has
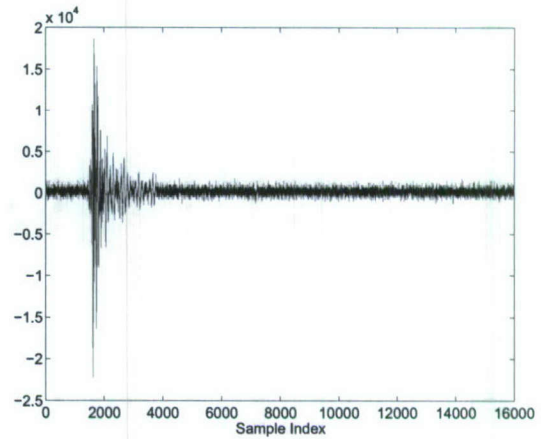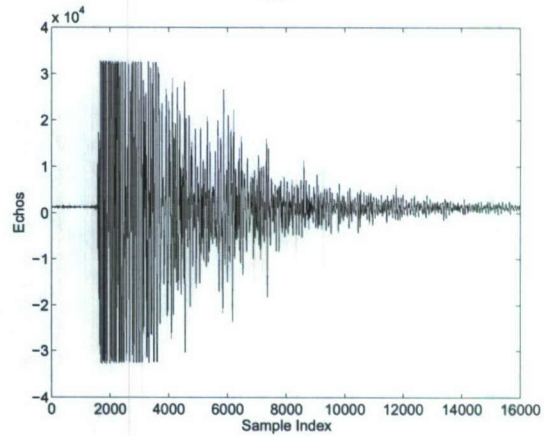
target at samples around 13,900. We plot the echo differences between Figs. 3a and 3b in Fig. 3c. However, it is impossible to identify whether there is any target and where there is target based on Fig. 3c. Since significant pulse-to-pulse variability exists in the echos, this motivate us to explore the spatial and time diversity using Radar Sensor Networks (RSN).

In RSN, the radar sensors are networked together in an ad hoc fashion. They do not rely on a preexisting fixed infrastructure, such as a wireline backbone network or a base station. They are self-organizing entities that are deployed on demand in support of various events surveillance, battlefield, disaster relief, search and rescue, etc. Scalability concern suggests a hierarchical organization of radar sensor networks with the lowest level in the hierarchy being a cluster. As argued in [7] [6] [5] [9], in addition to helping with scalability and robustness, aggregating sensor nodes into clusters has additional benefits:

2

(a)

(b)

(c)

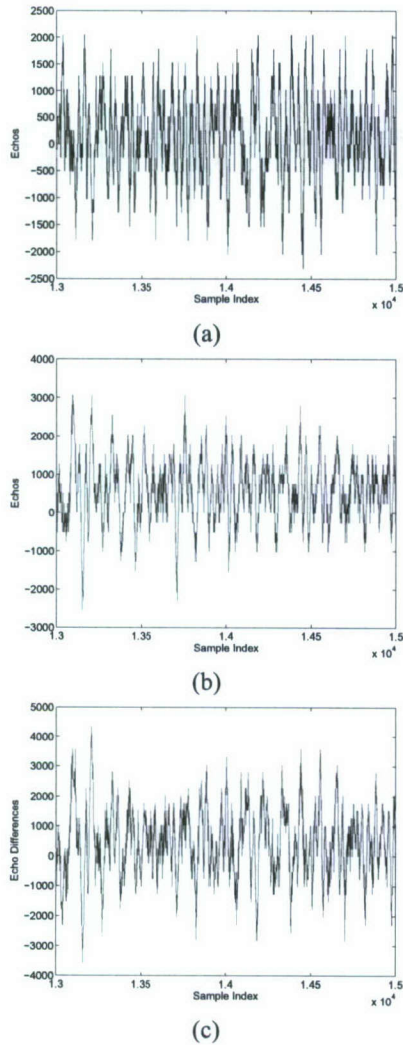Fig. 3. Measurement with poor signal quality and 35 pulses average. (a) Expanded view of traces (no target) from sample 13,001 to 15,000. (b) Expanded view of traces (with target) from samples 13,001 to 15,000. (c) The differences between (a) and (b).

1) conserving radio resources such as bandwidth;
2) promoting spatial code reuse and frequency reuse;
3) simplifying the topology, e.g., when a mobile radar changes its location, it is sufficient for only the nodes in attended clusters to update their topology information;
4) reducing the generation and propagation of routing information; and,
5) concealing the details of global network topology from individual nodes.

In RSN, each radar can provide their pulse parameters such as timing to their clusterhead radar, and the clusterhead radar can combine the echos (RF returns) from the target and clutter. In this paper, we propose a RAKE structure for combining echos, as illustrated by Fig. 4. The integration means time-average for a sample duration T and it's for general case when the echos are not in discrete values. It is quite often assumed that the radar sensor platform will have access to Global Positioning Service (GPS) and Inertial Navigation Unit (INU) timing and navigation data [1]. In this paper, we assume the radar sensors are synchronized in RSN. In Fig. 4, the echo, i.e., RF response by the pulse of each cluster-member sensor, will be combined by the clusterhead using a weighted average, and the weight w_i is determined by the two human-inspired mechanisms.
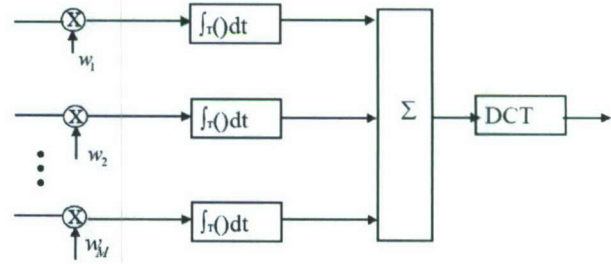
Fig. 4. Echo combining by clusterhead in RSN.

We applied the human-inspired MLE algorithm to combine the sensed echo collection from $M = 30$ UWB radars, and then the combined data are processed using discrete-cosine transform (DCT) to obtain the AC values. Based on our experiences, echo with a target generally has high and nonfluctuating AC values and the AC values can be obtained using DCT. We plot the power of AC values in Figs. 5a and 5b using MLE and DCT algorithms for the two cases (with target and without target) respectively. Observe that in Fig. 5b, the power of AC values (around sample 13,900) where the target is located is non-fluctuating (somehow monotonically increase then decrease). Although some other samples also have very high AC power values, it is very clear that they are quite fluctuating and the power of AC values behaves like random noise because generally the clutter has Gaussian distribution in the frequency domain.

Similarly, we applied the soft-max algorithm ($n = 2$) to combine the sensed echo collection from $M = 30$ UWB radars, and then used DCT to obtain the AC values. We plot the power of AC values in Figs. 5a and 5b using soft-max and DCT algorithms for the two cases (with target and without target) respectively. Observe that in Fig. 6b, the power of AC values (around sample 13,900) where the target is located is non-fluctuating (somehow monotonically increase then decrease).

We made the above observations. However, in real world application, automatic target detection is necessary to ensure that our algorithms could be performed in real time. In Section V, we apply fuzzy logic systems to automatic target detection based on the power of AC values (obtained

3

via MLE-DCT or soft-max-DCT).

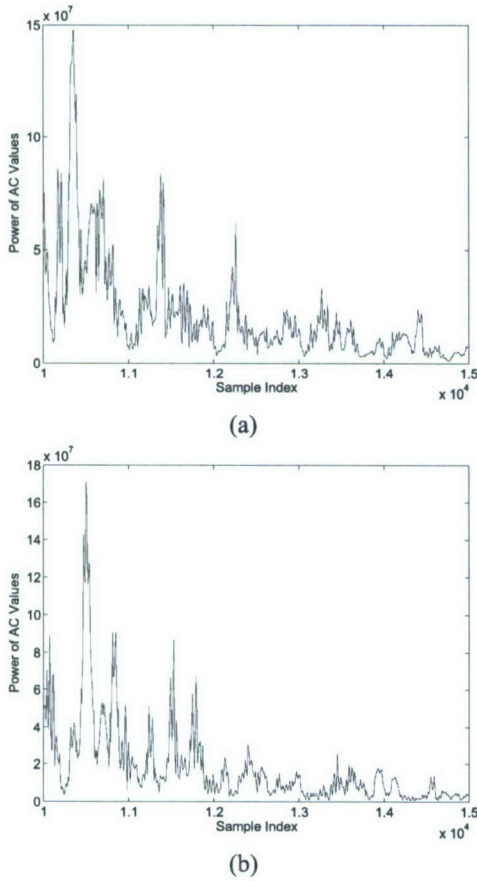Fig. 5. Power of AC values using MLE-based information integration and DCT. (a) No target (b) With target in the field.

Fig. 6. Power of AC values using soft-max based information integration and DCT. (a) No target (b) With target in the field.

We compared our approaches to the scheme proposed in [10]. In [10], 2-D image was created via adding voltages with the appropriate time offset. In Figs. 7a and 7b, we plot the 2-D image created based on the above two data sets (from samples 13,800 to 14,200). The sensed data from 30 radars are averaged first, then plotted in 2-D [10]. However, it's not clear which image shows there is target on range.

V. FUZZY LOGIC SYSTEM FOR AUTOMATIC TARGET DETECTION

A. Overview of Fuzzy Logic Systems

Figure 8 shows the structure of a fuzzy logic system (FLS) [8]. When an input is applied to a FLS, the inference engine computes the output set corresponding to each rule. The defuzzifer then computes a crisp output from these rule output sets. Consider a p-input 1-output FLS, using singleton fuzzification, *center-of-sets* defuzzification [8] and "IF-THEN" rules of the form

$$R^l : \text{IF } x_1 \text{ is } F_1^l \text{ and } x_2 \text{ is } F_2^l \text{ and } \cdots \text{ and } x_p \text{ is } F_p^l,$$
$$\text{THEN } y \text{ is } G^l.$$

Assuming singleton fuzzification, when an input $\mathbf{x}' = \{x_1', \ldots, x_p'\}$ is applied, the degree of firing corresponding to the lth rule is computed as

$$\mu_{F_1^l}(x_1') \star \mu_{F_2^l}(x_2') \star \cdots \star \mu_{F_p^l}(x_p') = \mathcal{T}_{i=1}^p \mu_{F_i^l}(x_i') \quad (2)$$

where $\star$ and $\mathcal{T}$ both indicate the chosen t-norm. There are many kinds of defuzzifiers. In this paper, we focus, for illustrative purposes, on the center-of-sets defuzzifier [8]. It computes a crisp output for the FLS by first computing the centroid, c_{G^l}, of every consequent set G^l, and, then computing a weighted average of these centroids. The weight corresponding to the lth rule consequent centroid is the degree of firing associated with the lth rule, $\mathcal{T}_{i=1}^p \mu_{F_i^l}(x_i')$, so that

$$y_{cos}(\mathbf{x}') = \frac{\sum_{l=1}^M c_{G^l} \mathcal{T}_{i=1}^p \mu_{F_i^l}(x_i')}{\sum_{l=1}^M \mathcal{T}_{i=1}^p \mu_{F_i^l}(x_i')} \quad (3)$$

where M is the number of rules in the FLS. In this paper, we design a FLS for automatic target recognition based on

4

(a)

(b)

Fig. 7. 2-D image created via adding voltages with the appropriate time offset. (a) No target (b) With target in the field.

the AC values obtained using MLE-DCT or soft-max-DCT.

Fig. 8. The structure of a fuzzy logic system.

B. FLS for Automatic Target Detection

Observe that in Figs. 5 and 6, the power of AC values are quite fluctuating and have lots of uncertainties. FLS is well known to handle the uncertain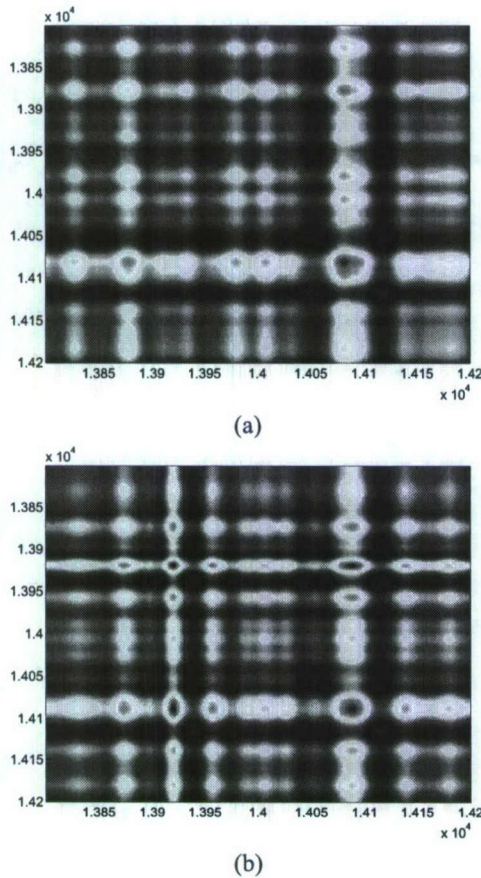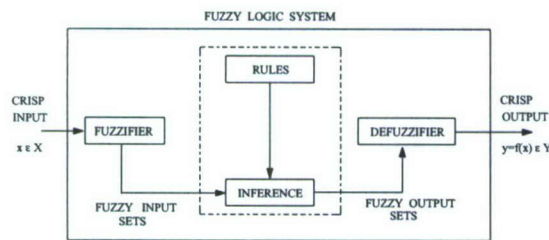ties. For convenience in describing the FLS design for Automatic Target Detection (ATD), we first give the definition of *footprint of uncertainty* of AC power values and *region of interest* in the footprint of uncertainty.

Definition 1 (Footprint of Uncertainty): Uncertainty in the AC power values and time index consists of a bounded region, that we call the *footprint of uncertainty* of AC power values. It is the union of all AC power values.

Definition 2 (Region of Interest (RoI)): An RoI in the footprint of uncertainty is a contour consisting of a large number (greater than 50) of AC power values where AC power values increase then decrease.

Definition 3 (Fluctuating Point in RoI): $P(i)$ is called a *fluctuating point* in the RoI if $P(i-1), P(i), P(i+1)$ are non-monotonically increasing or decreasing.

Our FLS for automatic target detection will classify each ROI (with target or no target) based on two antecedents: *the centroid of the ROI* and *the number of fluctuating points in the ROI*. The linguistic variables used to represent these two antecedents were divided into three levels: *low*, *moderate*, and *high*. The consequent – the possibility that there is a target at this RoI – was divided into 5 levels, *Very Strong, Strong, Medium, Weak, Very Weak*. We used trapezoidal membership functions (MFs) to represent *low*, *high*, *very strong*, and *very weak*; and triangle MFs to represent *moderate, strong, medium*, and *weak*. All inputs to the antecedents are normalized to 0–10.

Based on the fact the AC power value of target is non-fluctuating (somehow monotonically increase then decrease), and the AC power value of clutter behaves like random noise because generally the clutter has Gaussian distribution in the frequency domain, we design a fuzzy logic system using rules such as:

R^l : IF *centroid of a RoI* (x_1) is F_l^1, and *the number of fluctuating points in the ROI* (x_2) is F_l^2, THEN the possibility that there is a target at this RoI (y) is G^l.

where $l = 1, \ldots, 9$. We summarize all the rules in Table I. For every input (x_1, x_2), the output is computed using

$$y(x_1, x_2) = \frac{\sum_{l=1}^{9} \mu_{F_l^1}(x_1)\mu_{F_l^2}(x_2)c_{avg}^l}{\sum_{l=1}^{9} \mu_{F_l^1}(x_1)\mu_{F_l^2}(x_2)} \quad (4)$$

We ran simulations to 1000 collections in the real world sense-through-foliage experiment, and found that our FLS performs very well in the automatic target detection based on the AC power values obtained from MLE-DCT or soft-max-DCT, and achieve probability of detection $p_d = 100\%$ and false alarm rate $p_{fa} = 0$.

VI. CONCLUSIONS

Inspired by human's innate ability to process and integrate information from disparate, network-based sources, we applied human-inspired information integration mechanisms to target detection in UWB radar sensor network. Humans' information integration mechanisms have been modelled using maximum-likelihood estimation (MLE) or soft-max approaches. In this paper, we applied these two algorithms to UWB radar sensor networks target detection.

5

TABLE I

THE RULES FOR TARGET DETECTION. ANTECEDENT 1 IS *centroid of a RoI*, ANTECEDENT 2 IS *the number of fluctuating points in the ROI*, AND CONSEQUENT IS *the possibility that there is a target at this RoI*.

Rule #	Antecedent 1	Antecedent 2	Consequent
1	low	low	medium
2	low	moderate	weak
3	low	high	very weak
4	moderate	low	strong
5	moderate	moderate	medium
6	moderate	high	weak
7	high	low	very strong
8	high	moderate	strong
9	high	high	medium

Discrete-cosine-transform (DCT) was used to process the integrated data from MLE or soft-max. We applied fuzzy logic system (FLS) to automatic target detection based on the AC power values from DCT. Simulation results showed that our MLE-DCT-FLS and soft-max-DCT-FLS approaches performed very well in the radar sensor network target detection, whereas the existing 2-D construction algorithm couldn't work in this study.

REFERENCES

[1] ONR BAA 07-017, "NET-SENTRIC Surveillance," http://www.onr.navy.mil/02/baa/.

[2] D. K. Barton, *Radar System Analysis and Modeling*, Artech House, Boston, MA, 2006.

[3] N. V. S. Graham, "Visual pattern analyzers," pp. xvi, 646, New York, NY, US: Oxford University Press, 1989.

[4] J. M. Hillis, M. O. Ernst, M. S. Banks, and M. S. Landy, "Combining sensory information: Mandatory fusion within, but not between, senses," *Science*, vol. 298, No. 5598, pp. 1627-1630, 2002.

[5] T.-C. Hou and T-J. Tsai, " An access-based clustering protocol for multihop wireless ad hoc networks," *IEEE J. Selected Areas in Communications*, vol. 19, no. 7, pp. 1201-1210, July 2001.

[6] A. Iwata, C. C. Chiang, G. Pei, M. Gerla, and T. W. Chen, " Scalable routing strategies for ad hoc networks," *IEEE J. Selected Areas in Communications*, vol. 17, pp. 1369-1379, 1999.

[7] C. R. Lin and M. Gerla, "Adaptive clustering in mobile wireless networks," *IEEE J. Selected Areas in Communications*, vol. 16, pp. 1265-1275, 1997.

[8] J. M. Mendel, *Uncertain Rule-Based Fuzzy Logic Systems*, Prentice-Hall, Upper Saddle River, NJ, 2001.

[9] C. E. Perkins, "Chapter 4, Cluster-Based Networks," *Ad Hoc Networking*, Edited by C. E. Perkins, pp. 75-138, Addison-Wesley, 2001.

[10] P. Withington , H. Fluhler, and S. Nag , "Enhancing homeland security with advanced UWB sensors," *IEEE Microwave Magazine*, Sept 2003.

6

Outdoor Propagation Channel Modeling in Foliage Environment

Jing Liang and Qilian Liang, *Senior Member, IEEE*

Department of Electrical Engineering

University of Texas at Arlington

E-mail: jliang@wcn.uta.edu, liang@uta.edu

Abstract

In this paper, we study the statistical modeling for outdoor non line-of-sight (NLOS) channel in rich scattering and time-varying foliage environment based on extensive data collected using both narrowband and ultra-wideband (UWB) radars. The multi-path contributions arrive at the receiver are grouped into clusters. The time of arrival of clusters can be modeled as a Poisson arrival process, while within each cluster, subsequent multipath contributions or rays also arrive according to a Poisson process. However, the parameters are quite different along with the frequency. We also observe that the amplitude of channel coefficient at each path can be more accurately characterized by log-logistic distribution (LLD) other than log-normal, Weibull or Rayleigh due to the best goodness-of-fit and smallest root-mean-square (RMS).

Index Terms : Propagation channel, outdoor, NLOS, log-logistic, goodness-of-fit, narrowband, UWB

1 Introduction and Motivation

The area of indoor radio propagation channel measurement and modeling has been intensively investigated [1] [2] [3] because if the characterization of propagation channel is known, efforts can be employed at both transmitters and receivers to overcome the degrading effects and therefore improve the communication performance. As far as military warefare is concerned, lots of applications are for outdoor activities such as sense-through-foliage target detection. It is believed that understanding the characterization of outdoor non line-of-sight (NLOS) channels will assist both target detection

1

as well as commercial wireless communications.

Like indoor environment, the foliage contains a wealth of multiple scattering other than LOS free space. In addition, the movement of leaves, branches and even the tree trunks contribute to the time-variance fading phenomenon. Since the foliage medium can be completely described by its time and space varying feature, one can investigate the channel model based on characterization of the channel impulse response (CIR).

In our investigation, we will apply both narrowband and ultra-wide band (UWB) radar to model the propagation channel, as we believe that foliage is composed of intervening materials that are electromagnetically dispersive, which contributes to the strong frequency dependence of foliage, and thus a narrowband-wideband study would assist with the better understanding of statistic property of the channel. Narrowband signals have been tried at 200, 400 and 600 megahertz respectively, while UWB radar emissions are at a relatively low frequency-typically between 100 MHz and 3 GHz. Each frequency component in a radar signal will sense the foliage clutter in a slightly different manner, therefore provides difference in multipath.

The rest of this paper is organized as follows. In Section 2, we summarize the measurement and collection of the data. In Section 3, we apply CLEAN algorithm to extract CIR for 200MHz, 400MHZ, 600MHz and UWB signals. Section 4 presents the channel model in view of temporal characterization as well as statistic model comparison. We conclude our work in Section 5.

2 Measurement Setup

The foliage penetration measurement effort began in August 2005 and continued through December 2005. Working in August through the fall of 2005, the foliage measured included late summer foliage and fall and early winter foliage. Late summer foliage, because of the limited rainfall, involved foliage with decreased water content. Late fall and winter measurements involved largely defoliated but dense forest, so it's a rich scattering environment. Because of wind or different temperature in dense forest, it's also a time-varying environment.

The radar experiment was constructed on a seven-ton man lift, which had a total lifting capacity of 450 kg. The limit of the lifting capacity was reached during the experiment as essentially the

2

entire measuring apparatus was placed on the lift (as shown in Fig. 1). The principle pieces of equipment secured on the lift are: dual antenna mounting stand; two antennas; 200MHz, 1Kw Amplifier, power supply, pre-amp; 400MHz, 1Kw Amplifier, power supply, pre-amp; 600MHz, 1Kw Amplifier, power supply, pre-amp; Tektronix model 7704 B oscilloscope; rack system; IBM laptop; HP signal Generator; Custom RF switch and power supply and weather shield (small hut). Particularly for UWB signal, a Barth pulse source (Barth Electronics, Inc. model 732 GL) was used. The pulse generator uses a coaxial reed switch to discharge a charge line for a very fast rise time pulse outputs. The model 732 pulse generator provides pulses of less than 50 picoseconds (ps) rise time, with amplitude from 150 V to greater than 2 KV into any load impedance through a 50 ohm coaxial line. The generator is capable of producing pulses with a minimum width of 750 ps and a maximum of 1 microsecond. This output pulse width is determined by charge line length for rectangular pulses, or by capacitors for 1/e decay pulses.

The system was pointing at the specified 250 feet one way distance. For the data we used in this paper, each sample is spaced at 50 picoseconds interval, and 16,000 samples were collected for each collection for a total time duration of 0.8 microseconds. The accomplished data structure is shown in Fig. 2. For each frequency band, 12 positions named '0','2','4','5','6','8','10','12','14','16','18' and '20' have been tested. 35 pulses have been obtained for the transmitted and received signal respectively at each position. 'EMCO' is the brand name of the antenna horn. 'Background' refers to the background data taken along the track with the antenna bore sighted to the targets.

In the foliage-target data, we fired from each of twelve positions along the track. The firing was into the foliage at right angles to the track and these right angle shots are called track data, i.e., 'Track'. At all twelve positions along the track, the azimuth angle of the transmit antenna was changed from plus 10 to - 10 degrees to provide radial measurements, i.e., 'Radial'.

3

3 Channel Impulse Response Based on the Measured Data and CLEAN Algorithm

The average transmitted and received pulses at position 4 for different frequencies have been illustrated from Figs. 3 - 6. The purpose of average is to remove white Gaussian noise. Note that at a different position the result will be slightly different. However, illustration at one position is sufficient enough to describe the characterization.

The complicated multipath and time-varying CIR can be modeled as follows [4]

$$r(t) \approx \sum_n a_n p_n(t - \tau_n) \tag{1}$$

where a_n and τ_n is referred to as the amplitude and delay of the nth propagation path. In order to extract the CIR from our measurement, the CLEAN algorithm have been used. It was initially introduced in [5] to enhance radio astronomical maps of the sky, and has also been employed in narrowband channel modeling [6][7]; also applied in UWB channel characterization problems [4][8].

Our steps involved [8] are:

1. Calculate the autocorrelation of the transmitted signal $R_{ss}(t)$ and the cross-correlation of the transmitted with the received waveform $R_{sy}(t)$.

2. Find the largest correlation peak in $R_{sy}(t)$, record the normalized amplitudes α_k and the relative time delay τ_k of the correlation peak.

3. Subtract $R_{ss}(t)$ scaled by α_k from $R_{sy}(t)$ at the time delay τ_k.

4. If a stopping criterion (a minimum threshold on the peak correlation is not met, go step 2. otherwise stop.)

Given the transmission, reception and the CLEAN processing described above, the obtained CIR are illustrated from Fig. 7 to Fig. 10. Note that we plot the absolute value of the UWB channel for the comparison between the outdoor UWB channel with the indoor S-V model [9] (see Fig. 10). It is shown that

4

1. Both narrowband and UWB channels are made up of multipath components. The time-varying path magnitude implies that fading generally exists, therefore the received pulses are fairly random from one time to another.

2. The UWB channel we obtained looks similar as the CIR in S-V model shown in Fig. 10. However, they are different in the arrival of cluster and subsequent rays as well as envelope decay.

3. In outdoor environment, the largest scattering, i.e., the highest magnitude does not always appear at the first path. This phenomenon is clearly illustrated in Fig. 7 and 10.

4. Channels are frequency dependent. It has been observed that the intervening materials, such as foliage and soil, have dielectric properties that are strongly frequency dependent. This in part explains the difference among those channels. We will further analyze the detail in the following section.

4   Outdoor Channel Modeling

4.1   Temporal Characterization

In the S-V model, the arrival of clusters is modelled as a Poisson arrival process with a rate Λ, while within each cluster, subsequent multipath contributions or rays also arrive according to a Poisson process with a rate λ (see Fig. 12). Observe Fig. 7~10, like in S-V model, multipath contributions arrive at the receiver grouped into clusters and therefore similar methodology used in S-V model studies may be also applied to 200MHz, 400MHz, 600MHz and UWB CIR. The time of arrival of clusters can be modeled as a Poisson arrival process with a rate Λ, while within each cluster, subsequent multipath contributions or rays also arrive according to a Poisson process with a rate λ. We define:

- T_l = the arrival time of the first path of the l-th cluster;

- $\tau_{k,l}$ = the delay of the k-th path within the l-th cluster relative to the first path arrival time T_l;

5

- $\Lambda =$ the cluster arrival rate;

- $\lambda =$ the ray arrival rate, i.e., the arrival rate of the paths within each cluster.

By definition, we have $\tau_{0l} = T_l$. The distributions of the cluster arrival time and the ray arrival time are given by

$$p(T_l|T_{l-1}) = \Lambda \exp\left(-\Lambda(T_l - T_{l-1}), l > 0\right.$$

$$p(\tau_{k,l}|\tau_{(k-1),l}) = \lambda \exp\left(-\lambda(\tau_{k,l} - \tau_{(k-1),l})\right), k > 0 \tag{2}$$

Specifically, we also observed that the Λ and λ are quite different for 200MHz, 400MHz, 600MHz and UWB CIR. We listed observed parameters in Table 1. As for indoor UWB data, we refer [11]. The higher Λ and λ of UWB implies its exceptional range resolution. Lower Λ and λ of outdoor UWB than those of indoor means indoor environment typically have a richer multiple scattering.

4.2 Statistical Distribution of Channel Amplitude

In the S-V model, the average Power Decay Profile (PDP) is characterized by an exponential decay of the clusters and a different exponential decay for the pulses within each cluster. In other words, the amplitude follows rayleigh distribution. In the IEEE UWB indoor channel model [10], the clutter approach was adopted (same as S-V model), but a lognormal distribution was suggested for characterizing the multipath gain amplitude, and an additional log-normal variable was introduced for representing the fluctuations of the total multipath gain. In this Section we propose that log-logistic model that would better characterize the multipath gain amplitude for both outdoor NLOS narrowband and UWB.

4.2.1 Statistic Models

Log-logistic distribution (LLD) [12] is a special case of Burr's type-XII distribution [13] as well as a special case of the kappa distribution proposed by Mielke and Jonson [14]. Lee *et al.* employed the LLD for frequency analysis of multiyear drought durations [15], whereas Shoukri *et al.* employed LLD to analyse extensive Canadian precipitation data [16], and Narda & Malik used LLD to develop a model of root growth and water uptake in wheat [17]. In spite of intensive application in

6

precipitation and stream-flow data, so far the log-logistic distribution (LLD) statistical model has never been applied to foliage channel model to the best our knowledge.

This model is intended to be employed on a basis of higher kurtosis and longer tails, as well as its shape similarity to log-normal and Weibull distributions. PDF for LLD on a basis of different of μ and σ are illustrated in Fig. 13. As we shall see that this model provides the best curve fit compared to lognormal, Weibull and Rayleigh.

Here we use the two-parameter distribution with parameters μ and σ. The PDF for this distribution is given by

$$f(x) = \frac{e^{\frac{lnx-\mu}{\sigma}}}{\sigma x (1 + e^{\frac{lnx-\mu}{\sigma}})^2}, \quad x > 0, \ \sigma > 0 \tag{3}$$

where μ is scale parameter and σ is shape parameter. The mean of the the LLD is

$$E\{x\} = e^{\mu}\Gamma(1+\sigma)\Gamma(1-\sigma) \tag{4}$$

The variance is given by

$$Var\{x\} = e^{2\mu}\{\Gamma(1+2\sigma)\Gamma(1-2\sigma) - [\Gamma(1+\sigma)\Gamma(1-\sigma)]^2\} \tag{5}$$

while the moment of order k is

$$E\{x^k\} = \sigma e^{\mu} B(k\sigma, 1 - k\sigma), \ k < \frac{1}{\sigma} \tag{6}$$

where

$$B(m,n) = \int_0^1 x^{m-1}(1-x)^{n-1}dx \tag{7}$$

Similarly, the log-normal distribution [18] is a two-parameter distribution with parameters μ and σ. The PDF for this distribution is given by

$$f(x) = \frac{1}{x\sigma\sqrt{2\pi}}e^{-\frac{(lnx-\mu)^2}{2\sigma^2}}, \quad x > 0, \sigma > 0 \tag{8}$$

where μ is the scale parameter and σ is the shape parameter.

The Weibull distribution, which is named after Waloddi Weibull, can be made to fit measurements that lie between the Rayleigh and log-normal distribution [19].

7

The Weibull distribution is also a two-parameter distribution with parameters a and b. The PDF for this distribution is given by

$$f(x) = ba^{-b}x^{b-1}e^{-(x/a)^b}, \quad x > 0, a > 0, \ b > 0 \tag{9}$$

where b is the shape parameter and a is the scale parameter.

The Rayleigh distribution, whose real and imaginary components are Gaussian, has the PDF as follows:

$$f(x) = \frac{x}{b^2}e^{-\frac{x^2}{2b^2}}, \quad b > 0 \tag{10}$$

If a and b are the parameters of the Weibull distribution, then the Rayleigh distribution with parameter b is equivalent to the Weibull distribution with parameters $a = \sqrt{2}b$ and $b = 2$.

4.2.2 Maximum Likelihood Estimation

On a basis of CIR cluster amplitude from 12 different positions, we apply Maximum Likelihood Estimation (MLE) approach to estimate the parameters for log-logistic, log-normal, Weibull and Rayleigh models respectively. MLE is often used when the sample data are known and parameters of the underlying probability distribution are to be estimated [20] [21]. It is generalized as follows:

Let $y_1, y_2, \cdots, y_N$ be N independent samples drawn from a random variable $\mathbf{Y}$ with m parameters $\theta_1, \theta_2, \cdots, \theta_m$, where $\theta_i \in \theta$, then the joint PDF of $y_1, y_2, \cdots, y_N$ is

$$L_N(\mathbf{Y}|\theta) = f_{Y|\theta}(y_1|\theta_1, \theta_2, \cdots, \theta_m)f_{Y|\theta}(y_2|\theta_1, \theta_2, \cdots, \theta_m) \cdots f_{Y|\theta}(y_n|\theta_1, \theta_2, \cdots, \theta_m) \tag{11}$$

When expressed as the conditional function of $\mathbf{Y}$ depends on the parameter θ, the likelihood function is

$$L_N(\mathbf{Y}|\theta) = \prod_{k=1}^{N} f_{Y|\theta}(y_k|\theta_1, \theta_2, \cdots, \theta_m) \tag{12}$$

The maximum likelihood estimate of $\theta_1, \theta_2, \cdots, \theta_m$ is the set of values $\hat{\theta}_1, \hat{\theta}_2, \cdots, \hat{\theta}_m$ that maximize the likelihood function $L_N(\mathbf{Y}|\theta)$.

As the logarithmic function is monotonically increasing, maximizing $L_N(\mathbf{Y}|\theta)$ is equivalent to maximizing $\ln(L_N(\mathbf{Y}|\theta))$. Hence, it can be shown that a necessary but not sufficient condition to

8

obtain the ML estimate $\hat{\theta}$ is to solve the likelihood equation

$$\frac{\partial}{\partial \theta} \ln(L_N(\mathbf{Y}|\theta)) = 0 \tag{13}$$

We obtain $\hat{\mu}$ and $\hat{\sigma}$ for log-logistic, $\hat{\mu}$ and $\hat{\sigma}$ for log-normal, $\hat{a}$ and $\hat{b}$ for weibull and $\hat{b}$ for Rayleigh respectively, which are shown in table 2. Note that due to the very small amount of channel sample of 600MHz, its analysis have to be ignored. We also explore the standard deviation (STD) error of each parameter. These descriptions are also shown in table ?? in the form of ε_x, where x denotes different parameter for each model. It is obvious that log-logistic model provides smaller STD errors than those of log-normal.

4.2.3 Goodness-of-fit in curve and RMSE

We may also observe that to what extend does the PDF curve of the statistic model match that of CIR cluster amplitude by root mean square error (RMSE). Let i (i=1, 2, $\cdots$, n) be the sample index of CIR amplitude, c_i is the corresponding PDF value whereas $\hat{c}_i$ is the PDF value of the statistical model with estimated parameters by means of MSE. RMSE is obtained through

$$\text{RMSE} = \sqrt{\frac{1}{n} \sum_{i=1}^{n} (c_i - \hat{c}_i)^2} \tag{14}$$

where n is the amount of sample index. The RMSE for 200MHz, 400Hz and UWB have been listed in Table 3. It demonstrates that LLD turns out to be the model that fit the channel data best.

One may also draw the above conclusion from the Fig. 14, which describes the the goodness-of-fit in curve. The absolute amplitude of clusters have been plotted in terms of histogram. It can be easily seen that Rayleigh model provide the worst goodness-of-fit compared to LLD, log-normal and Weibull, so that exponential PDP of the clusters adopted in S-V model can not be applied in outdoor NLOS environment. Also, Weibull is not a good choice due to the inaccurate kurtosis and high tails. Compare LLD with log-normal, it is obvious that LLD is able to provide shaper kurtosis, shaper slope,and lower tail. In other word, LLD provides better goodness-of-fit than that of log-normal.

Since the above investigations have shown that LLD can better characterize the multipath gain amplitude for outdoor NLOS narrowband and UWB channels than log-normal, we may suggest an

9

additional LLD variable to represent the fluctuations of the total multi-path gain. Moreover, similar to the IEEE UWB model, the phase of each path in outdoor NLOS environment may assumed to be either 0 or π with equal probability.

5 Conclusion

In our investigation, we accomplished following conclusions: 1) Outdoor NLOS channels are frequency dependent as intervening materials have dielectric properties that are strongly frequency dependent. 2) Both narrowband and UWB channels are made up of multipath and time-varying components. 3) In outdoor NLOS environment, the largest scattering, i.e., the highest magnitude does not always appear at the first path. 4) The outdoor UWB channels we obtained are similar in their basic features as indoor models. However, they are different in the arrival of cluster and subsequent rays as well as envelope decay. 5) The amplitude of channel coefficient at each path can be more accurately characterized by log-logistic distribution (LLD) other than log-normal, Weibull or Rayleigh due to the best goodness-of-fit and smallest root-mean-square (RMS).

Acknowledgement

References

[1] H. Hashemi, "The indoor Radio Propagaion Channel", *Proceedings of the IEEE*, vol. 81, pp. 943-968, July 1993.

[2] A. A. M. Saleh and R. A. Valenzuela, "A statistical Model for Indoor Multipath Propagation", *IEEE Journal on selected areas in communications*, vol. SAC-5, pp. 128-137, 1987

10

[3] T. S. Rappaport, "Characterization of UHF multipath radio channels in factory buildings", *IEEE Transactions on Antennas and Propagation*, vol. 37, pp. 1058-1069, Aug. 1989

[4] R. J. -M. Cramer, R. A. Scholtz and M. Z. Win, "Evaluation of an ultra-wide-band propagation channel", *IEEE Transactions on Antennas and Propagation*, vol. 50, pp. 561 - 570, May 2002.

[5] J. A. Högbom, "Aperture Synthesis with a non-regular distribution of interferometer baselines", *Astronomy and Astrophysics Supplement Ser.*, vol. 15, pp. 417-426, 1974.

[6] Q. Spencer, M. Rice, B. Jeffs and M. Jensen, "A Statistical Model for the Angle-of-Arrival in Indoor Multipath Propagation", *IEEE Vehicular Technology Conference*, IEEE 1997, pp. 1415-1419.

[7] G. L. Turin, "Introduction to Spread Spectrum Antimultipath Techniques and their Application to Urban Digital Radio", Proc. IEEE, vol. 68, March 1980, pp. 328-354.

[8] J. H. Reed, *An introduction to Ultra Wideband Communication Systems*, Prentice Hall, 2005.

[9] A. A. Saleh and R. A. Valenzuela, "A statistical model for indoor multipath propagation", *IEEE J. on Selected Areas in Communications*, vol. 5, no.2, pp. 128-137, Feb 1987.

[10] IEEE 802. 15. SG3a, "Channel modeling sub-committee report final," *IEEE P802.15-02/490r1-SG3a*, Feb 2003.

[11] M. -G. Di Benedetto and G. Giancola, *Understanding ultra wideband Radio Fundamentals*, Prentice Hall, 2004.

[12] R. C. Gupta, O. Akman and S. Lvin, "A Study of Log-Logistic Model in Survival Analysis", *Biometrical Journal*, 41, pp. 431-443, 1999

[13] I. W. Burr, "Cumulative frequency functions", *Ann. Math. Statist.*, 13, 215-232, 1942.

[14] P. W. Mielke, and E. S. Johnson, "Three-parameter kappa distribution maximum likelihood estimates and likelihood ratio tests",*Monthly Weather Rev.*, 101, 701-709, 1973.

11

[15] K. S. Lee, J. Sadeghipour and J. A. Dracup, "An approach for frequency analysis of multiyear dought duration", *Wat. Resour. Res.* 22(5), 655-662, 1986.

[16] M. M. Shoukri, I. U. H. Mian, and D. S. Tracy, " Sampling properties of estimators of the log-logistic distribution with application to Canadian precipitation data", *Can. J. Statist.* 16(3), 223-236, 1988.

[17] N. K. Narda and R. K. Malik, "Dynamic model of root growth and water uptake in wheat", *Indian J. Agric. Engng* 3(3&4), 147-155, 1993.

[18] E. Limpert, W. Stahel and M. Abbt, "Log-normal Distributions across the Sciences: Keys and Clues", *BioScience*, 51 (5), pp. 341C352, 2001.

[19] W. Weibull, "A statistical distribution function of wide applicability", J. Appl. Mech.-Trans. ASME 18(3), 293-297, 1951.

[20] Devore, *Probability and Statistics for Engineering and the Sciences*, Monterey, CA: Brooksi-Cole, 1982.

[21] M. Barkat, *Signal deteciton and estimation*, 2nd, London: Artech house, 2005.

12

List of Tables

Table 1: Temporal Parameters for Channel Models

Scenario	$\Lambda(1/ns)$	$\lambda(1/ns)$
200MHz	0.012	0.4
400MHz	0.004	0.128
600MHz	0.002	0.06
Outdoor UWB	0.04	0.8
Indoor UWB Extreme NLOS	0.0667	2.1

Table 2: Estimated Parameters for Statistic Model

PDF	Log-Logistic	Log-normal	Weibull	Rayleigh
200MHz	$\hat{\mu} = -3.79907$ $\hat{\sigma} = 0.43948$ $\varepsilon_\mu = 0.0517626$ $\varepsilon_\sigma = 0.0250518$	$\hat{\mu} = -3.69473$ $\hat{\sigma} = 0.811659$ $\varepsilon_\mu = 0.0550099$ $\varepsilon_\sigma = 0.0390963$	$\hat{a} = 0.0388139$ $\hat{b} = 1.00543$ $\varepsilon_a = 0.0027934$ $\varepsilon_b = 0.00456447$	$\hat{b}=0.0474046$
400MHz	$\hat{\mu} = -3.75666$ $\hat{\sigma} = 0.482505$ $\varepsilon_\mu = 0.071783$ $\varepsilon_\sigma = 0.035901$	$\hat{\mu} = -3.61265$ $\hat{\sigma} = 0.917049$ $\varepsilon_\mu = 0.0795182$ $\varepsilon_\sigma = 0.0565477$	$\hat{a} = 0.0447926$ $\hat{b} = 0.903163$ $\varepsilon_a = 0.00458706$ $\varepsilon_b = 0.0536079$	$\hat{b}=0.0609159$
Outdoor UWB	$\hat{\mu} = -3.30616$ $\hat{\sigma} = 0.590192$ $\varepsilon_\mu = 0.202988$ $\varepsilon_\sigma = 0.101636$	$\hat{\mu} = -3.13344$ $\hat{\sigma} = 1.12623$ $\varepsilon_\mu = 0.225245$ $\varepsilon_\sigma = 0.164277$	$\hat{a} = 0.080002$ $\hat{b} = 0.765597$ $\varepsilon_a = 0.0222858$ $\varepsilon_b = 0.106023$	$\hat{b}=0.141188$

Table 3: root mean square error (RMSE) comparison between Statistic Models

PDF	Log-Logistic	Log-normal	Weibull	Rayleigh
200MHz	5.7016	6.2850	8.8810	9.7562
400MHz	5.9023	6.5635	9.7056	10.3359
UWB	2.1867	2.4756	3.0136	4.8975

13

List of Figures

Figure 1: This figure shows the lift with the experiment. The antennas are at the far end of the lift from the viewer under the roof that was built to shield the equipment from the elements. This picture was taken in September with the foliage largely still present. The cables coming from the lift are a ground cable to an earth ground and one of 4 tethers used in windy conditions.
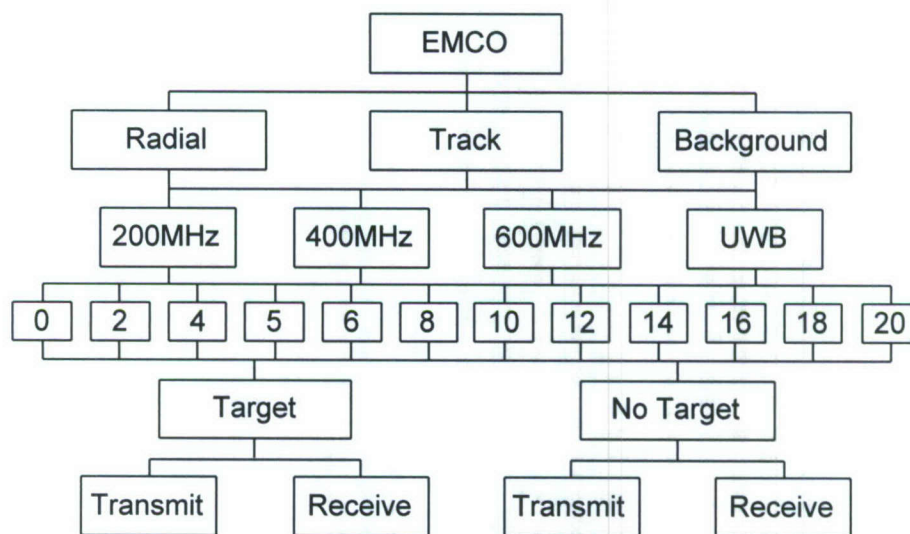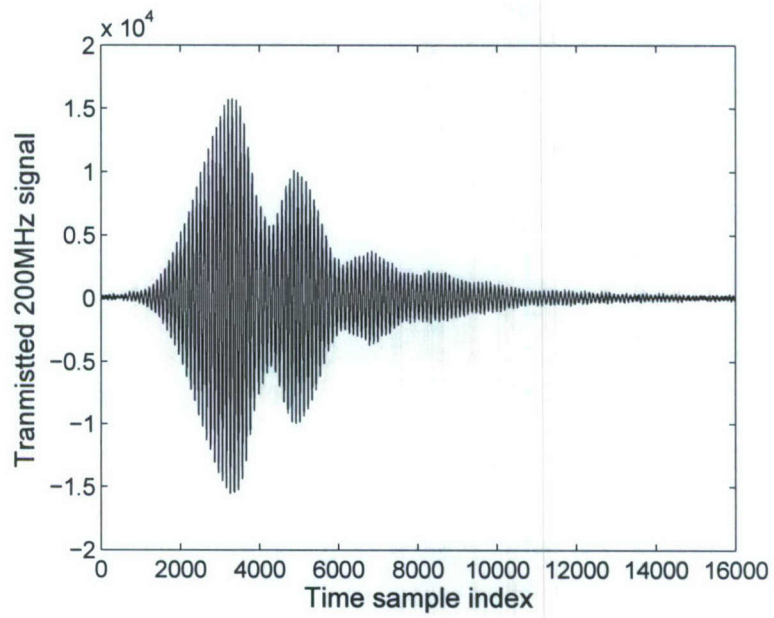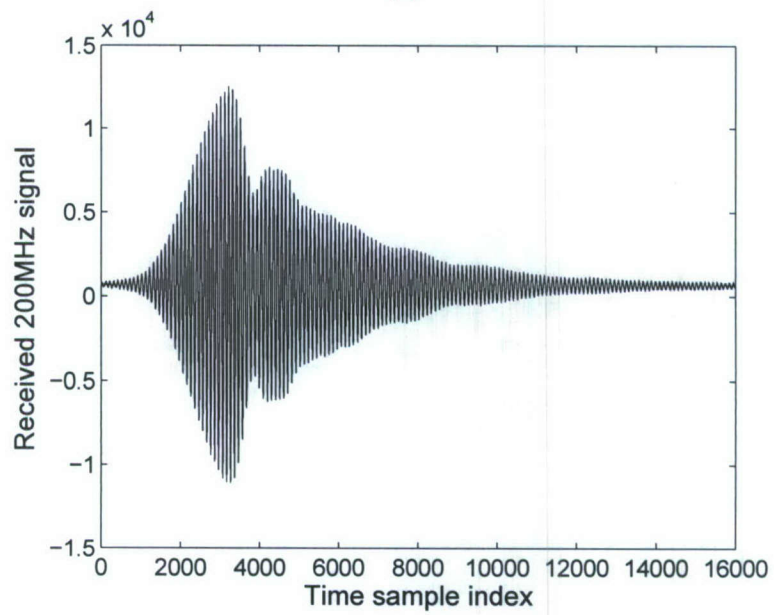
Figure 2: Data file structure

15

Figure 3: Measurement of 200MHz and 35 pulses average : (a) transmitted pulse (b) received echoes

16
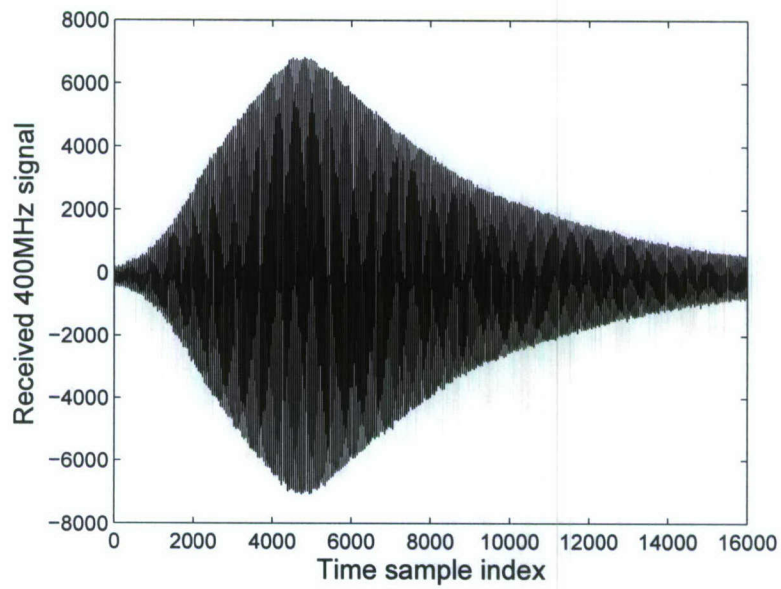
Figure 4: Measurement of 400MHz and 35 pulses average: (a) transmitted pulse (b) received echoes

17
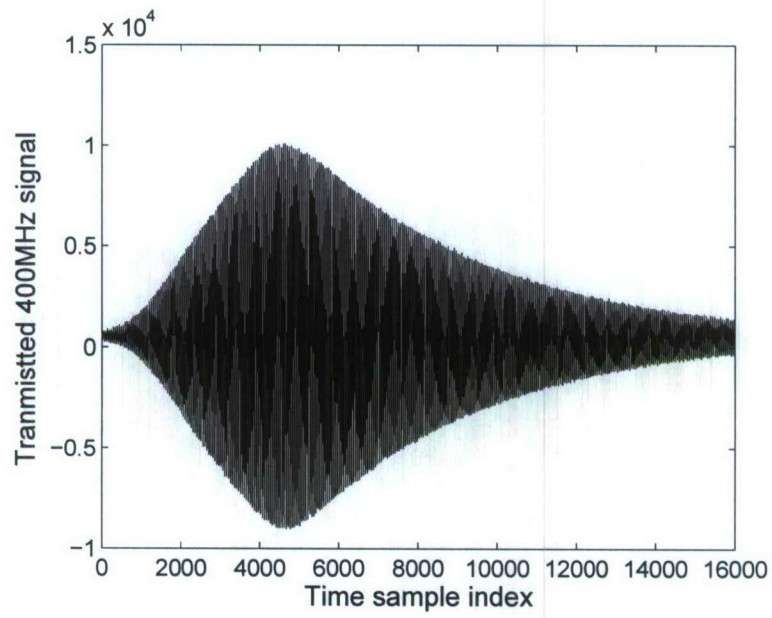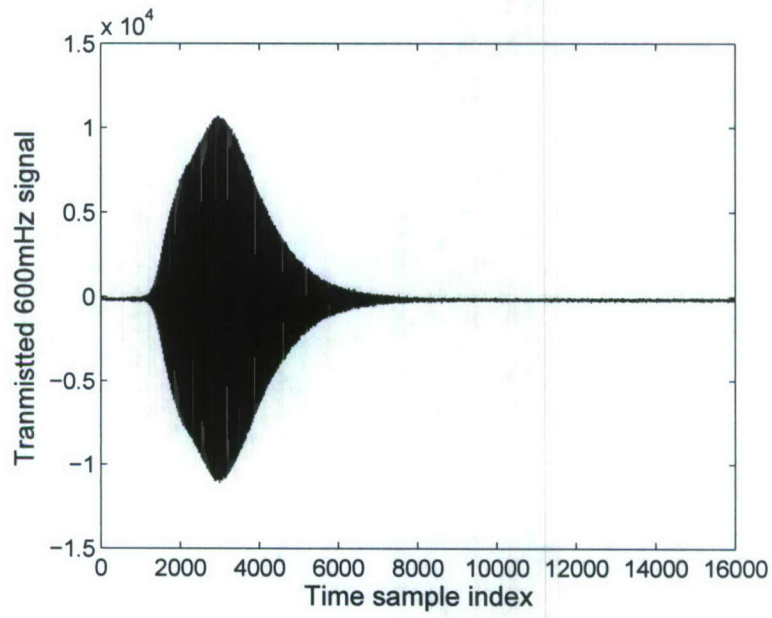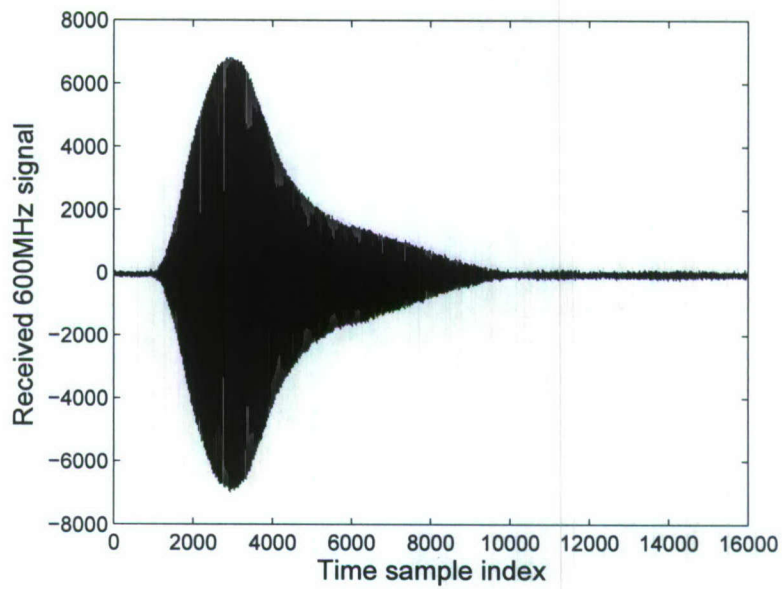
Figure 5: Measurement of 600MHz and 35 pulses average: (a) transmitted pulse (b) received echoes

18
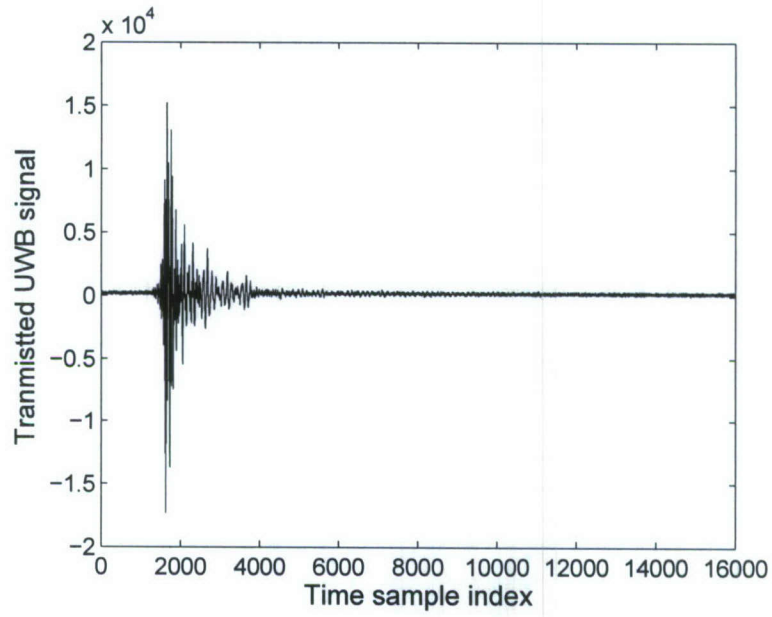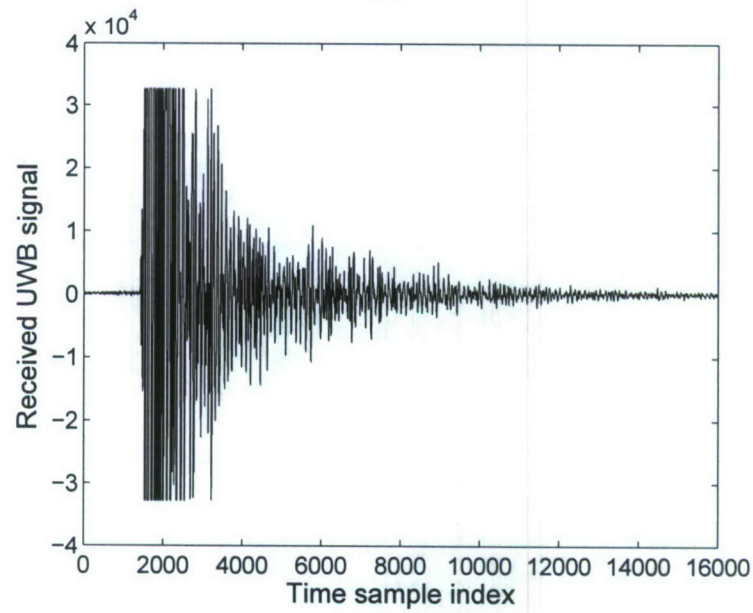
Figure 6: Measurement of UWB and 35 pulses average: (a)transmitted pulse (b) received echoes

19
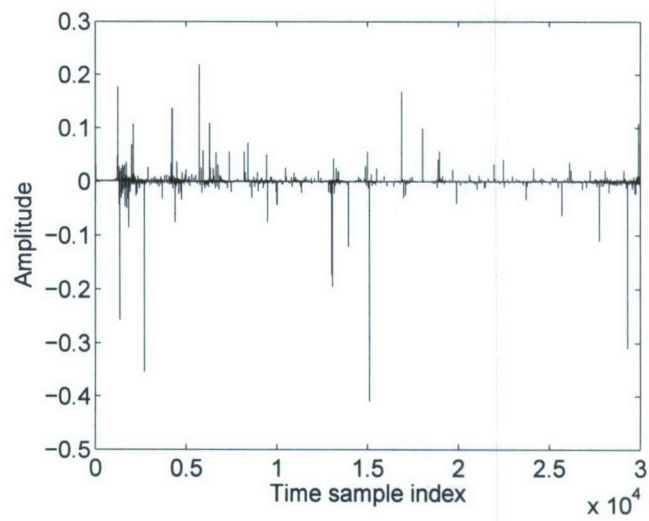
Figure 7: 200MHz Channel
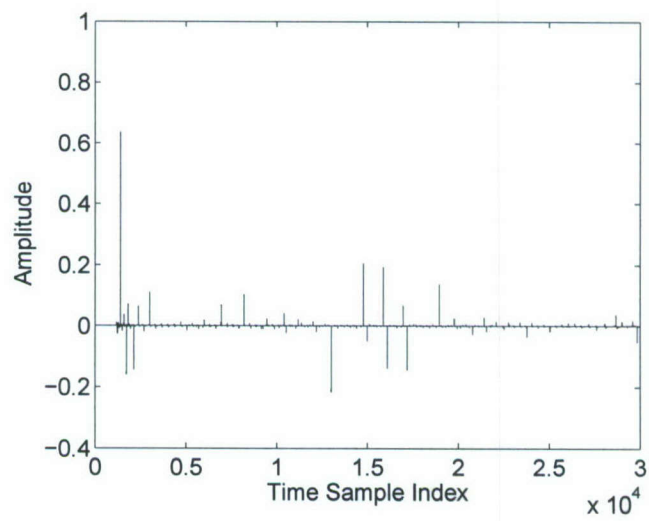
Figure 8: 400MHz Channel

20
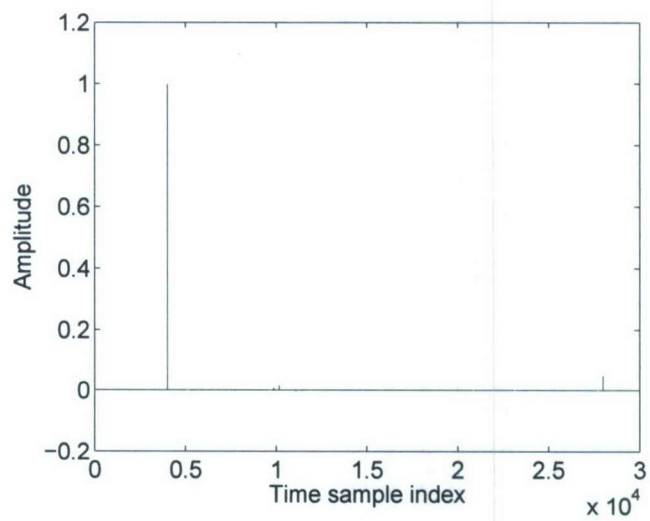
Figure 9: 600MHz Channel
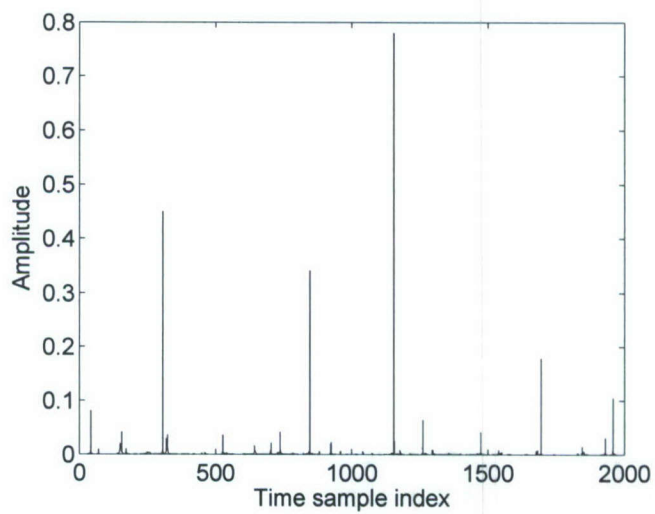
Figure 10: UWB Channel

21
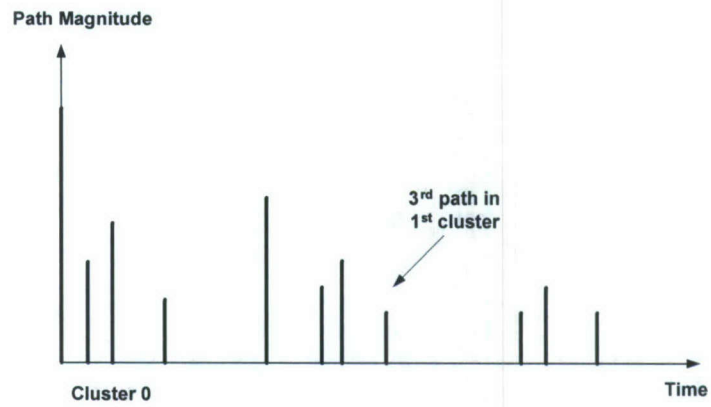
Figure 11: An illustration of the channel impulse in S-V model.
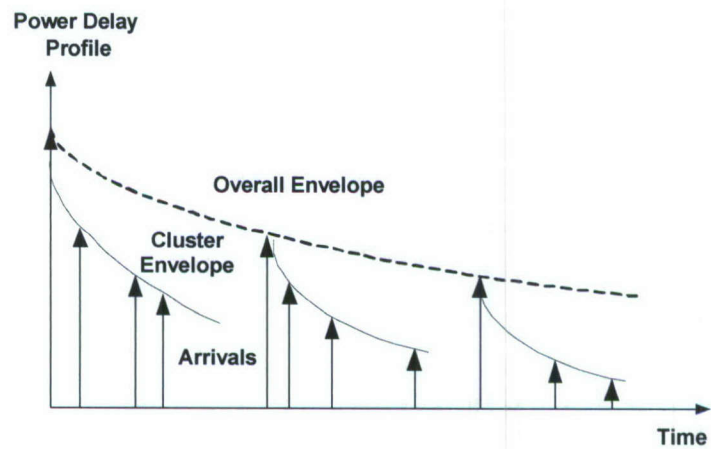
Figure 12: An illustration of the double exponential decay of the mean cluster power and the ray power within clusters in S-V model.

22
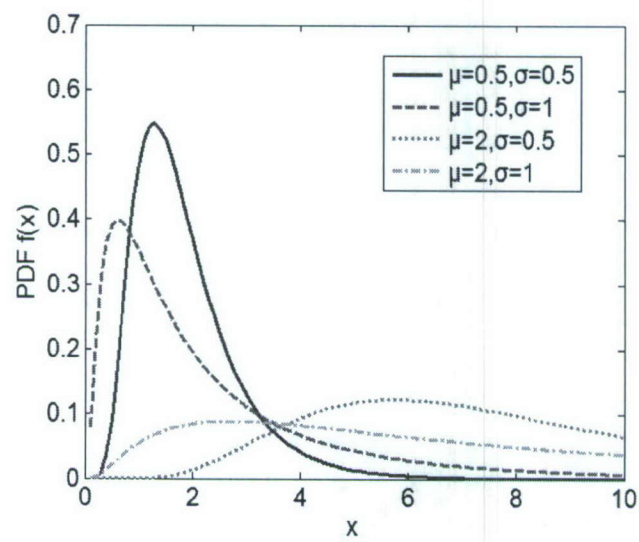
Figure 13: An illustration of log-logistic PDF.

23
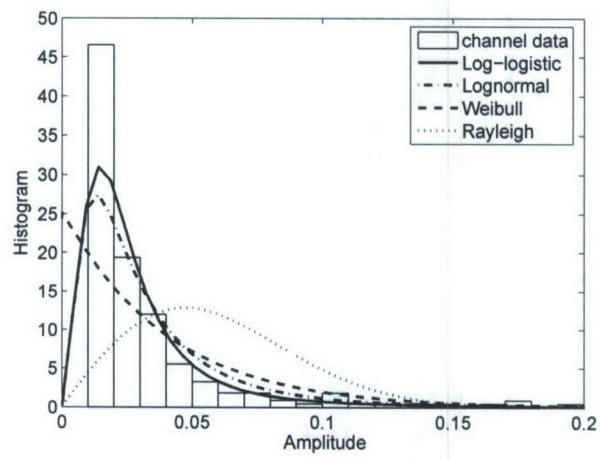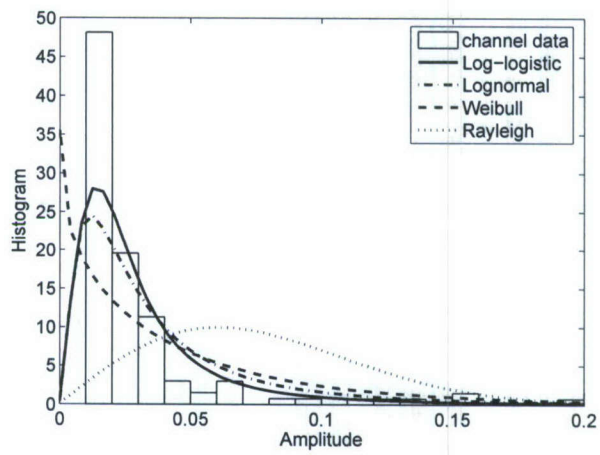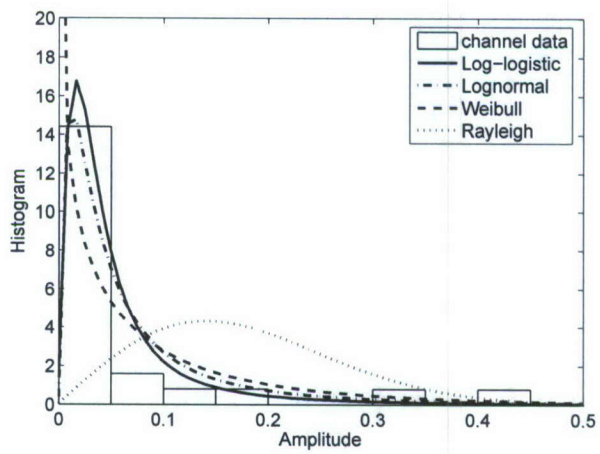
Figure 14: Goodness-of-fit (a)200MHz (b)400MHz (c)UWB

24

Outdoor Propagation Channel Modeling in Foliage Environment

Jing Liang and Qilian Liang
Department of Electrical Engineering
University of Texas at Arlington
E-mail: jliang@wcn.uta.edu, liang@uta.edu

Abstract— In this paper, we study the statistical modeling for outdoor non line-of-sight (NLOS) channels in rich scattering and time-varying foliage environment based on extensive data collected by both narrowband and ultra-wideband (UWB) radars. The multi-path contributions arrive at the receiver are grouped into clusters. The time of arrival of clusters can be modeled as a Poisson arrival process, while within each cluster, subsequent multipath contributions or rays also arrive according to a Poisson process. However, the parameters are quite different along with the frequency. We also observe that the amplitude of channel coefficient at each path can be more accurately characterized as log-logistic distribution (LLD) other than log-normal, Weibull or Rayleigh due to the best goodness-of-fit and smallest root-mean-square (RMS).

I. Introduction

The indoor radio propagation channel measurement and modeling has been intensively investigated [1]-[3]. If the characterization of propagation channel is known, efforts can be employed at both transmitters and receivers to overcome the channel effects and therefore improve the communication performance. As far as military warefare is concerned, lots of applications are for outdoor activities such as sense-through-foliage target detection. It is believed that understanding the characterization of outdoor non line-of-sight (NLOS) channels will assist both target detection as well as commercial wireless communications.

Like indoor environment, the foliage contains a wealth of multiple scattering other than LOS free space. In addition, the movement of leaves, branches and even the tree trunks contribute to the time-variance fading phenomenon. Since the foliage medium can be completely described by its time and space varying feature, one can investigate the channel model based on characterization of the channel impulse response (CIR).

In our investigation, we will apply both narrowband and ultra-wide band (UWB) radars to model the propagation channels, as we believe that foliage is composed of intervening materials that are electromagnetically dispersive, which contributes to the strong frequency dependence of foliage, and thus a narrowband-wideband study would assist with the better understanding of statistic property of the channel. Narrowband signals have been tried at 200, 400 and 600 megahertz respectively, while UWB radar emissions are at a relatively low frequency-typically between 100 MHz and 3 GHz. Each frequency component in a radar signal will sense the foliage clutter in a slightly different manner, therefore provides differences in multipath.

The rest of this paper is organized as follows. In Section II, we summarize the measurement and collection of the data. In Section III, we apply CLEAN algorithm to extract CIR for 200MHz, 400MHZ, 600MHz and UWB signals. Section IV presents the channel model in view of temporal characterization as well as statistic model comparison. We conclude our work in Section V.

II. Measurement Setup

The foliage penetration measurement effort began in August 2005 and continued through December 2005. Working in August through the fall of 2005, the foliage measured included late summer foliage and fall and early winter foliage. Late summer foliage, due to the limited rainfall, involved foliage with decreased water content. Late fall and winter measurements involved largely defoliated but dense forest, so it's a rich scattering environment. Because of wind or different temperature in dense forest, it's also a time-varying environment.

The radar experiment was constructed on a seven-ton man lift, which had a total lifting capacity of 450 kg. The limit of the lifting capacity was reached during the experiment as essentially the entire measuring apparatus was placed on the lift (as shown in Fig. 1). The principle pieces of equipment secured on the lift are: dual antenna mounting stand; two antennas; 200MHz, 1Kw Amplifier, power supply, pre-amp; 400MHz, 1Kw Amplifier, power supply, pre-amp; 600MHz, 1Kw Amplifier, power supply, pre-amp; Tektronix model 7704 B oscilloscope; rack system; IBM laptop; HP signal Generator; Custom RF switch and power supply and weather shield (small hut). Particularly for UWB signal, a Barth pulse source (Barth Electronics, Inc. model 732 GL) was used. The pulse generator uses a coaxial reed switch to discharge a charge line for a very fast rise time pulse outputs. The model 732 pulse generator provides pulses of less than 50 picoseconds (ps) rise time, with amplitude from 150 V to greater than 2 KV into any load impedance through a 50 ohm coaxial line. The generator is capable of producing pulses with a minimum width of 750 ps and a maximum of 1 microsecond. This output pulse width is determined by charge line length for rectangular pulses, or by capacitors for 1/e decay pulses.

The system was pointing at the specified 250 feet distance. For the data we used in this paper, each sample is
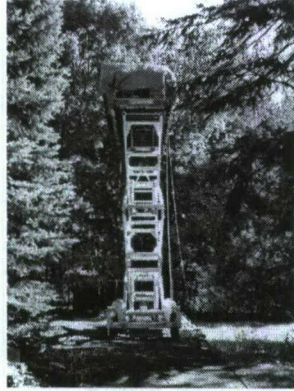
Fig. 1. This figure shows the lift with the experiment. The antennas are at the far end of the lift from the viewer under the roof that was built to shield the equipment from the elements. This picture was taken in September with the foliage largely still present. The cables coming from the lift are a ground cable to an earth ground and one of 4 tethers used in windy conditions.

spaced at 50 picoseconds interval, and 16,000 samples were collected for each collection for a total time duration of 0.8 microseconds. The accomplished data structure is shown in Fig. 2. For each frequency band, 12 positions named '0','2','4','5','6','8','10','12','14','16','18' and '20' have been tested. 35 pulses have been obtained for the transmitted and received signal respectively at each position. 'EMCO' is the brand name of the antenna horn. 'Background' refers to the background data taken along the track with the antenna bore sighted to the targets.
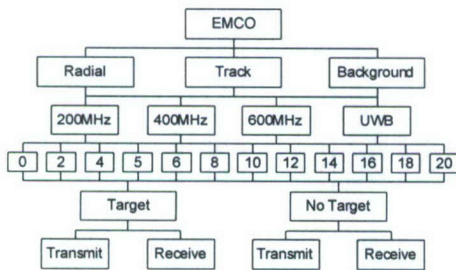
Fig. 2. Data file structure

In the foliage-target data, we fired from each of twelve positions along the track. The firing was into the foliage at right angles to the track and these right angle shots are called track data, i.e., 'Track'. At all twelve positions along the track, the azimuth angle of the transmit antenna was changed from plus 10 to - 10 degrees to provide radial measurements, i.e., 'Radial'.

III. CHANNEL IMPULSE RESPONSE BASED ON THE MEASURED DATA AND CLEAN ALGORITHM

The average transmitted and received pulses at position 4 for different frequencies have been illustrated from Figs. 3 - 6. The purpose of average is to remove white Gaussian noise. Note

that at a different position the result will be slightly different. However, illustration at one position is sufficient enough to describe the characterization.

(a)

(b)
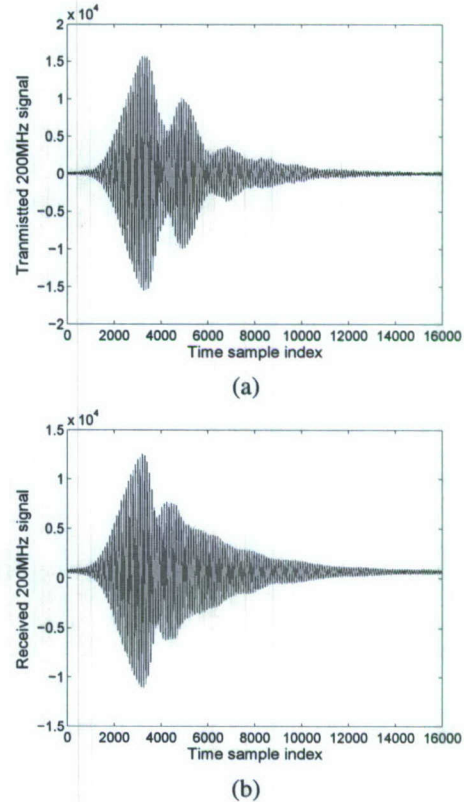
Fig. 3. Measurement of 200MHz and 35 pulses average : (a) transmitted pulse (b) received echoes

The complicated multipath and time-varying CIR can be modeled as follows [4]

$$r(t) \approx \sum_n a_n p_n(t - \tau_n) \qquad (1)$$

where a_n and τ_n is referred to as the amplitude and delay of the nth propagation path. In order to extract the CIR from our measurement, the CLEAN algorithm has been used. It was initially introduced in [5] to enhance radio astronomical maps of the sky, and has also been employed in narrowband channel modeling [6][7]and UWB channel characterization problems [4][8].

Our steps involved [8] are:

1) Calculate the autocorrelation of the transmitted signal $R_{ss}(t)$ and the cross-correlation of the transmitted with the received waveform $R_{sy}(t)$.
2) Find the largest correlation peak in $R_{sy}(t)$, record the normalized amplitudes α_k and the relative time delay τ_k of the correlation peak.
3) Subtract $R_{ss}(t)$ scaled by α_k from $R_{sy}(t)$ at the time delay τ_k.
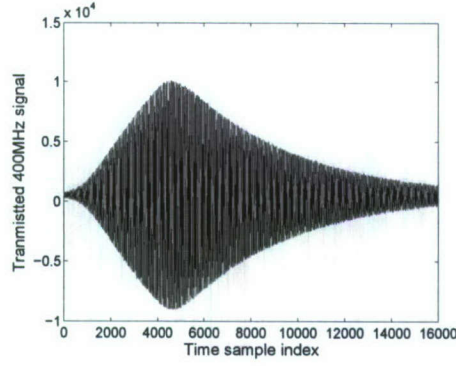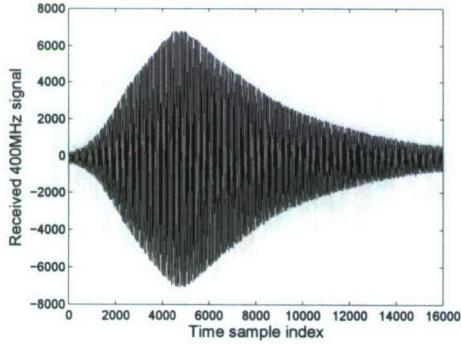
Fig. 4.   Measurement of 400MHz and 35 pulses average: (a) transmitted pulse (b) received echoes
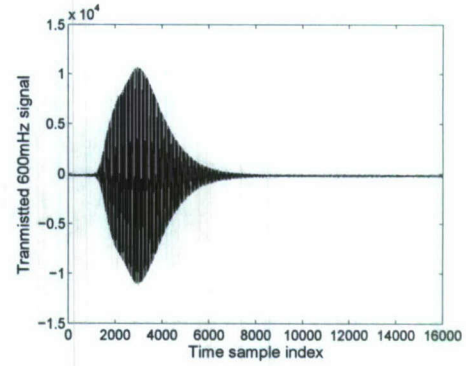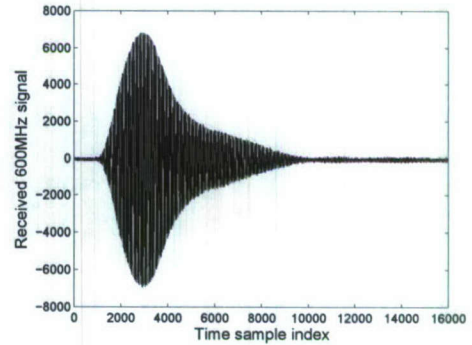
Fig. 5.   Measurement of 600MHz and 35 pulses average: (a) transmitted pulse (b) received echoes

4) If a stopping criterion (a minimum threshold) on the peak correlation is not met, go step 2. otherwise stop.

Given the transmission, reception and the CLEAN processing described above, the obtained CIR are illustrated from Fig. 7 to Fig. 10. Note that we plot the absolute value of the UWB channel for the comparison between the outdoor UWB channel with the indoor S-V model [9] (see Fig. 11). It is shown that

1) Both narrowband and UWB channels are made up of multipath components. The time-varying path magnitude implies that fading generally exists, therefore the received pulses are fairly random from one time to another.

2) The UWB channel we obtained looks similar as the CIR in S-V model shown in Fig. 11. However, they are different in the arrival of cluster, subsequent rays and envelope decay.

3) In outdoor environment, the largest scattering, i.e., the highest magnitude does not always appear at the first path. This phenomenon is clearly illustrated in Fig. 7 and 10.

4) Channels are frequency dependent. It has been observed that the intervening materials, such as foliage and soil, have dielectric properties that are strongly frequency dependent. This in part explains the difference among those channels. We will further analyze the detail in the following section.

IV. OUTDOOR CHANNEL MODELING

A. Temporal Characterization

In the S-V model, the arrival of clusters is modelled as a Poisson arrival process with a rate Λ, while within each cluster, subsequent multipath contributions or rays also arrive according to a Poisson process with a rate λ (see Fig. 12). Observe Fig. 7~10, like in S-V model, multipath contributions arrive at the receiver grouped into clusters and therefore similar methodology used in S-V model studies may be also applied to 200MHz, 400MHz, 600MHz and UWB CIR. The time of arrival of clusters can be modeled as a Poisson arrival process with a rate Λ, while within each cluster, subsequent multipath contributions or rays also arrive according to a Poisson process with a rate λ.

We define:

- T_l = the arrival time of the first path of the l-th cluster;
- $\tau_{k,l}$ = the delay of the k-th path within the l-th cluster relative to the first path arrival time T_l;
- Λ = the cluster arrival rate;
- λ = the ray arrival rate, i.e., the arrival rate of the paths within each cluster.

By definition, we have $\tau_{0l} = T_l$. The distributions of the

(a)

(b)

Fig. 6. Measurement of UWB and 35 pulses average: (a)transmitted pulse (b) received echoes

Fig. 7. 200MHz Channel

Fig. 8. 400MHz Channel

TABLE I

TEMPORAL PARAMETERS FOR CHANNEL MODELS

Scenario	$\Lambda(1/ns)$	$\lambda(1/ns)$
200MHz	0.012	0.4
400MHz	0.004	0.128
600MHz	0.002	0.06
Outdoor UWB	0.04	0.8
Indoor UWB Extreme NLOS	0.0667	2.1

cluster arrival time and the ray arrival time are given by

$$p(T_l|T_{l-1}) = \Lambda \exp\left(-\Lambda(T_l - T_{l-1}), l > 0\right.$$
$$p(\tau_{k,l}|\tau_{(k-1),l}) = \lambda \exp\left(-\lambda(\tau_{k,l} - \tau_{(k-1),l})\right), k > 0 \quad (2)$$

Specifically, we also observed that the Λ and λ are quite different for 200MHz, 400MHz, 600MHz and UWB CIR. We listed observed parameters in Table I. As for indoor UWB data, we refer [11]. The higher Λ and λ of UWB implies its exceptional range resolution. Lower Λ and λ of outdoor UWB than those of indoor means outdoor environment typically more sparse multiple scattering than that of indoor.

B. Statistical Distribution of Channel Amplitude

In the S-V model, the average Power Decay Profile (PDP) is characterized by an exponential decay of the clusters and a different exponential decay for the pulses within each cluster.

In other words, the amplitude follows rayleigh distribution. In the IEEE UWB indoor channel model [10], the clutter approach was adopted (same as S-V model), but a log-normal distribution was suggested for characterizing the multipath gain amplitude, and an additional log-normal variable was introduced for representing the fluctuations of the total multipath gain. In this Section we propose that log-logistic model may better characterize amplitude of the multipath for both outdoor NLOS narrowband and UWB signals.

1) Statistic Models: Log-logistic distribution (LLD) [12] is a special case of Burr's type-XII distribution [13] as well as a special case of the kappa distribution proposed by Mielke and Jonson [14]. Lee et al. employed the LLD for frequency analysis of multiyear drought durations [15], whereas Shoukri et al. employed LLD to analyse extensive Canadian precipitation data [16], and Narda & Malik used LLD to develop a model of root growth and water uptake in wheat [17]. In spite of intensive application in precipitation and stream-flow data, so far LLD statistical model has never been applied to foliage channel model to the best our knowledge.

This model is intended to be employed on a basis of higher kurtosis and longer tails, as well as its shape similarity to log-normal and Weibull distributions. PDF for LLD on a basis of different of μ and σ are illustrated in Fig. 13. As we shall
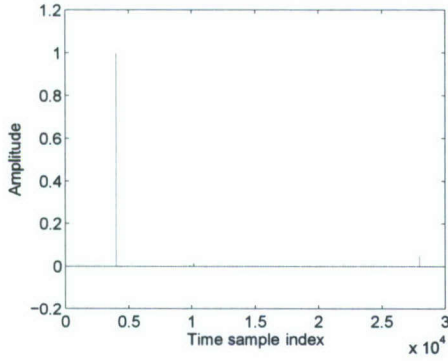
Fig. 9.   600MHz Channel
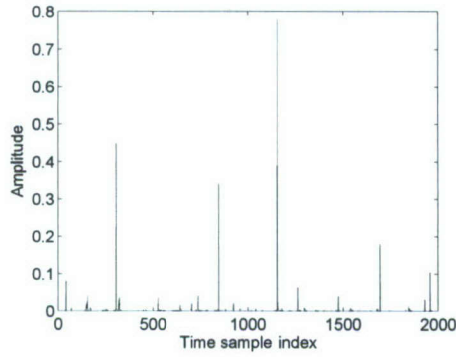
Fig. 10.   UWB Channel

see that this model provides the best curve fit compared to log-normal, Weibull and Rayleigh.

Here we use the two-parameter distribution with parameters μ and σ. The PDF for this distribution is given by

$$f(x) = \frac{e^{\frac{\ln x - \mu}{\sigma}}}{\sigma x (1 + e^{\frac{\ln x - \mu}{\sigma}})^2}, \quad x > 0, \ \sigma > 0 \tag{3}$$

where μ is scale parameter and σ is shape parameter. The mean of the the LLD is

$$E\{x\} = e^\mu \Gamma(1 + \sigma) \Gamma(1 - \sigma) \tag{4}$$
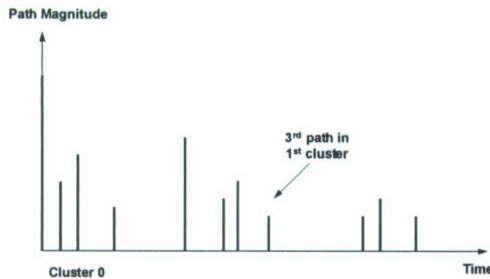
Fig. 11.   An illustration of the channel impulse in S-V model.
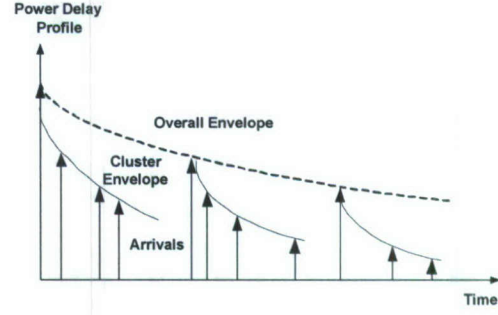
Fig. 12.   An illustration of the double exponential decay of the mean cluster power and the ray power within clusters in S-V model.
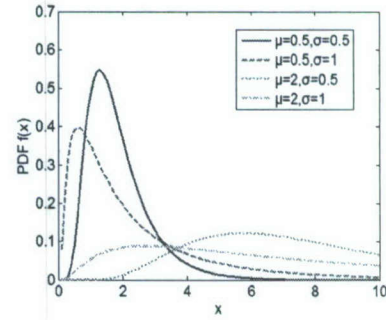
Fig. 13.   An illustration of log-logistic PDF.

The variance is given by

$$Var\{x\} = e^{2\mu}\{\Gamma(1 + 2\sigma)\Gamma(1 - 2\sigma) - [\Gamma(1 + \sigma)\Gamma(1 - \sigma)]^2\} \tag{5}$$

while the moment of order k is

$$E\{x^k\} = \sigma e^\mu B(k\sigma, 1 - k\sigma), \ k < \frac{1}{\sigma} \tag{6}$$

where

$$B(m, n) = \int_0^1 x^{m-1}(1 - x)^{n-1} dx \tag{7}$$

Similarly, the log-normal distribution [18] is a two-parameter distribution with parameters μ and σ. The PDF for this distribution is given by

$$f(x) = \frac{1}{x\sigma\sqrt{2\pi}} e^{-\frac{(\ln x - \mu)^2}{2\sigma^2}}, \quad x > 0, \sigma > 0 \tag{8}$$

where μ is the scale parameter and σ is the shape parameter.

The Weibull distribution can be made to fit measurements that lie between the Rayleigh and log-normal distribution [19].

The Weibull distribution is also a two-parameter distribution with parameters a and b. The PDF for this distribution is given by

$$f(x) = ba^{-b}x^{b-1}e^{-(x/a)^b}, \quad x > 0, a > 0, \ b > 0 \tag{9}$$

where b is the shape parameter and a is the scale parameter.

The Rayleigh distribution, whose real and imaginary components are Gaussian, has the PDF as follows:

$$f(x) = \frac{x}{b^2} e^{-\frac{x^2}{2b^2}}, \quad b > 0 \tag{10}$$

2) Maximum Likelihood Estimation: On a basis of CIR cluster amplitude from 12 different positions, we apply Maximum Likelihood Estimation (MLE) approach to estimate the parameters for log-logistic, log-normal, Weibull and Rayleigh models respectively. MLE is often used when the sample data are known and parameters of the underlying probability distribution are to be estimated [20] [21]. It is generalized as follows:

Let $y_1, y_2, \cdots, y_N$ be N independent samples drawn from a random variable $\mathbf{Y}$ with m parameters $\theta_1, \theta_2, \cdots, \theta_m$, where $\theta_i \in \theta$, then the joint PDF of $y_1, y_2, \cdots, y_N$ is

$$L_N(\mathbf{Y}|\theta) = f_{Y|\theta}(y_1|\theta_1, \theta_2, \cdots, \theta_m) \cdots f_{Y|\theta}(y_n|\theta_1, \theta_2, \cdots, \theta_m) \tag{11}$$

When expressed as the conditional function of $\mathbf{Y}$ depends on the parameter θ, the likelihood function is

$$L_N(\mathbf{Y}|\theta) = \prod_{k=1}^{N} f_{Y|\theta}(y_k|\theta_1, \theta_2, \cdots, \theta_m) \tag{12}$$

The maximum likelihood estimate of $\theta_1, \theta_2, \cdots, \theta_m$ is the set of values $\hat{\theta}_1, \hat{\theta}_2, \cdots, \hat{\theta}_m$ that maximize the likelihood function $L_N(\mathbf{Y}|\theta)$.

As the logarithmic function is monotonically increasing, maximizing $L_N(\mathbf{Y}|\theta)$ is equivalent to maximizing $\ln(L_N(\mathbf{Y}|\theta))$. Hence, it can be shown that a necessary but not sufficient condition to obtain the ML estimate $\hat{\theta}$ is to solve the likelihood equation

$$\frac{\partial}{\partial \theta} \ln(L_N(\mathbf{Y}|\theta)) = 0 \tag{13}$$

We obtain $\hat{\mu}$ and $\hat{\sigma}$ for log-logistic, $\hat{\mu}$ and $\hat{\sigma}$ for log-normal, $\hat{a}$ and $\hat{b}$ for weibull and $\hat{b}$ for Rayleigh respectively, which are shown in table II. Note that due to the very small amount of channel sample of 600MHz, its analysis have to be ignored. We also explore the standard deviation (STD) error of each parameter. These descriptions are also shown in table II in the form of ε_x, where x denotes different parameter for each model. It is obvious that log-logistic model provides smaller STD errors than those of log-normal.

3) Goodness-of-fit in curve and RMSE: We may also observe that to what extend does the PDF curve of the statistic model match that of CIR cluster amplitude by root mean square error (RMSE). Let i (i=1, 2, $\cdots$, n) be the sample index of CIR amplitude, c_i is the corresponding PDF value whereas $\hat{c}_i$ is the PDF value of the statistical model with estimated parameters by means of MSE. RMSE is obtained through

$$\text{RMSE} = \sqrt{\frac{1}{n} \sum_{i=1}^{n} (c_i - \hat{c}_i)^2} \tag{14}$$

where n is the amount of sample index. The RMSE for 200MHz, 400Hz and UWB have been listed in Table III. It

TABLE II
ESTIMATED PARAMETERS FOR STATISTIC MODEL

PDF	Log-Logistic	Log-normal
200MHz	$\hat{\mu} = -3.79907$ $\hat{\sigma} = 0.43948$ $\varepsilon_\mu = 0.0517626$ $\varepsilon_\sigma = 0.0250518$	$\hat{\mu} = -3.69473$ $\hat{\sigma} = 0.811659$ $\varepsilon_\mu = 0.0550099$ $\varepsilon_\sigma = 0.0390963$
400MHz	$\hat{\mu} = -3.75666$ $\hat{\sigma} = 0.482505$ $\varepsilon_\mu = 0.071783$ $\varepsilon_\sigma = 0.035901$	$\hat{\mu} = -3.61265$ $\hat{\sigma} = 0.917049$ $\varepsilon_\mu = 0.0795182$ $\varepsilon_\sigma = 0.0565477$
Outdoor UWB	$\hat{\mu} = -3.30616$ $\hat{\sigma} = 0.590192$ $\varepsilon_\mu = 0.202988$ $\varepsilon_\sigma = 0.101636$	$\hat{\mu} = -3.13344$ $\hat{\sigma} = 1.12623$ $\varepsilon_\mu = 0.225245$ $\varepsilon_\sigma = 0.164277$
PDF	Weibull	Rayleigh
200MHz	$\hat{a} = 0.0388139$ $\hat{b} = 1.00543$ $\varepsilon_a = 0.0027934$ $\varepsilon_b = 0.00456447$	$\hat{b} = 0.0474046$
400MHz	$\hat{a} = 0.0447926$ $\hat{b} = 0.903163$ $\varepsilon_a = 0.00458706$ $\varepsilon_b = 0.0536079$	$\hat{b} = 0.0609159$
Outdoor UWB	$\hat{a} = 0.080002$ $\hat{b} = 0.765597$ $\varepsilon_a = 0.0222858$ $\varepsilon_b = 0.106023$	$\hat{b} = 0.141188$

demonstrates that LLD turns out to be the model that fits the channel data best.

TABLE III
ROOT MEAN SQUARE ERROR (RMSE) COMPARISON BETWEEN STATISTIC MODELS

PDF	Log-Logistic	Log-normal	Weibull	Rayleigh
200MHz	5.7016	6.2850	8.8810	9.7562
400MHz	5.9023	6.5635	9.7056	10.3359
UWB	2.1867	2.4756	3.0136	4.8975

One may also draw the above conclusion from the Fig. 14, which describes the the goodness-of-fit in curve. The absolute amplitude of clusters have been plotted in terms of histogram. It can be easily seen that Rayleigh model provides the worst goodness-of-fit compared to LLD, log-normal and Weibull, so that exponential PDP of the clusters adopted in S-V model can not be applied in outdoor NLOS environment. Also, Weibull is not a good choice due to the inaccurate kurtosis and high tails. Compare LLD with log-normal, it is obvious that LLD is able to provide shaper kurtosis, shaper slope, and lower tail. In other word, LLD provides better goodness-of-fit than that of log-normal.

Since the above investigations have shown that LLD can better characterize the multipath gain amplitude for outdoor NLOS narrowband and UWB channels than log-normal, we may suggest an additional LLD variable to represent the fluctuations of the total multi-path gain. Moreover, similar to the IEEE UWB model, the phase of each path in outdoor NLOS environment may assumed to be either 0 or π with equal probability.
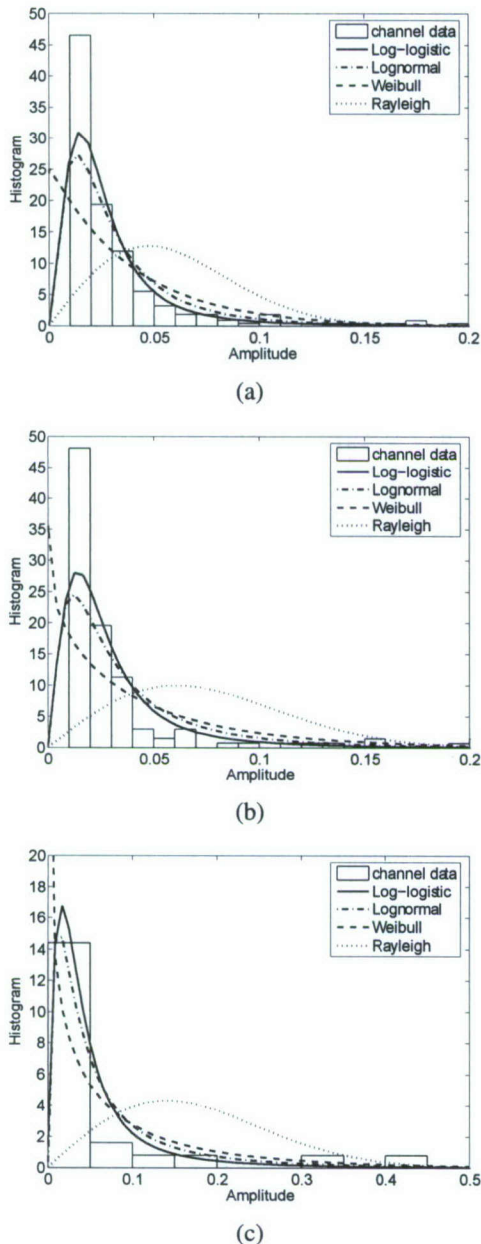
Fig. 14.   Goodness-of-fit (a)200MHz (b)400MHz (c)UWB

V. Conclusion

In our investigation, we accomplished following conclusions: 1) Outdoor NLOS channels are frequency dependent as intervening materials have dielectric properties that are strongly frequency dependent. 2) Both narrowband and UWB channels are made up of multipath and time-varying components. 3) In outdoor NLOS environment, the largest scattering, i.e., the highest magnitude does not always appear at the first path. 4) The outdoor UWB channels we obtained are similar in their basic features as indoor models. However, they are different in the arrival of cluster and subsequent rays as well as envelope decay. 5) The amplitude of channel coefficient at each path can be more accurately characterized as log-logistic distribution (LLD) other than log-normal, Weibull or Rayleigh due to the best goodness-of-fit and smallest root-mean-square (RMS).

References

[1] H. Hashemi, "The indoor Radio Propagaion Channel", *Proceedings of the IEEE*, vol. 81, pp. 943-968, July 1993.

[2] A. A. M. Saleh and R. A. Valenzuela, "A statistical Model for Indoor Multipath Propagation", *IEEE Journal on selected areas in communications*, vol. SAC-5, pp. 128-137, 1987

[3] T. S. Rappaport, "Characterization of UHF multipath radio channels in factory buildings", *IEEE Transactions on Antennas and Propagation*, vol. 37, pp. 1058-1069, Aug. 1989

[4] R. J. -M. Cramer, R. A. Scholtz and M. Z. Win, "Evaluation of an ultrawide-band propagation channel", *IEEE Transactions on Antennas and Propagation*, vol. 50, pp. 561 - 570, May 2002.

[5] J. A. Högbom, "Aperture Synthesis with a non-regular distribution of interferometer baselines", *Astronomy and Astrophysics Supplement Ser.*, vol. 15, pp. 417-426, 1974.

[6] Q. Spencer, M. Rice, B. Jeffs and M. Jensen, "A Statistical Model for the Angle-of-Arrival in Indoor Multipath Propagation", *IEEE Vehicular Technology Conference*, IEEE 1997, pp. 1415-1419.

[7] G. L. Turin, "Introduction to Spread Spectrum Antimultipath Techniques and their Application to Urban Digital Radio", Proc. IEEE, vol. 68, March 1980, pp. 328-354.

[8] J. H. Reed, *An introduction to Ultra Wideband Communication Systems*, Prentice Hall, 2005.

[9] A. A. Saleh and R. A. Valenzuela, "A statistical model for indoor multipath propagation", *IEEE J. on Selected Areas in Communications*, vol. 5, no.2, pp. 128-137, Feb 1987.

[10] IEEE 802. 15. SG3a, "Channel modeling sub-committee report final," *IEEE P802.15-02/490r1-SG3a*, Feb 2003.

[11] M. -G. Di Benedetto and G. Giancola, *Understanding ultra wideband Radio Fundamentals*, Prentice Hall, 2004.

[12] R. C. Gupta, O. Akman and S. Lvin, "A Study of Log-Logistic Model in Survival Analysis", *Biometrical Journal*, 41, pp. 431-443, 1999

[13] I. W. Burr, "Cumulative frequency functions", *Ann. Math. Statist.*, 13, 215-232, 1942.

[14] P. W. Mielke, and E. S. Johnson, "Three-parameter kappa distribution maximum likelihood estimates and likelihood ratio tests",*Monthly Weather Rev.*, 101, 701-709, 1973.

[15] K. S. Lee, J. Sadeghipour and J. A. Dracup, "An approach for frequency analysis of multiyear dought duration", *Wat. Resour. Res.* 22(5), 655-662, 1986.

[16] M. M. Shoukri, I. U. H. Mian, and D. S. Tracy, " Sampling properties of estimators of the log-logistic distribution with application to Canadian precipitation data", *Can. J. Statist.* 16(3), 223-236, 1988.

[17] N. K. Narda and R. K. Malik, "Dynamic model of root growth and water uptake in wheat", *Indian J. Agric. Engng* 3(3&4), 147-155, 1993.

[18] E. Limpert, W. Stahel and M. Abbt, "Log-normal Distributions across the Sciences: Keys and Clues", *BioScience*, 51 (5), pp. 341C352, 2001.

[19] W. Weibull, "A statistical distribution function of wide applicability", J. Appl. Mech.-Trans. ASME 18(3), 293-297, 1951.

[20] Devore, *Probability and Statistics for Engineering and the Sciences*, Monterey, CA: BrooksiCole, 1982.

[21] M. Barkat, *Signal deteciton and estimation*, 2nd, London: Artech house, 2005.

PUNCTURED BINARY SEQUENCE-PAIR AND ITS APPLICATION IN RADAR SYSTEM

Lei Xu and Qilian Liang
Department of Electrical Engineering
University of Texas at Arlington
416 Yates Street
Nedderman Hall, Rm 501
Arlington, TX 76010
Email: xu@wcn.uta.edu, liang@uta.edu

Ting Jiang
Wireless Network Lab
School of Telecommunications Engineering
Beijing University of
Posts and Telecommunication
Beijing 100876, China
Email: tjiang@bupt.edu.cn

I. ABSTRACT

This paper presents new developed code – punctured binary sequence-pair. The definitions and the autocorrelation properties of the proposed code are given. Doppler shift performance is also investigated. The significant advantages of punctured binary sequence-pair over conventional pulse compression codes, such as the widely used Barker codes, are zero autocorrelation sidelobes and the longer length of the code which can be as long as 31 so far. In the radar target detection system simulation, punctured binary sequence-pair also outperforms other conventional pulse compression codes. Therefore, our proposed code can be used as one of the candidates for pulse compression code.

II. INTRODUCTION

Pulse compression, which allows a radar to simultaneously achieve the energy of a long pulse and the resolution of a short pulse without the high peak power required by a high energy short duration pulse [1], is generally used in modern radar system. The main purpose of this technique is to raise the signal to maximum sidelobe (signal-to-sidelobe) ratio to improve the target detection and range resolution abilities of the radar system. The range sidelobes are harmful because they can mask main peaks caused by small targets situated near large targets. The lower the sidelobes, relative to the mainlobe peak, the better the main peak can be distinguished.

In the industrial world, pulse compression is one of the significant factors to determine the performance of high detection and high resolution radar. For example, a satellite-borne rain radar demands very stringent requirements on range sidelobe level of -60dB [2], a downward looking rain measuring radar requires a range sidelobe of 55dB under the mainlobe level [3] [4], and the air traffic control system demands the sidelobe level lower -55dB [5].

There are two kinds of basic waveform designs suitable for pulse compression: frequency-codes, such as linear frequency modulation(LFM) codes [6] [7] and nonlinear frequency modulation codes(NLFM) [7] [8] [9]; phase-coded waveforms, such as binary phase codes and polyphase codes. For a phase-coded waveform, a long pulse of duration T is divided into N subpulses each of width T_s. Each subpulse has a particular phase, which is selected in accordance with a given code sequence. And the pulse compression ratio equals to the number of subpulses $N = T/T_s \approx BT$, where the bandwidth is $B \approx 1/T_s$.

A common form of phase coding is *binary phase coding*, in which the phase of each subpulse is selected to be either 0 or π radians. Since the binary phase codes are easy to generate, they are widely used in modern radar system. However, when the selection of the phase is made randomly, the expected maximum sidelobe is only about $2/N$ of the peak of the compressed pulse. So completely random selection of the phase, is not a good idea, and the criterion for selecting the subpulse phases is that all the time-sidelobe of the compressed pulse should be equal and as low as possible. One family of binary phase code widely used nowadays that can produce compressed waveforms with constant sidelobe levels equal to unity is the Barker code. It has special features with which its sidelobe structure contains the minimum energy which is theoretically possible for binary codes, and the energy is uniformly distributed among the sidelobes(the sidelobe level of the Barker codes is $1/N^2$ that of the peak signal) [10]. Unfortunately, the length N of known binary and complex Barker codes is limited to 13 and 25, respectively [11], which may not be sufficient for the desired radar applications. In [12] [13] [14], polyphase codes, with better Doppler tolerance and lower range sidelobes such as the Frank and P1 codes, the Butler-matrix derived P2 code and the linear-frequency derived P3 and P4 codes were intensively analyzed. However, the low range sidelobe of the polyphase codes can not reach the level zero either. The structure of polyphase codes is more complicated and is not easy to generate comparing with binary codes. Therefore, we propose and analyze a new kind of code–punctured binary sequence-pair, whose sidelobe level is as low as 0 and the longest length of which is 31 in this paper, and subsequently apply it to radar system. According to the simulation results, the new code can be a good alternative for the current used pulse compression codes in radar system.

The rest of the paper is organized as following. Section 2 introduces the basic concept and properties of our proposed code. In Section 3, an example of punctured binary sequence-pair is given and its properties are investigated. In Section 4, the performance of our proposed code is also simulated and analyzed in radar targets detection system. In Section 5, some conclusions are drawn about the punctured binary sequence-pair.

III. DESIGN OF PUNCTURED BINARY SEQUENCE-PAIR

First of all, there are some relating definitions listed here.

Definition 1 A sequence-pair (x, y) is made up of two N-length sequences $\mathbf{x} = (x_0, x_1, \cdots, x_{N-1})$ and $\mathbf{y} = (y_0, y_1, \cdots, y_{N-1})$,

$$R_{xy}(\tau) = \sum_{j=0}^{N-1} x_j y^*_{(j+\tau)modN}, 0 \le \tau \le N-1 \quad (1)$$

is called the periodic autocorrelation function of the sequence pair, while $x = y$, the sequence-pair (x, y) turns to be a one-sequence code.

Definition 2 [15] Sequence $y = (y_0, y_1, \cdots, y_{N-1})$ is the punctured sequence for $x = (x_0, x_1, \cdots, x_{N-1})$,

$$y_j = \begin{cases} 0 & j \in p\text{-}punctured\ bits \\ x_j & j \in Non\text{-}punctured\ bits \end{cases} \quad (2)$$

Where p is the number of punctured bits in sequence x, suppose $x = [-1, 1]$, y is p-punctured binary sequence, (x, y) is called a punctured binary sequence-pair.

Definition 3 The periodic autocorrelation of punctured sequence-pair (x, y) is defined

$$R_{xy}(\tau) = \sum_{j=0}^{N-1} x_j y^*_{(j+\tau)modN}, 0 \le \tau \le N-1$$

When punctured sequence-pair has the following autocorrelation property

$$R_{xy}(\tau) = \begin{cases} E & \tau \equiv 0 \bmod N \\ 0 & otherwise \end{cases} \quad (3)$$

it is called perfect punctured sequence-pair [15]. Here, $E = \sum_{j=0}^{N-1} x_i y_i = N - p$, is the energy of punctured sequence-pair. Then binary sequence-pair (x, y) is called a p-punctured sequence-pair. The energy efficiency of the sequence-pair is defined as

$$\eta = \frac{E}{N} = \frac{N\text{-}p}{N} \quad (4)$$

Definition 4 The balance of the sequence x is defined as $I = \sum_{j=0}^{N-1} x_j = n_p - n_n$, while n_p, n_n are the number of $'+1'$ and $'-1'$ in x separately.

Theorem 1 Mapping property, if $x_1(i) = x(-i), y_{1(i)} = y(-i)$, then sequence-pair (x_1, y_1) is perfect punctured binary sequence-pair.

Theorem 2 Opposite to element symbol property, if $x_1(i) = -x(i), y_1(i) = -y(i)$, then sequence-pair (x_1, y_1) is perfect punctured binary sequence-pair.

Theorem 3 Cyclic shift property, if $x_1(i) = -x(i + u), y_1(i) = -y(i + u)$, then sequence-pair (x_1, y_1) is perfect punctured binary sequence-pair.

Theorem 4 Periodically sampling property, if $x_1(i) = -x(ki), y_1(i) = -y(ki), k$ and N are relatively prime, then sequence-pair (x_1, y_1) is perfect punctured binary sequence-pair.

In [15], the perfect punctured binary sequence-pairs of length from 3 to 31 are presented in the Table 1.

IV. PROPERTIES

A. Autocorrelation Properties

The autocorrelation function is one of the most important properties that represents the compressed pulse in an ideal pulse compression system, because it is proportional to the matched filter response in the noise-free condition. As presented in the equation (4) in the last section, the periodic autocorrelation function of the punctured binary sequence-pair is

$$R_{xy}(\tau) = \sum_{j=0}^{N-1} x_j y^*_{(j+\tau)modN} = \begin{cases} E & \tau \equiv 0 \bmod N \\ 0 & otherwise \end{cases}$$

EXAMPLE
The autocorrelation property of 13-length punctured binary sequence pair(x, y), $(x = (111 - 111 - 1 - 1 - 1 - 111 - 1)$ and $y = (1010110000110))$, and that of 31-length punctured binary sequence-pair(x, y), $(x = (1111 - 1 - 1 - 11 - 11 - 1111 - 1 - 1 - 1 - 11 - 1 - 11 - 1 - 1111 - 111 - 1)$ and $y = (1111000101011100001001001110110))$ are shown in the Fig.1 and Fig.2.

As it is known that a suitable criterion for evaluating code of length N is the peak signal to peak signal sidelobe ratio (PSR) of their aperiodic autocorrelation function, which can be bounded by [16]

$$[PSR]_{dB} \le 20logN = [PSR_{max}]_{dB} \quad (5)$$

The only uniform phase codes that can reach the PSR_{max} are the Barker codes whose length is equal or less than 13. However, the sidelobe of the new code in both Fig.1 and Fig.2 can be as low as 0. In some other words, the peak signal to peak signal sidelobe can be as large as infinite. In addition, it is also obvious that the length of the new code can expend to 31 that is much longer than the length of the Barker code.

2

TABLE I
OPTIMUM PUNCTURED BINARY SEQUENCE-PAIR

Length	Sequence (octet)	Punctured positions	Energy Efficiency(%)
3	6	3	66.67
5	32	3 4 5	40.00
5	34	2 4 5	40.00
7	162	4 5 7	57.14
7	164	4 6 7	57014
9	652	1 2 3 4 5 6 7	22.22
9	760	1 2 3 4 6 7 8	22.22
11	3426	4 5 6 8 11	54.54
11	3550	4 7 9 10 11	54.54
12	7426	1 6 7 12	66.67
12	7550	4 5 10 11	66.67
12	7624	3 6 9 12	66.67
13	16606	2 4 7 8 9 10 13	46.15
13	17124	5 6 8 9 10 12 13	46.15
15	74232	5 6 7 9 10 13 15	53.33
15	75310	6 7 10 11 13 14 15	53.33
17	351134	4 6 7 8 9 10 12 16 17	47.06
17	372142	3 6 8 9 10 13 14 15 17	47.06
19	1715412	5 6 9 12 13 14 15 17 19	52.63
19	1724154	5 7 9 10 11 12 15 18 19	52.63
20	3433330	2 5 6 7 8 9 12 15 16 17 18 19	40.00
20	3610556	1 6 7 8 9 10 11 16 17 18 19 20	40.00
21	7405316	2 5 6 7 8 9 11 13 14 16 17 20 21	38.10
21	7563240	3 5 6 9 10 12 13 15 17 18 19 20 21	38.10
23	37024632	6 7 8 9 11 13 14 17 18 21 23	52.17
23	37263120	6 8 11 12 15 16 18 20 21 22 23	52.17
28	1702164566	4 5 6 7 10 11 18 19 20 21 24 25	57.14
28	1734164226	4 5 8 9 10 11 18 19 22 23 24 25	57.14
28	1740465534	4 6 7 9 10 13 18 20 21 23 24 27	57.14
29	3556415302	4 7 11 13 14 15 16 19 20 21 24 25 26 27 29	48.28
29	3642213634	5 7 8 9 11 12 14 15 16 18 23 24 26 28 29	48.28
31	17053411166	5 6 7 9 11 15 16 17 18 20 21 23 24 28 31	51.61
31	17464412730	6 7 10 12 13 15 16 17 18 20 22 26 29 30 31	51.61

Note: The sequences in the table are presented by octets, '1' for '+1', '0' for '-1' and punctured positions begins from left to right.

B. Ambiguity Function

When the transmitted impulse is reflected by a moving target, the reflected echo signal includes a linear phase shift which corresponds to a Doppler shift f_d [17]. As a result of the Doppler shift f_d, the main peak of the autocorrelation function is reduced:

$$[d]_{dB} = 10 log \frac{\int_0^T x(s)x^*(s)ds}{\int_0^T x(s)e^{j2\pi f_d T_c}x^*(s)ds} \qquad (6)$$

In addition, the SNR degraded and the sidelobe structure is changed thanks to the Doppler shift.

(a)

(b)
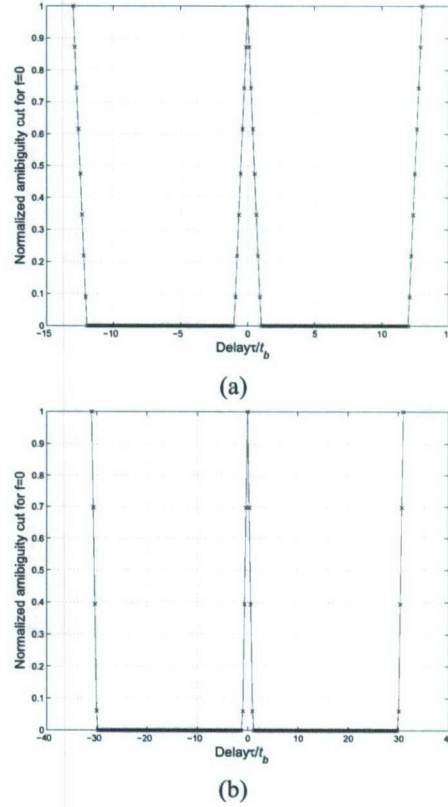
Fig. 1. Periodic autocorrelation property of punctured binary sequence-pair: (a) 13 length code (b) 31 length code

The ambiguity function which is usually used to analyze the radar performance of Doppler shift and time delay can be found in [17]

$$y(t, F_D) = \int_{-\infty}^{\infty} x(s)e^{j2\pi F_D s}x^*(s-t)ds \equiv \hat{A}(t, F_D) \qquad (7)$$

where t is the time delay and F_D is the Doppler shift.

An equivalent definition can be given in terms of the signal spectrum by applying basic Fourier transform properties

$$\hat{A}(t, F_D) = \int_{-\infty}^{\infty} X^*(F)X(F - F_D)e^{j2\pi F t}dF \qquad (8)$$

The *ambiguity function* is defined as the magnitude of $\hat{A}(t, F_D)$ [17]

$$A(t, F_D) \equiv |\hat{A}(t, F_D)| \qquad (9)$$

However, the code used in our paper is sequence-pair, so the transmitting code and the receiving code are not the same. The ambiguity function can be obtained as following:

$$y_{pair}(t, F_D) = \int_{-\infty}^{\infty} x(s)e^{j2\pi F_D s}y^*(s-t)ds \qquad (10)$$

$$\hat{A}_{pair}(t, F_D) = \int_{-\infty}^{\infty} X^*(F)Y(F - F_D)e^{j2\pi F t}dF \qquad (11)$$

3

The *ambiguity function* is defined as the magnitude of $\hat{A}_{pair}(t, F_D)$

$$A_{pair}(t, F_D) \equiv |\hat{A}_{pair}(t, F_D)| \tag{12}$$

In addition, assume the punctured binary sequence-pair is (x, y), $x(t) = \sum_{n=0}^{N-1} x_n(t - nT_s)$ and $y(t) = \sum_{n=0}^{N-1} y_n(t - nT_s)$, since the periodic correlation is used instead of aperiodic correlation in this paper. The $\hat{A}_{pair}(t, F_D)$ in one period of length NT_s can be expressed as

$$\hat{A}_{pair}(t, F_D) = \int_0^t x(s - nT_s)y^*(s - nT_s - (NT_s - t))$$
$$e^{(j2\pi F_D s)}ds + \int_t^{(N-1)T_s} x(s - nT_s)y^*(s - nT_s - t)$$
$$e^{(j2\pi F_D s)}ds \tag{13}$$

EXAMPLE

Ambiguity functions of the punctured binary sequence-pair within length of 13 and 31 used in the last section are simulated, where maximal time delay is 1 unit(normalized to length of the code, in units of NT_s) and maximal Doppler shift is 5 units(normalized to the inverse of the length of the code, in units of $1/NT_s$). The ambiguity functions of 13-length long Barker code and 31-length long P4 code are presented in Fig.2 and Fig.3 in order to compare with the punctured binary sequence-pairs of the same length.

Fig.2 and Fig.3 show that the sidelobe improvement of the punctured binary sequence-pair is obvious comparing with those of Barker code and P4 code when there is no Doppler shift. The sidelobe of punctured binary sequence-pair can reach as low as zero. Nevertheless, when there are Doppler shift and time delay, the ambiguity functions of punctured binary sequence-pair is not as flat as those of Barker code or P4 code. In some other words, punctured binary sequence-pair is, to some extent, less tolerant of Doppler shifts than P4 code. One of the reasons why the proposed code is not tolerant of large Doppler shift is that periodic correlation property is used for punctured binary sequence-pair instead of the aperiodic correlation property which is used for the other two codes. However, comparing with P4 code, punctured binary sequence-pair made up of only three different phases, is more simple and easy to obtain in the industrial world.

C. Doppler Shift Performance Without Time Delay

The ambiguity function can be simplified when there is no time delay:

$$\hat{A}_{pair}(0, F_D) = \int_0^{T_s} x(s - nT_s)y^*(s - nT_s)e^{(j2\pi F_D s)}ds \tag{14}$$

However, in Fig.2 and Fig.3, it is not obvious to see the Doppler shift performance of punctured binary sequence-pair and the other two codes when there is no time delay. The Doppler shift performance without time delay is presented in Fig.4 and Fig.5.
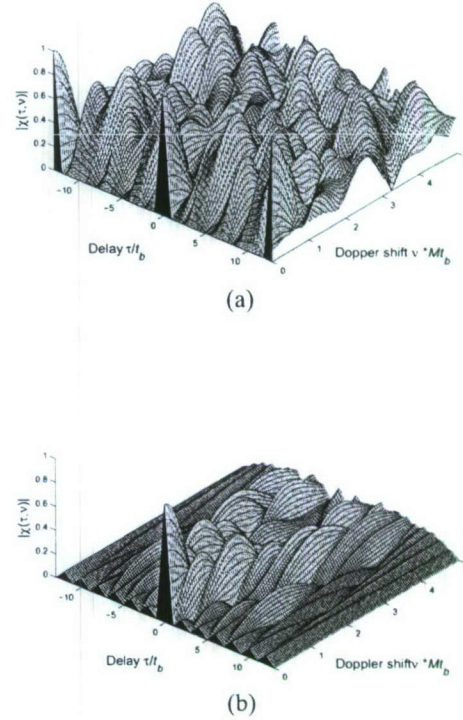

(a)

(b)

Fig. 2. Ambiguity function of 13-length codes: (a) Punctured binary sequence-pair (b) Barker code

Without time delay, while the Doppler shift is less than 1 unit (normalized to length of the code, in units of NT_s), punctured binary sequence-pair has the similar performance of Barker and P4 code that the amplitude has a sharp downward trend. Furthermore, amplitude of punctured binary sequence-pair decreases more quickly than amplitude of the other two codes. However, when the Doppler shift is larger than 1 unit (normalized to length of the code, in units of NT_s), the performances of these codes are distinguished. On one hand, the trend presented by punctured binary sequence-pair is not as regular as the other two kinds of code when the Doppler shift is larger than 1. On the other hand, for Barker and P4 code, when Doppler frequencies equal to multiples of the pulse repetition frequency ($PRF = 1/PRI = 1/Ts$) the ambiguity value turns to be zero. Because of these zeros, such multiples of the pulse repetition frequency will render the radar blind [1]to their velocities. Nevertheless, referring to punctured binary sequence-pair, ambiguity values do not go to zero when Doppler frequencies are equal to multiples of the PRF. Therefore, using the punctured binary sequence-pair as the compression code could, to some extent, improve the blind speed problem in moving target detection system.
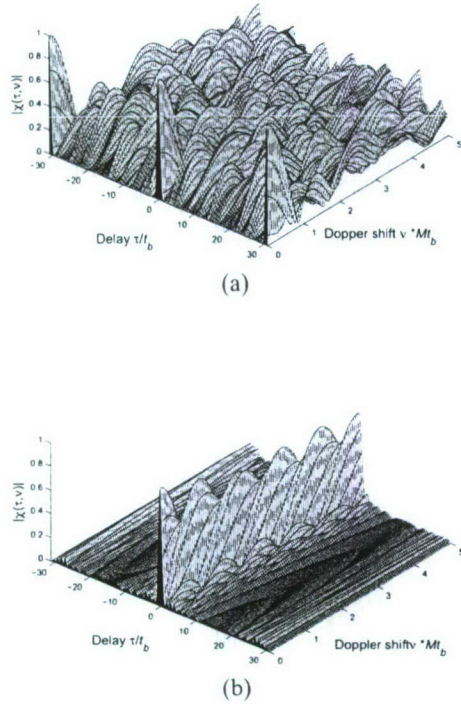
4

(a)

(b)

Fig. 3. Ambiguity function of 31-length codes: (a) Punctured binary sequence-pair (b) P4 code
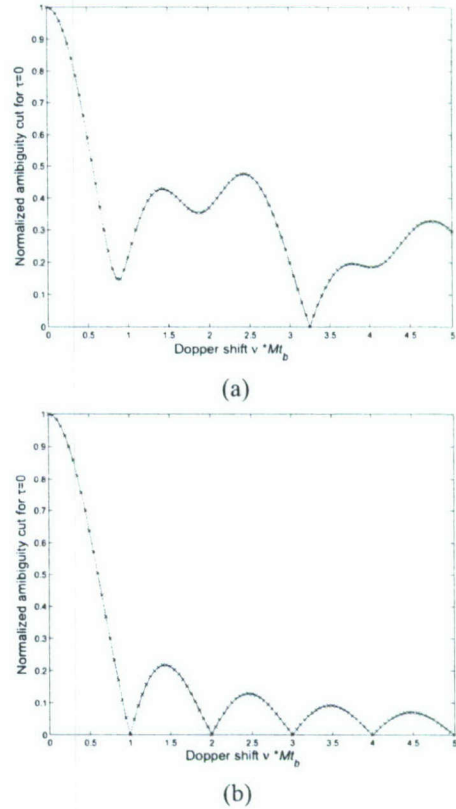

(a)

(b)

Fig. 4. Doppler shift of 13-length codes(time delay=0): (a) Punctured binary sequence-pair (b) Barker code

V. SYSTEM SIMULATION IN RADAR SYSTEM

As a rule, the following probabilities [17] are of most interest in the Radar system.

1. Probability of Detection, P_D: The probability that a target is declared when a target is in fact present.

2. Probability of False Alarm, P_{FA}: The probability that a target is declared when a target is in fact *not* present.

3. Probability of Miss, P_M: The probability that a target is *not* declared when a target is in fact present.

Note that $P_M = 1 - P_D$, thus, P_D and P_{FA} suffice to specify all of the probabilities of interest in radar system. Therefore, the above three probabilities of punctured binary sequence-pairs in radar system are simulated using Matlab, as shown in Fig.6 and Fig.7. In addition, the performance of the 13-length Barker code and 31-length P4 code are provided in order to compare with the performance of punctured binary sequence-pairs of corresponding lengths. In the simulation model, we ran Monte-Carlo simulation for 10^5 times at each SNR value, the Doppler shift frequency which is kept less than 1 unit (normalized to the inverse of the length of the code, in units of $1/NT_s$) is randomly determined by Matlab, and the time delay is assumed to be zero. We use threshold detection in coherent system and the threshold is adaptively determined in the simulation.

In Fig.6(a), we plotted the probabilities of miss P_M of 13-length punctured binary sequence-pair and the same length Baker code. Observe the figure, the probability of miss P_M of the system using 13-length punctured binary sequence-pair is lower than 13-length Barker code especially when the SNR is not large. It is in accordance with the result shown in Fig.4 that when Doppler shift is kept less than 1 and the time delay is zero, the amplitude of punctured binary sequence-pair falls more sharply than Barker code. In Fig.6(b), we plotted the probabilities of miss targets detection of 31-length punctured binary sequence-pair and those of the same length P4 code. The probability of miss targets detection of the system using 31-length punctured binary sequence-pair is less than 31-length P4 code especially when the SNR is not large. When SNR is larger than 17 dB, both probabilities of miss targets detection of the system approach zero. However, the probability of miss targets of P4 code is lower than punctured binary sequence-pair. Comparing both Fig.6(a) and Fig.6(b), longer punctured code performs better especially when the SNR is not very large.

In addition, we also plotted the probability of detection versus probability of false alarm of the coherent receiver in Fig.7.

Fig.7(a) illustrates performance of 13-length punctured binary sequence-pair and the same length Baker code when the SNR is 10dB and 14dB. Having the same SNR value such as
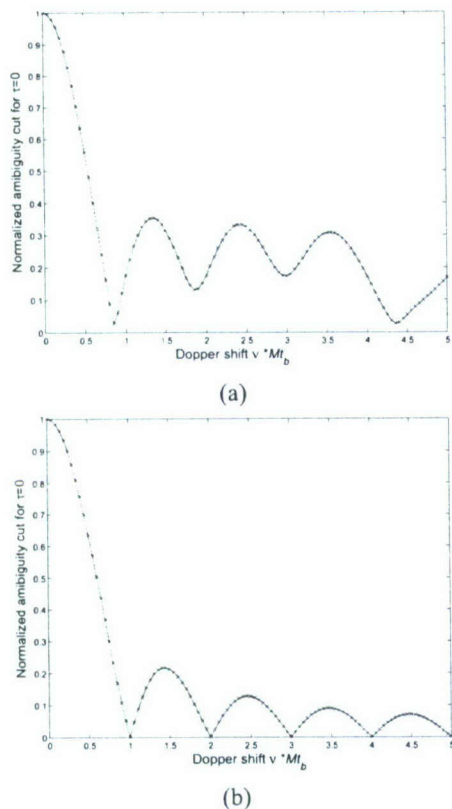
5

(a)

(b)

Fig. 5. Doppler shift of 31-length codes(time delay=0): (a) Punctured binary sequence-pair (b) P4 code
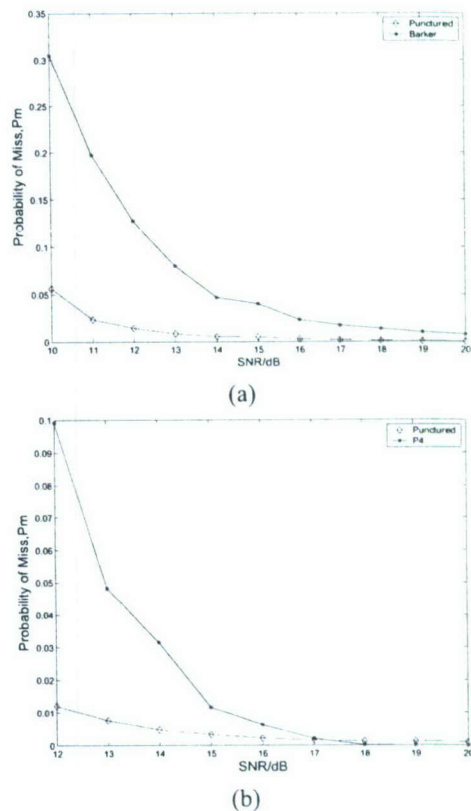

(a)

(b)

Fig. 6. Probability of miss targets detection (No time delay, Doppler shift less than 1): (a) 13-length Punctured binary sequence-pair VS. 13-length Barker code(b) 31-length Punctured binary sequence-pair VS. 31-length P4 code

10dB or 14dB in the figure, the P_D of 13-length punctured binary sequence-pair is larger than P_D of 13-length Barker code while the P_{FA} of the first code is also smaller than P_{FA} of the latter code. In some other words, 13-length punctured binary sequence-pair has much higher target detection probability while keeping a lower false alarm probability. Furthermore, observe Fig.7(a), 13-length punctured binary sequence-pair even has much better performance at 10dB SNR value than 13-length Barker code at 14dB SNR value. Similarly, Fig.7(b) shows that the performance of 31-length punctured binary sequence-pair is much better than the P4 code of same length. According to the above results, it is easy to see that our newly provided punctured binary sequence-pair is very promising to be an alternative pulse compression code in the Radar system.

VI. CONCLUSION

A kind of new code–punctured binary sequence-pair and its properties have been investigated in this paper. The significant advantage of the new code over conventional phase compression code is the considerably reduced sidelobe as low as zero and correspondingly the significantly improved PSR of the autocorrelation function. In addition, the length of punctured binary sequence-pair known can be as long as 31. The disadvantage of the new sequence-pair is that it is not so tolerant of Doppler shift when the Doppler shift is larger

than 1. We also apply the punctured binary sequence-pair to the target detection simulation in the radar system. According to the simulation results, it is easy to observe that 13-length punctured binary sequence-pair has better performance than 13-length Barker code. Similarly, the 31-length punctured binary sequence-pair performs better than 31-length P4 code when the Doppler shift is kept less than 1 unit(normalized to the inverse of the length of the code, in units of $1/NT_s$) in the radar target detection system. As a result, the general conclusion from the results presented in this paper is that the punctured binary sequence-pair, which has much longer code length and better autocorrelation sidelobe property than the biphase code such as Barker code, and simpler structure than those polyphase codes such as P4 code, effectively increases the variety of candidates for pulse compression codes especially for long code.

REFERENCES

[1] S. Ariyavisitakul, N. Sollenberger, and L. Greenstein, *Introduction to Radar System*, Tata McGraw-Hill, 2001.

6

[14] B. L. Lewis and F. F. Kretschuner, "Linear frequency modulation derived polyphase pulse compression codes", *IEEE Transactions on Aerospace and Electronic Systems,* AES-18, pp. 637-641, Sep. 1982.

[15] T. Jiang, *Research on Quasi-Perfect Binary Signal Pair and Perfect Punctured Binary Signal Pair Theory,* Ph.D Dissertation: Yanshan University, 2003.

[16] M. I. Skolnik, *Radar Handbook,* New York: McGraw-Hill, 1970.

[17] M. A. Richards, *Fundamentals of Radar Signal Processing,* McGraw-Hill, 2005.

(a)

(b)

Fig. 7. Probability of detection versus probability of false alarm of the coherent receiver(No time delay, Doppler shift less than 1): (a) 13-length Punctured binary sequence-pair VS. 13-length Barker code(b) 31-length Punctured binary sequence-pair VS. 31-length P4 code
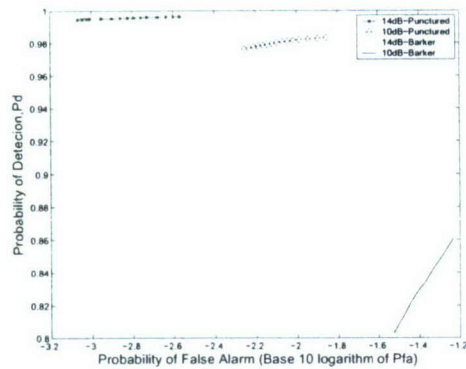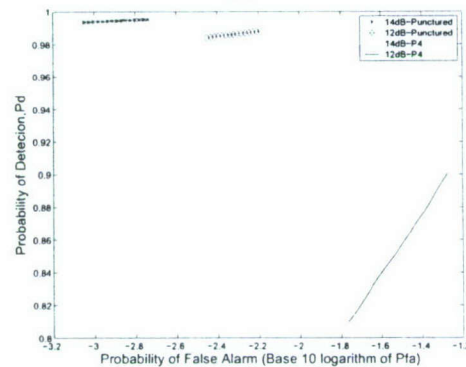
[2] H. D. Griffiths and L. Vinagre, "Design of low-sidelobe pulse compression waveforms," *Electronics Letters,* vol. 30, no. 12, pp. 1004-1005, Jun. 1994.

[3] T. Kozu, "Effects of signal decorrelation on pulse compressed waveforms ofr nadir-looking spacebone radar," *IEEE Trans. Geosci. Remote Sensing,* vol. 29, no. 5, pp. 786-790, Sep. 1991.

[4] A. Tanner, S. L. Durden, R. Denning, E. Im, F. K. Li, W. Ricketts, and W. Wilson, "Pulse compression with very low sidelobes in an airborne rain mapping radar," *IEEE Trans. Geosci. Remote Sensing,* vol. 32, no. 1, pp. 211-213, Jan. 1994.

[5] J. P. Larvor, "Digital pulse compression with low range sidelobes," *Int. Conference Radar,* pp. 391-394, 1992.

[6] J. R. Klauder, A. C. Price, S. Darlington and W. J. Albersheim, "The theory and design of chirp radars," *Bell System Technical Journal,* vol. 39, 745-808, Jul. 1960.

[7] C. E. Cook and M. Bernfeld, *Radar Signals, an Introduction to Theory and Application,* New York: Academic Press, 1967.

[8] J. W. Arthur, "SAW pulse compression in modern multi-channel radar applications", *Microwave Journal,* pp. 159-169, Jan. 1986.

[9] M. B. N. Butler, "Radar applications of SAW dispersive filters", *IEE Proceedings,* vol. 127, no. 2, pp. 118-124, Apr. 1980.

[10] J. L. Eaves and E. K. Reedy, *Principles of Modern Radar,* Van Nostrand Reinhold, 1987.

[11] L. Bomer and M. Antweiler, "Polyphase Barker sequences ," *Electronics Letters,* 1577-1579, Dc. 1989.

[12] R. L. Frank, "Polyphase codes with good nonperiodic correlation properties", *IEEE Transactions on Information Theory,* IT. -9, pp. 43-45, Jan. 1963.

[13] B. L. Lewis and F. F. Kretschuner, "A new class of polyphase pulse compression codes and techniques", *IEEE Transactions on Aerospace and Electronic Systems,* AES-17, pp. 364-372, May. 1981.

7

PERFECT PUNCTURED ZCZ SEQUENCE-PAIR SET: DESIGN, ANALYSIS AND APPLICATION TO RADAR

Lei Xu
Department of Electrical Engineering
University of Texas at Arlington
416 Yates Street
Nedderman Hall, Rm 205
Arlington, TX 76010
Email: xu@wcn.uta.edu

Qilian Liang
Department of Electrical Engineering
University of Texas at Arlington
416 Yates Street
Nedderman Hall, Rm 501
Arlington, TX 76010
Email: liang@uta.edu

I. ABSTRACT

Based on zero correlation zone(ZCZ) concept, the definition and properties of ZCZ sequence-pair set are given in this paper. A method is presented to use the perfect punctured sequence-pair together with Hadamard matrix in the zero correlation zone to construct the perfect punctured ZCZ sequence-pair set. According to performance analysis, perfect punctured ZCZ sequence-pair set has good autocorrelation and cross correlation properties when doppler shift is not large. The radar target detection system simulation results also show that perfect punctured ZCZ sequence-pair outperforms other conventional pulse compression codes, such as the well known polyphase code–P4 code. As a result, perfect punctured ZCZ sequence-pair set can be good candidate for pulse compression code.

II. INTRODUCTION

Pulse compression, known as a technique to raise the signal to maximum sidelobe(signal-to-sidelobe) ratio to improve the target detection and range resolution abilities of the radar system, allows a radar to simultaneously achieve the energy of a long pulse and the resolution of a short pulse without the high peak power which is required by a high energy short duration pulse [1]. One of the waveform designs suitable for pulse compression is phase-coded waveform design that a long pulse of duration T is divided into N subpulses each of width T_s. Each subpulse has a particular phase, which is selected in accordance with a given code sequence. The pulse compression ratio equals the number of subpulses $N = T/T_s \approx BT$, where the bandwidth is $B \approx 1/T_s$. In general, a phase-coded waveform with longer code word, in some other words, higher pulse compression ratio, can have lower sidelobe of autocorrelation, relative to the mainlobe peak, so its main peak can be better distinguished. The relative lower sidelobe of autocorrelation is very important since range sidelobe are so

harmful that they can mask main peaks caused by small targets situated near large targets. In addition, the cross-correlation property of the pulse compression codes should be considered in order to reduce the interference among radars when we choose a set of pulse compression codes, because in the real world, a radar may not work alone, such as in the RSN(Radar Sensor Network).

Much time and effort was put for designing sequences with good autocorrelation and cross correlation properties for radar target ranging and target detection. However, it is known that for most good binary sequences of length $N(N > 13)$ the attainable sidelobe levels are approximately $\sqrt{N}$ [2] [3] and the mutual cross correlation peaks of sequences of the same length are much larger and are usually in the order of $2\sqrt{(N)}$ to $3\sqrt{(N)}$. Set of binary sequences of length N with autocorrelation sidelobes and cross-correlation peak values both of approximately $\sqrt{(N)}$ are only achieved in paper [4]. In addition to binary sequences, polyphase codes, with better Doppler tolerance and lower range sidelobes such as the Frank and P1 codes, the Butler-matrix derived P2 code and the linear-frequency derived P3 and P4 codes were provided and intensively analyzed in [5] [6] [7]. Nevertheless, the range sidelobe of the polyphase codes can not be as low as zero either. The structure of polyphase codes is more complicated and is not easy to generate comparing with binary codes. Therefore, based on ZCZ (zero-correlation zone) [8] concept, we propose the ZCZ sequence-pair set, which can reach zero autocorrelation sidelobe during zero correlation zone and zero mutual cross correlation peaks during the whole period. We also propose and analyze a method that perfect punctured sequence-pair together with Hadamard matrix are used in the zero correlation zone to construct the perfect punctured ZCZ sequence-pair set and subsequently apply it to radar detection system. For the performance evaluation of this proposed code, an example is presented, investigated and studied in the radar targets detection simulation system in the paper. Because of the ideal property performance and good target detection

performance in simulation system, our proposed new code can be another useful candidate for pulse compression application, especially in the RSN.

The rest of the paper is organized as follows. Section 2 introduces the definition and properties of ZCZ sequence-pair set. In Section 3, the perfect punctured ZCZ sequence-pair set is introduced, and a method using perfect punctured sequence-pair and Hadamard matrix to construct ZCZ sequence-pair set is given and proved. In Section 4, the properties and ambiguity function of perfect punctured ZCZ sequence pair set are simulated and analyzed. The performance of perfect punctured ZCZ sequence-pair set is investigated in radar targets detection simulation system comparing with P4 code. In Section 6, conclusions are drawn on perfect punctured ZCZ sequence-pair set.

III. THE DEFINITION AND PROPERTIES OF ZCZ SEQUENCE-PAIR SET

Zero correlation zone(ZCZ) is a new concept provided by Fan [8] [9] [10] in which the autocorrelation and cross correlation sidelobes are zero while the time delay is kept within the value τ instead of the whole period of time domain.

We consider ZCZ sequence-pair set(X, Y), X to be a set of K sequences of length N and Y to be a set of K sequences of the same length N:

$$x^{(p)} \in X \quad p = 0, 1, 2, ..., K-1 \tag{1}$$

$$y^{(q)} \in Y \quad q = 0, 1, 2, ..., K-1 \tag{2}$$

The autocorrelation function for sequence-pair (x^p, y^p) is defined by:

$$R_{x^{(p)}y^{(p)}}(\tau) = \sum_{i=0}^{N-1} x_i^{(p)} y_{(i+\tau)modN}^{(p)*}, 0 \leq \tau \leq N-1 \tag{3}$$

The cross correlation function for sequence-pair (x^p, y^p) and (x^q, y^q), $p \neq q$ is defined by:

$$C_{x^{(p)}y^{(q)}}(\tau) = \sum_{i=0}^{N-1} x_i^{(p)} y_{(i+\tau)modN}^{(q)*}, 0 \leq \tau \leq N-1 \tag{4}$$

$$C_{x^{(q)}y^{(p)}}(\tau) = \sum_{i=0}^{N-1} x_i^{(q)} y_{(i+\tau)modN}^{(p)*}, 0 \leq \tau \leq N-1 \tag{5}$$

For pulse compression sequences, some properties are of particular concern in the optimization of any design. They are peak sidelobe level, the energy of autocorrelation sidelobes and energy of their mutual cross correlation [4]. So the peak sidelobe level which represents a source of mutual interference that can obscure weaker targets can be presented as $\max_K |R_{x^p y^p}(\tau)|, \tau \in Z_0$(zero correlation zone) for ZCZ sequence-pair set. The another optimization criterion for the set of sequence-pair is the energy of autocorrelation sidelobes together with the energy of cross correlation. By minimizing the energy, it can be distributed evenly and the peak autocorrelation level can be minimized as well [4]. Here, the energy

of ZCZ sequence-pair set can be employed as:

$$E = \sum_{p=0}^{K-1} \sum_{\tau=1}^{Z_0} R_{x^{(p)}y^{(p)}}^2(\tau) + \sum_{p=0}^{K-1} \sum_{q=0}^{K-1} \sum_{\tau=0}^{N-1} C_{x^{(p)}y^{(q)}}(\tau) \tag{6}$$
$$(p \neq q)$$

According to (7), it is obvious to see that the energy can be kept low while minimizing the autocorrelation and cross correlation of the sequence-pair set.

Then, the ZCZ sequence-pair set can be constructed to minimize the autocorrelation and cross correlation of the sequence-pair set and the definition of ZCZ sequence-pair set can be expressed:

Definition 2-1 Assume$(x_i^{(p)}, y_i^{(p)})$ to be sequence-pair set of length N and number of sequence-pair K, where $p = 1, 2, 3, ..., N-1, i = 0, 1, 2, ..., K-1$, if all the sequences in the set satisfy the following equation:

$$R_{x^{(p)}y^{(q)}}(\tau) = \sum_{i=0}^{N-1} x_i^{(p)} y_{(i+\tau)mod(N)}^{(q)*} = \sum_{i=0}^{N-1} y_i^{(p)} x_{(i+\tau)mod(N)}^{(q)*}$$

$$= \begin{cases} \lambda N, & \text{for } \tau = 0, p = q \\ 0, & \text{for } \tau = 0, p \neq q \\ 0, & \text{for } 0 < |\tau| \leq Z_0 \end{cases} \tag{7}$$

where $0 < \lambda \leq 1$, then $(x_i^{(p)}, y_i^{(p)})$ is called ZCZ sequence-pair set, $ZCZP(N, K, Z_0)$ is a symbol in short.

IV. PERFECT PUNCTURED ZCZ SEQUENCE-PAIR SET

A. Definition of Perfect Punctured ZCZ Sequence-pair Set

Matsufuji and Torii have provided some methods of constructing ZCZ sequences in [11] [12]. In this section, we apply perfect punctured sequence-pair [13] in zero correlation zone to construct the perfect punctured ZCZ sequence-pair set.

Definition 3-1 [13] Sequence $u = (u_0, u_1, ..., u_{N-1})$ is the punctured sequence for $v = (v_0, v_1, ..., v_{N-1})$,

$$u_j = \begin{cases} 0, & \text{if } j \in p \text{ punctured bits} \\ v_j, & \text{if } j \in \text{Non-punctured bits} \end{cases} \tag{8}$$

Where p is the number of punctured bits in sequence v, suppose $v_j = (-1, 1)$, u is p-punctured binary sequence, (u, v) is called a punctured binary sequence-pair.

Theorem 3-1 [13] The autocorrelation of punctured sequence-pair (u, v) is defined

$$R_{uv}(\tau) = \sum_{i=0}^{N-1} u_i v_{(i+\tau)modN}, 0 \leq \tau \leq N-1 \tag{9}$$

If the punctured sequence-pair has the following autocorrelation property:

$$R_{uv}(\tau) = \begin{cases} E, & \text{if } \tau \equiv 0 modN \\ 0, & \text{others} \end{cases} \tag{10}$$

the punctured sequence-pair is called perfect punctured sequence-pair [13]. Where, $E = \sum_{i=0}^{N-1} u_i v_{(i+\tau)modN} = N - p$, is the energy of punctured sequence-pair.

2

If $(x_i^{(p)}, y_i^{(p)})$ in Definition 2-1 is constructed by perfect punctured sequence-pair and a certain matrix, such as Hadamard matrix or an orthogonal matrix, where

$$x_i^{(p)} \in (-1, 1), \quad i = 0, 1, 2, ..., N-1$$
$$y_i^{(q)} \in (-1, 0, 1), \quad i = 0, 1, 2, ..., N-1$$

$$R_{x^{(p)}y^{(q)}}(\tau) = \sum_{i=0}^{N-1} x_i^{(p)} y_{(i+\tau)modN}^{(q)*} = \sum_{i=0}^{N-1} y_i^{(p)} x_{(i+\tau)modN}^{(q)*}$$

$$= \begin{cases} \lambda N, & \text{for } \tau = 0, p = q \\ 0, & \text{for } \tau = 0, p \neq q \\ 0, & \text{for } 0 < |\tau| \leq Z_0 \end{cases} \quad (11)$$

where $0 < \lambda \leq 1$, then $(x_i^{(p)}, y_i^{(p)})$ can be called perfect punctured ZCZ sequence-pair set.

B. Design for Perfect Punctured ZCZ Sequence-pair Set

Based on odd length perfect punctured binary sequence pairs and a Hadamard matrix, a perfect punctured ZCZ sequence-pair set can be constructed on following steps:

Step 1: Considering an odd length perfect punctured binary sequence-pair (u, v), the length of each sequence is N_1

$$u = u_0, u_1, ..., u_{N_1-1}, u_i \in (-1, 1),$$
$$v = v_0, v_1, ..., v_{N_1-1}, v_i \in (-1, 0, 1),$$
$$i = 0, 1, 2, ..., N_1 - 1, N_1 \ odd$$

Step 2: Consider Walsh sequences set B, the length of the sequence is N_2 which is equal to the number of the sequences. In some other words, a Hadamard matrix of order N_2 is considered.

$$B = (b^0, b^1, ..., b^{N_2-1}),$$
$$b^i = (b_0^i, b_1^i, ..., b_{N_2-1}^i),$$
$$R_{b^i b^j} = \begin{cases} N_2, & \text{if } i = j \\ 0, & \text{if } i \neq j \end{cases}$$

Step 3: Doing bit-multiplication on the perfect punctured binary sequence-pair and each line of Walsh sequences set B(Hadamard matrix), then sequence-pair set (X, Y) is obtained,

$$b^i = (b_0^i, b_1^i, ..., b_{N_2-1}^i), i = 0, 1, ..., N_2 - 1,$$
$$x_j^i = u_{jmodN_1} b_{jmodN_2}^i, 0 \leq i \leq N_2 - 1, 0 \leq j \leq N - 1,$$
$$X = (x^0, x^1, ..., x^{N_2-1}),$$
$$y_j^i = v_{jmodN_1} b_{jmodN_2}^i, 0 \leq i \leq N_2 - 1, 0 \leq j \leq N - 1,$$
$$Y = (y^0, y^1, ..., y^{N_2-1})$$

Where $GCD(N_1, N_2) = 1$, common divisor of N_1 and N_2 is 1, $N = N_1 * N_2$. The sequence-pair set (X, Y) is perfect punctured ZCZ sequence-pair set and $N_1 - 1$ is the zero correlation zone Z_0. The length of each sequence in perfect punctured ZCZ sequence-pair set is $N = N_1 * N_2$ that depends on the product of length of perfect punctured sequence-pair and the length of Walsh sequence in Hadamard matrix. The

number of sequence-pair in perfect punctured ZCZ sequence-pair set rests on the order of the Hadamard matrix. The sequence x^i in sequence set X and the corresponding sequence y^i in sequence set Y construct a sequence-pair (x^i, y^i) that can be used as a pulse compression code.

The correlation property of the sequence-pair in perfect punctured ZCZ sequence-pair set is:

$$\begin{aligned} R_{x^i y^j}(\tau) &= R_{x^j y^i}(\tau) = R_{uv}(\tau mod N_1) R_{b^i b^j}(\tau mod N_2) \\ &= R_{uv}(\tau mod N_1) R_{b^j b^i}(\tau mod N_2) \\ &= \begin{cases} EN_2, & \text{if } \tau = 0, i = j \\ 0, & \text{if } 0 < |\tau| \leq N_1 - 1, i = j \quad (12) \\ 0, & \text{if } i \neq j \end{cases} \end{aligned}$$

where $N_1 - 1$ is the zero correlation zone Z_0.

Proof:
1) When $i = j$,

$$\tau = 0,$$
$$R_{uv}(0) = E, R_{b^i b^j}(0) = N_2,$$
$$R_{x^i y^j}(0) = R_{uv}(0) R_{b^i b^j}(0) = EN_2;$$
$$0 < |\tau| \leq N_1 - 1,$$
$$R_{uv}(\tau) = 0,$$
$$R_{x^i y^j}(\tau) = R_{uv}(\tau mod N_1) R_{b^i b^j}(\tau mod N_2) = 0;$$

2) When $i \neq j$,

$$\tau = 0,$$
$$R_{b^i b^j}(0) = 0,$$
$$R_{x^i y^j}(0) = R_{x^j y^i}(0)$$
$$= R_{uv}(\tau mod N_1) R_{b^i b^j}(\tau mod N_2) = 0;$$
$$0 < |\tau| \leq N_1 - 1,$$
$$R_{uv}(\tau) = 0,$$
$$R_{x^i y^j}(\tau) = R_{x^j y^i}(\tau)$$
$$= R_{uv}(\tau mod N_1) R_{b^i b^j}(\tau mod N_2) = 0.$$

According to Definition 2-1, the sequence-pair set constructed by the above method is ZCZ sequence-pair set.

V. PROPERTIES OF PERFECT PUNCTURED ZCZ SEQUENCE-PAIR SET

Considering the perfect punctured ZCZ sequence-pair set that is constructed by the method mentioned in the last section, the autocorrelation and cross correlation properties can be simulated and analyzed with Matlab. For example, the perfect punctured ZCZ sequence-pair set (X, Y) is constructed by 31-length perfect punctured binary sequence-pair (u, v), $u = (1111-1-1-11-11-11111-1-1-1-11-1-11-1-1111-111-1)$, $v = (1111000101011100001001001110110)$ and Hadamard matrix $H = [1111; 1-11-1; 11-1-1; 1-1-11]$ of order 4. We follow the three steps presented in Section 3 to construct the 124-length perfect punctured ZCZ sequence-pair set. The number of sequence-pair here is 4 and the length of each sequence is $31 * 4 = 124$. The first line of each matrix $X = [x_1; x_2; x_3; x_4]$ and $Y = [y_1; y_2; y_3; y_4]$ constitute a certain perfect punctured ZCZ sequence-pair (x_1, y_1). Similarly,

3

the second line of each matrix X and Y constitute another perfect punctured ZCZ sequence-pair (x_2, y_2).

$$x_1 = (\quad 1111 - 1 - 1 - 11 - 11 - 1111 - 1 - 1 - 1 - 1$$
$$1 - 1 - 11 - 1 - 1111 - 111 - 11111 - 1 - 1$$
$$-11 - 11 - 1111 - 1 - 1 - 1 - 11 - 1 - 11 - 1$$
$$-1111 - 111 - 11111 - 1 - 1 - 11 - 11 - 111$$
$$1 - 1 - 1 - 1 - 11 - 1 - 11 - 1 - 1111 - 111 - 1$$
$$1111 - 1 - 1 - 11 - 11 - 1111 - 1 - 1 - 1 - 11$$
$$-1 - 11 - 1 - 1111 - 111 - 1 \quad),$$

$$y_1 = (\quad 111100010101110000100100111011011111000$$
$$10101110000100100111011011110001010111$$
$$00001001001110110111100010101110000100$$
$$1001110110 \quad);$$

$$x_2 = (\quad 1 - 11 - 1 - 11 - 1 - 1 - 1 - 1 - 1 - 11 - 1$$
$$-11 - 1111 - 1 - 1 - 111 - 1111 - 1 - 1 - 1$$
$$1 - 111 - 1111111 - 111 - 11 - 1 - 1 - 1111$$
$$-1 - 11 - 1 - 1 - 1111 - 11 - 1 - 11 - 1 - 1$$
$$-1 - 1 - 1 - 11 - 1 - 11 - 1111 - 1 - 1 - 11$$
$$1 - 1111 - 1 - 1 - 11 - 111 - 1111111 - 111$$
$$-11 - 1 - 1 - 1111 - 1 - 11 - 1 - 1 - 111 \quad),$$

$$y_2 = (\quad 1 - 11 - 1000 - 10 - 10 - 11 - 10000100 - 1$$
$$001 - 1101 - 10 - 11 - 1100010101 - 110000$$
$$-100100 - 11 - 10 - 1101 - 11 - 1000 - 10$$
$$-10 - 11 - 10000100 - 1001 - 1101 - 10 - 1$$
$$1 - 1100010101 - 110000 - 100100 - 11 - 10$$
$$-110 \quad).$$

Perfect punctured ZCZ sequence-pairs (x_1, y_1) and (x_2, y_2) are simulated and investigated in the following parts.

A. Autocorrelation and Cross Correlation Properties

The autocorrelation property and cross correlation property of 124-length perfect punctured ZCZ sequence pair set (X, Y) are shown in Fig.1 and Fig.2 .

From the Fig.1 and Fig.2, the sidelobe of autocorrelation of ZCZ sequence-pair set can be as low as 0 when the time delay is kept within $Z_0 = N_1 = 31$ (zero correlation zone) and the cross correlation value is kept as low as 0 during the whole time domain.

B. Ambiguity function

When the transmitted impulse is reflected by a moving target, the reflected echo signal includes a linear phase shift which corresponds to a Doppler shift f_d [14]. As a result of the Doppler shift f_d, the main peak of the autocorrelation function is reduced and so as to the SNR degradation shown as following:

$$[d]_{dB} = 10log \frac{\int_0^T x(s)x^*(s)ds}{\int_0^T x(s)e^{j2\pi f_d T_c}x^*(s)ds} \tag{13}$$
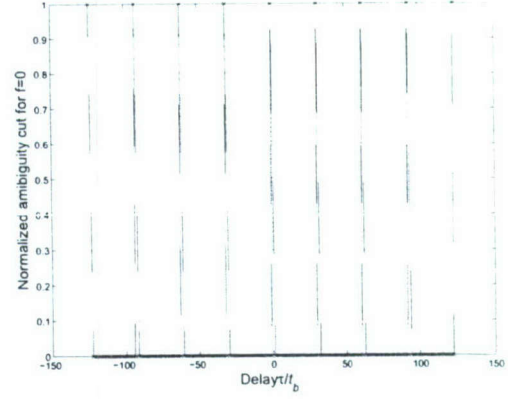

Fig. 1. Periodic autocorrelation property of perfect punctured ZCZ sequence-pair set
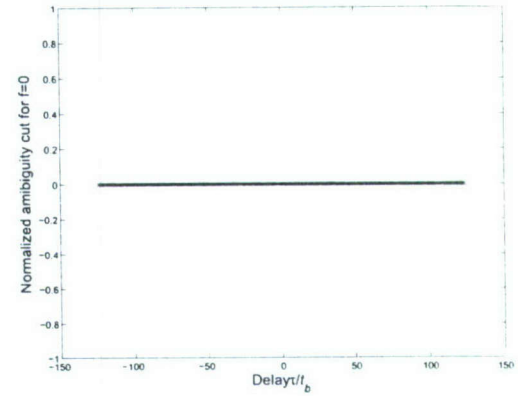

Fig. 2. Periodic cross correlation property of perfect punctured ZCZ sequence-pair set

In addition, the sidelobe structure is changed because of the Doppler shift.

The ambiguity function which is usually used to analyze the radar performance within Doppler shift can be found in [14] shown as following:

$$y(t, F_D) = \int_{-\infty}^{\infty} x(s)e^{j2\pi F_D s}x^*(s - t)ds \equiv \hat{A}(t, F_D) \tag{14}$$

where t is the time delay and F_D is the Doppler shift.

An equivalent definition can be given in terms of the signal spectrum by applying basic Fourier transform properties

$$\hat{A}(t, F_D) = \int_{-\infty}^{\infty} X^*(F)X(F - F_D)e^{j2\pi Ft}dF \tag{15}$$

The *ambiguity function* is defined as the magnitude of $\hat{A}(t, F_D)$ [14] as following:

$$A(t, F_D) \equiv |\hat{A}(t, F_D)| \tag{16}$$

However, we have ZCZ sequence-pair set in the paper, so the transmitting code and the receiving code are not the same.

4

The ambiguity function for ZCZ sequence-pair set can be rewritten as

$$y_{pair}(t, F_D) = \int_{-\infty}^{\infty} x^{(p)}(s)e^{j2\pi F_D s}y^{(q)*}(s-t)ds$$
$$where\ p, q = 0, 1, 2..., K-1$$

$$\hat{A}_{pair}(t, F_D) = \int_{-\infty}^{\infty} X^{(p)*}(F)Y^{(q)}(F-F_D)e^{j2\pi Ft}dF$$

$$where\ p, q = 0, 1, 2..., K-1 \qquad (17)$$

The *ambiguity function* is defined as the magnitude of $\hat{A}_{pair}(t, F_D)$ as following:

$$A_{pair}(t, F_D) \equiv |\hat{A}_{pair}(t, F_D)| \qquad (18)$$

In addition, assume the ZCZ sequence-pair set are (X, Y), $x^{(p)} \in X$, $x^{(p)} = \sum_{n=0}^{N-1} x_n^{(p)}(t - nT_s)$ and $y^{(p)} \in Y$, $y^{(q)} = \sum_{n=0}^{N-1} y_n^{(p)}(t - nT_s)$, since the periodic correlation is used instead of aperiodic correlation in this paper. The $\hat{A}_{pair}(t, F_D)$ in one period of length NT_s can be expressed as:

$$|\hat{A}_{pair}(t, F_D)| \qquad (19)$$
$$= | \int_0^t u^{(p)}(s - nT_s)v^{(q)*}(s - nT_s - (NT_s - t))$$
$$e^{(j2\pi F_D s)}ds + \int_t^{(N-1)T_s} u^{(p)}(s - nT_s)v^{(q)*}$$
$$(s - nT_s - t)e^{(j2\pi F_D s)}ds|, \ p, q = 0, 1, 2..., K-1$$

At the same time, when $p = q$, equation (20) can be used to analyze the autocorrelation performance within Doppler shift; and when $q \neq p$, equation (20) can be used to analyze the cross correlation performance within Doppler shift. Equation (20) is plotted in Fig.3 in a three-dimensional surface plot to analyze the radar performance of perfect punctured ZCZ sequence-pair set within Doppler shift. Here, maximal time delay is 1 unit (normalized to length of the code, in units of NT_s) and maximal doppler shift is 5 units for cross correlation and 3 units for autocorrelation (normalized to the inverse of the length of the code, in units of $1/NT_s$).

In Fig.3(a), there is relative uniform plateau suggesting low and uninform sidelobes, minimizing target masking effect in zero correlation zone of time domain, where $Z_0 = 31$, $-31 < \tau < 31$. From Fig.3(b), considering cross correlation property between any two perfect punctured ZCZ sequence-pairs among the ZCZ sequence-pair set, 124-length perfect punctured ZCZ sequence-pair set is tolerant of Doppler shift when Doppler shift is not large. When the Doppler shift is zero, the range sidelobe of cross correlation of our proposed code is zero in the whole time domain.

As synchronization technology develops quickly in the industrial world, time delay can, to some extent, be well limited, it is necessary to investigate the performance of our proposed code without time delay. When $t = 0$, the ambiguity function can be expressed as:

$$\hat{A}_{pair}(0, F_D) = \int_0^{T_s} x(s - nT_s)y^*(s - nT_s)e^{(j2\pi F_D s)}ds \quad (20)$$
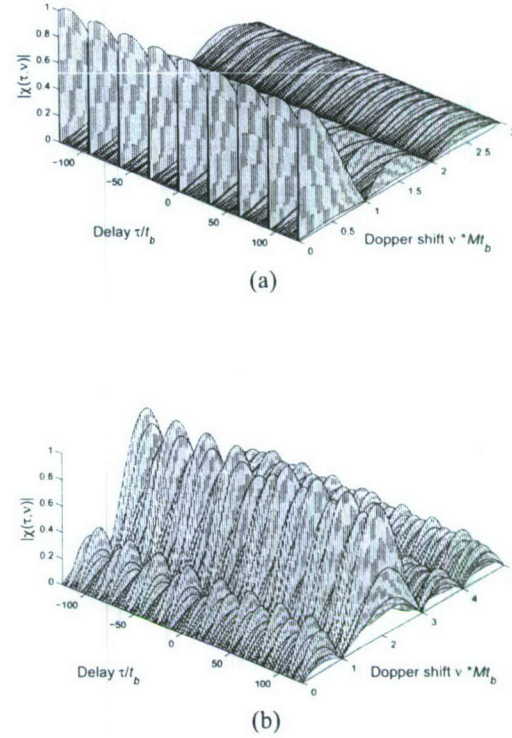

(a)

(b)

Fig. 3. Ambiguity function of 124-length ZCZ sequence-pair set: (a) autocorrelation (b) cross correlation

And the doppler shift performance without time delay is presented in the Fig.4.

Fig.4(a) illustrates that without time delay, when the Doppler shift is less than 1 unit, autocorrelation value of perfect punctured ZCZ sequence-pair set falls sharply and the trend of the amplitude over the whole frequency domain decreases as well. Fig.4(b) shows that there are some convex surfaces in cross correlation performance. Observe Fig.4(a) and Fig.4(b), when Doppler frequencies equal to multiples of the pulse repetition frequency ($PRF = 1/PRI = 1/Ts$) except Doppler frequency is equal to 2 PRF for cross correlation, all the ambiguity value turns to be zero. That is the same as many widely used pulse compression binary code such as Barker code. In a word, behavior in time delay and in response to Doppler shift shown by ambiguity function of perfect punctured ZCZ sequence-pair set can be as good as conventional pulse compression binary code.

VI. SYSTEM SIMULATION IN RADAR SYSTEM

According to [14], P_D(Probability of Detection), P_{FA}(Probability of False Alarm) and P_M(Probability of Miss) are three probabilities of most interest in the radar system. Note that $P_M = 1 - P_D$, thus, P_D and P_{FA} suffice
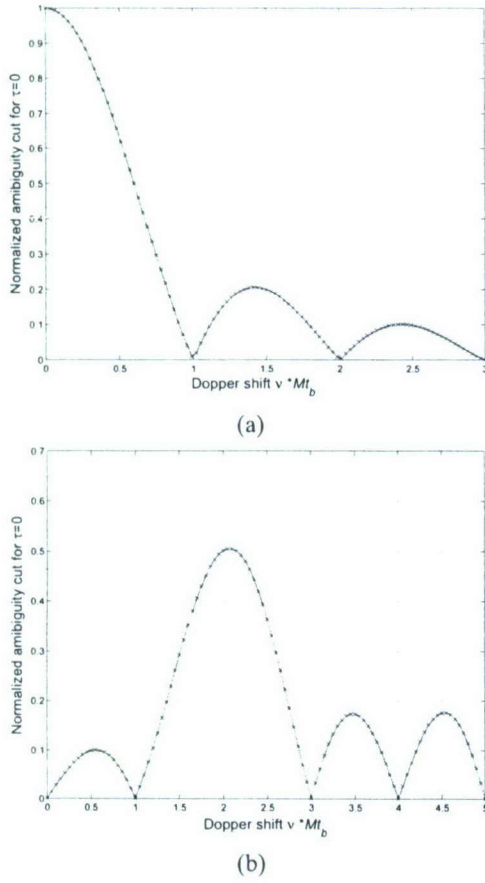
5

(a)

(b)

Fig. 4. Doppler shift of 124-length ZCZ sequence-pair set(time delay=0): (a) autocorrelation (b) cross correlation
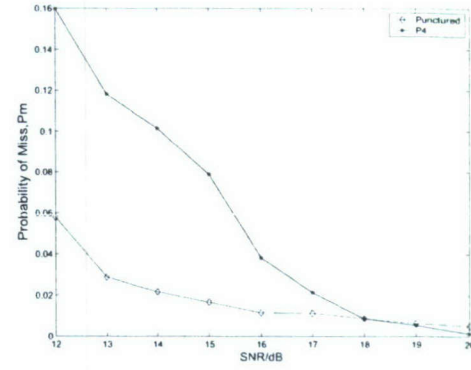

Fig. 5. Probability of miss targets detection (No time delay, Doppler shift less than 1): 124-length perfect punctured ZCZ sequence-pair VS. 124-length P4 code
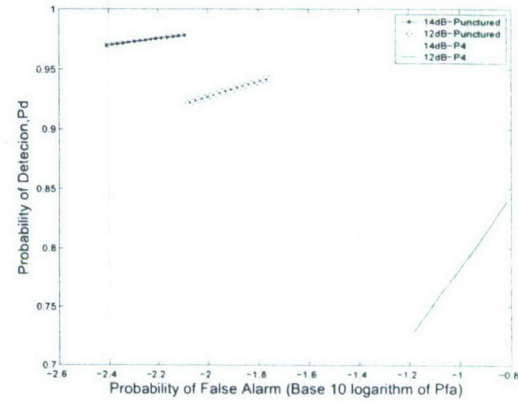

Fig. 6. Probability of detection versus probability of false alarm of the coherent receiver(No time delay, Doppler shift less than 1) : 124-length perfect punctured ZCZ sequence-pair VS. 124-length P4 code

to specify all of the probabilities of interest in radar system. Therefore, we simulated the above three probabilities of perfect punctured ZCZ sequence-pair in radar system in this section. The performance of 124-length P4 code is also provided in order to compare with the performance of punctured binary perfect punctured ZCZ sequence-pair of corresponding length. In the simulation model, 10^5 times of Monte-Carlo simulation has been run for each SNR value. The Doppler shift frequency that is kept less than 1 unit (normalized to the inverse of the length of the code, in units of $1/NT_s$) is a random variable, and the time delay is assumed zero. Threshold detection is used in this coherent system where the threshold is adaptively adjusted.

In Fig.5, the probabilities of miss target detection P_M of the system using 124-length perfect punctured ZCZ sequence-pair are lower than 124-length P4 code especially when the SNR is not large. When SNR is larger than 18 dB, both probabilities of miss targets of the system approaches zero. However, the probabilities of miss targets of P4 code fall more quickly than perfect punctured ZCZ sequence-pair.

We plotted the probability of detection P_D versus probability of false alarm P_{FA} of the coherent receiver in Fig.6.

Fig.6 shows performance of 124-length perfect punctured ZCZ sequence-pair and the same length P4 code when the SNR is 10dB and 14dB. Within the same SNR value either 10dB or 14dB, the probabilities of detection of 124-length perfect punctured ZCZ sequence-pair are much larger than probabilities of detection of 124-length P4 code, and meanwhile probabilities of false alarm of the first code are also smaller than P_{FA} of the latter code. In some other words, 124-length perfect punctured ZCZ sequence-pair has higher target detection probability while keeping a lower false alarm probability. Furthermore, observe Fig.6, 124-length perfect punctured ZCZ sequence-pair even has much better performance with 10dB SNR than 124-length P4 code with 14dB SNR.

VII. CONCLUSION

The definition and properties of ZCZ sequence-pair set are discussed in this paper. Based on perfect punctured sequence-pair and Hadamard matrix, a constructing method for the perfect punctured ZCZ sequence-pair set has been investigated along with its properties. The significant advantage of the

6

perfect punctured ZCZ sequence-pair set is a considerably reduced sidelobe as low as zero in the zero correlation zone and zero mutual cross correlation value in the whole time domain. The disadvantage of our proposed code is that the number of the sequences in the set depends on the order of Hadamard matrix that is limited by $2^k, (k = 0, 1, ...)$. According to the radar system simulation results shown in Fig.5 and Fig.6, it is easy to observe that 124-length perfect punctured ZCZ sequence-pair set has better performance than 124-length P4 code when the Doppler shift is kept less than 1 unit(normalized to the inverse of the length of the code, in units of $1/NT_s$). As a result, the general conclusion can be drawn from the results presented in this paper that the perfect punctured ZCZ sequence-pair set, which has much better autocorrelation and cross correlation properties than the optimum biphase codes(longer than 13), whose autocorrelation sidelobes and cross correlation peak value have been found to be both approximately $\sqrt{N}$, can effectively increase the variety of candidates for pulse compression codes. Because of the ideal cross correlation properties of perfect punctured ZCZ sequence-pair set, future work would be focused on the application of the perfect punctured ZCZ sequence-pair set in multiple radar system.

ACKNOWLEDGEMENT

REFERENCES

[1] S. Ariyavisitakul, N. Sollenberger, and L. Greenstein, *Introduction to Radar System*, Tata McGraw-Hill, 2001.
[2] A. M. Boehmer, "Binary pulse compression codes," *IEEE Trans.Informaion Theory*, vol.IT-13, pp.156-167, April 1967.
[3] R. Turyn, "On Barker codes of event length," *Proc.IEEE*, vol.51,9.1256, September 1963.
[4] U. Somaini, "Bianry sequences with good autocorrelation and cross correlation properties," *IEEE Transactions on Aerospace and Electronic Systems*, AES-11, 6, 1226-1231, Nov.1975.
[5] R. L. Frank, "Polyphase codes with good nonperiodic correlation properties", *IEEE Transactions on Information Theory*, IT. -9, pp. 43-45, Jan. 1963.
[6] B. L. Lewis and F. F. Kretschuner, "A new class of polyphase pulse compression codes and techniques", *IEEE Transactions on Aerospace and Electronic Systems*, AES-17, pp. 364-372, May. 1981.
[7] B. L. Lewis and F. F. Kretschuner, "Linear frequency modulation derived polyphase pulse compression codes", *IEEE Transactions on Aerospace and Electronic Systems*, AES-18, pp. 637-641, Sep. 1982.
[8] P. Z. Fan, N. Suehiro, N. Kuroyanagi and X. M. Deng, "A class of binary sequences with zero correlation zone," *IEE Electron.Letter*, 35 (10): 777-779, 1999.
[9] P. Z. Fan and L. Hao, "Generalized Orthogonal Sequences and Their Applications in Synchronous CDMA Systems," *IEICE Trans.Fundamentals*, E832A(11): 1 16, 2000.
[10] P. Z. Fan, "New Direction in Spreading Sequence Design and the Related Theoretical Bounds," *International Conference of Communications , Circuits and Systems*, June 29-July 1, 2002, PRC.
[11] S. Matsufuji, N Suehiro , N Kuroyanagi and P Z Fan, "Two types of polyphase sequence set for approximately synchronized CDMA systems," *IEICE Trans. Fundamentals*, E862A(1): 229-234, Jan. 2003.
[12] H. Torii, M. Nakamura and N. Suehiro, "A new class of zero correlation zone sequences," *Tran. Inform.Theory*, 50: 559-565, Mar. 2004.
[13] T. Jiang, *Research on Quasi-Perfect Binary Signal Pair and Perfect Punctured Binary Signal Pair Theory*, Ph.D Dissertation: Yanshan University, 2003.
[14] M.A.Richards, *Fundamentals of Radar Signal Processing*, McGraw-Hill, 2005.

7